## Title

Probing the Ultimate Limits of Biology: Developing Microparticle Platforms for High-Throughput Single-Cell Assays



## Author

de Rutte, Joseph Michael

## Publication Date

2020

Peer reviewed|Thesis/dissertation

UNIVERSITY OF CALIFORNIA

Los Angeles

# Probing the Ultimate Limits of Biology: Developing Microparticle Platforms for High-Throughput Single-Cell Assays

A dissertation submitted in partial satisfaction of the

requirements for the degree Doctor of Philosophy

in Bioengineering

by

Joseph Michael de Rutte

2020

ABSTRACT OF THE DISSERTATION

Probing the Ultimate Limits of Biology:

Developing Microparticle Platforms for High-Throughput

Single-Cell Assays

By

Joseph Michael de Rutte

Doctor of Philosophy in Bioengineering

University of California, Los Angeles, 2020

Professor Dino Di Carlo, Chair

Techniques to analyze and sort single cells based on complex phenotypes such as secreted products have the potential to transform our understanding of cellular biology as well as accelerate the development of next generation cell and antibody therapies. Microfluidic techniques have emerged over the last two decades that enable such assays by creating small compartments that can isolate individual cells. Despite these technical advances, adoption of this technology has been slow due to the complexity of the approaches and the requirement of specialty instruments. To address this issue, we developed a microparticle based approach to create uniform sub-nanoliter water in oil compartments using only standard lab equipment. We refer to these droplets formed with microparticles, dropicles.

In this dissertation I will provide an overview of various strategies used to create microscale compartments, specifically to perform single-cell secretion assays. I will then discuss in detail an approach to fabricate and use 3D structured microparticles to perform single-cell secretion assays massively in parallel with standard lab equipment. By making this microparticle approach compatible with existing high-throughput flow cytometers we are able to analyze and sort of over 100,000 single cells based on their secreted products. Lastly to create a truly democratized platform there is a need to be able to manufacture these particles in a scalable manner. In these last chapters I will discuss approaches to fabricate microparticles with different morphologies in high-throughput.

The dissertation of Joseph Michael de Rutte is approved.

Andrea L. Bertozzi

Aydogan Ozcan

Pei-Yu Chiou

Dino Di Carlo, Committee Chair

University of California Los Angeles

2020

# DEDICATION

This work is dedicated to all of my family, friends and mentors who have supported me throughout my academic journey.

I first want to thank my parents for their endless love and support. I would not have made it to where I am today without them.

I would like to thank all of the amazing members of the Di Carlo Lab. I have learned so many things from you all and am grateful for all the fond memories we have shared over the last four years.

I would like to thank my Masters' advisor Sumita Pennathur who encouraged me to pursue a graduate education, and pushed me to reach my full potential.

Lastly, I would like to thank my amazing mentor, Dino Di Carlo, who has been a source of endless support and inspiration during my PhD. I am truly grateful for having the opportunity to work together these last four years.

TABLE OF CONTENTS

TABLE OF FIGURES

# ACKNOWLEDGMENTS

I acknowledge support from the National Institutes of Health Grant #R21GM126414 and the Simons Foundation Math+X Investigator Award #510776 for the work shown in chapter 2. The work in chapter 3 was supported by the Presidential Early Career Award for Scientists and Engineers (N00014-16-1-2997) and the Eli and Edythe Broad Center of Regenerative Medicine and Stem Cell Research at UCLA and California NanoSystems Institute at UCLA Planning Award.

**Chapter 2** is adapted from: de Rutte, J., Dimatteo, R., Zee, M. van, Damoiseaux, R., and Di Carlo, D. Massively parallel encapsulation of single cells with structured microparticles and secretion-based flow sorting. BioRxiv, 2020. Doi.org/10.1101/2020.03.09.984245

J.D. and D.D. conceived and designed initial dropicle system and protocols. J.D. designed the fabrication workflow for the drop-carrier particles, performed experiments, and analyzed data. J.D. and R.Di. fabricated drop-carrier particles. J.D, R.Di. and M.V. developed cell secretion protocols. J.D., R.Di., M.V., R.Da. and D.D. designed the flow sorting studies. J.D., R.Di and R.Da performed cell sorting experiments. R.Di performed secretion cross-talk experiments. M.V. performed suspension adapted CHO cell experiments. J.D. and D.D. wrote the manuscript with input from all authors. J.D. prepared figures. D.D, supervised the study. The authors acknowledge the help of Aiden Di Carlo in editing the secretion assay workflow video.

**Chapter 3** is adapted from: de Rutte, J. M., Koh, J., & Di Carlo, D. (2019). Scalable high-throughput production of modular microgels for in situ assembly of microporous tissue scaffolds. Advanced Functional Materials, 29(25), 1900071. Doi.org/10.1002/adfm.201900071.
JMD performed all experiments. JMD and DD prepared the manuscript. JMD and JK designed experimental protocols.

**Chapter 4.** I would like to acknowledge Sohyung Lee for her assistance in developing the temperature induced phase separation workflows.

# VITA

## EDUCATION

University of California, Santa Barbara

- M.S. Mechanical Engineering 2014 – 2016
- B.S. Mechanical Engineering 2010 – 2014

## RESEARCH APPOINTMENTS

Graduate Student Researcher, University of California, Los Angeles 2016 – 2020

Professor Dino Di Carlo, Department of Bioengineering

Graduate Student Researcher, University of California, Santa Barbara 2014 – 2016

Professor Sumita Pennathur, Department of Mechanical Engineering

## SELECTED PUBLICATIONS

- Ha, K., **de Rutte, J.**, Di Carlo, D., Bertozzi, A. Minimal surface configurations for axisymmetric microparticles. *In Preparation*.
- Wu, C.Y., Wang, B., **de Rutte, J**., Joo, A., Jacobs, M., Ha, K., Bertozzi, A.L., Di Carlo, D. Monodisperse drops templated by 3D-structured microparticles. *Science Advances* (Accepted)
- **de Rutte, J.**, Dimatteo, R., Zee, M. van, Damoiseaux, R., and Di Carlo, D. Massively parallel encapsulation of single cells with structured microparticles and secretion-based flow sorting. *BioRxiv,* 2020.

- **de Rutte, J.M.**, Koh, J., Di Carlo, D. Scalable high-throughput production of modular microgels for *in-situ* assembly of microporous tissue scaffolds. *Advanced Functional Materials*, 2019. (Inside Cover)
- Sheikhi, A., **de Rutte, J.**, Haghniaz, R., Akouissi, O., Sohrabi, A., Di Carlo, D., & Khademhosseini, A. Microfluidic-enabled bottom-up hydrogels from annealable naturally-derived protein microbeads. *Biomaterials*, 2019.
- **de Rutte, J. M.**, Janssen, K. G., Tas, N. R., Eijkel, J. C., & Pennathur, S. Numerical investigation of micro-and nanochannel deformation due to discontinuous electroosmotic flow. *Microfluidics and Nanofluidics*, 2016.

## SELECTED AWARDS

- UCLA Bioengineering Outstanding PhD Award, 2020
- First Place Podium Presentation, Bioengineering Research Day, UCLA, 2020
- SLAS Innovation Award, SLAS International Conference & Exhibition, 2020
- Tony B. Academic Travel Award, SLAS International Conference & Exhibition, 2020
- NIST and Lab on a Chip – Art in Science Award, MicroTAS, 2019
- Student Travel Grant, MicroTAS, 2018
- The Center for Minimally Invasive Therapeutics Award on scientific excellence, 2018
- First Place Speaking Award, SoCal Micro & Nanofluidics Symposium, 2018
- UCLA Graduate Division Fellowship, 2016-2017
- Outstanding Senior Award, Department of Mechanical Engineering, UCSB, 2014

# Chapter 1. Introduction to single cell secretion assays

## 1.1. Introduction

The ability for cells to secrete bioactive molecules is critical in the regulation of cell and tissue functions. The complex set of molecules secreted by cells into the extracellular space, or secretome, encompasses many different molecules, including antibodies, cytokines, growth factors, extracellular matrix proteins, exosomes, and matrix metallic proteases (**Figure 1-1**).[1] The vastness of the secretome underscores its importance in a wide array of biological processes. Of the ~20,000 protein coding genes, ~3,000 proteins are predicted to be secreted compared to ~5,000 membrane proteins[2]. These secreted factors lead to outsized biological effects compared to membrane bound molecules because of their ability to diffuse and rapidly remodel signaling in many nearby cells and tissues. For example, local increases in growth factor concentrations can aid the regeneration and maturation of vasculature, enabling tissue regrowth after traumatic injury.[3] Cytokines and chemokines work in concert to coordinate the activity of immune cells as they respond to pathogens.[4,5] Proteolytic enzymes catalyze reactions in the cellular microenvironment, proving critical in functions such as extracellular matrix remodeling.[6] Antibodies produced by immune cells neutralize pathogens such as bacteria and viruses and are a critical part of the adaptive immune response.[7] Further, recombinant antibodies manufactured from producer cell lines can be used directly as therapies.[8] Exosomes are involved in immune response and signal transduction, capable of transporting membrane bound proteins, RNA, and DNAs between cells.[9,10]

Despite the importance of cell secretions in understanding biological function and in the development of cell and antibody therapies, there is limited access to tools that can probe functional cells based on secretions with high-sensitivity. Increasingly, researchers have pointed to cellular heterogeneity as a significant factor in the variability of therapeutic efficacy for cell therapies[11–14]. Even in genetically homogeneous cell populations, there can be a large variation in functional phenotype such as cell secretion, indicating that bulk measurements, which treat all cells as the mean, are not sufficient for accurately determining cell properties[15]. As such being

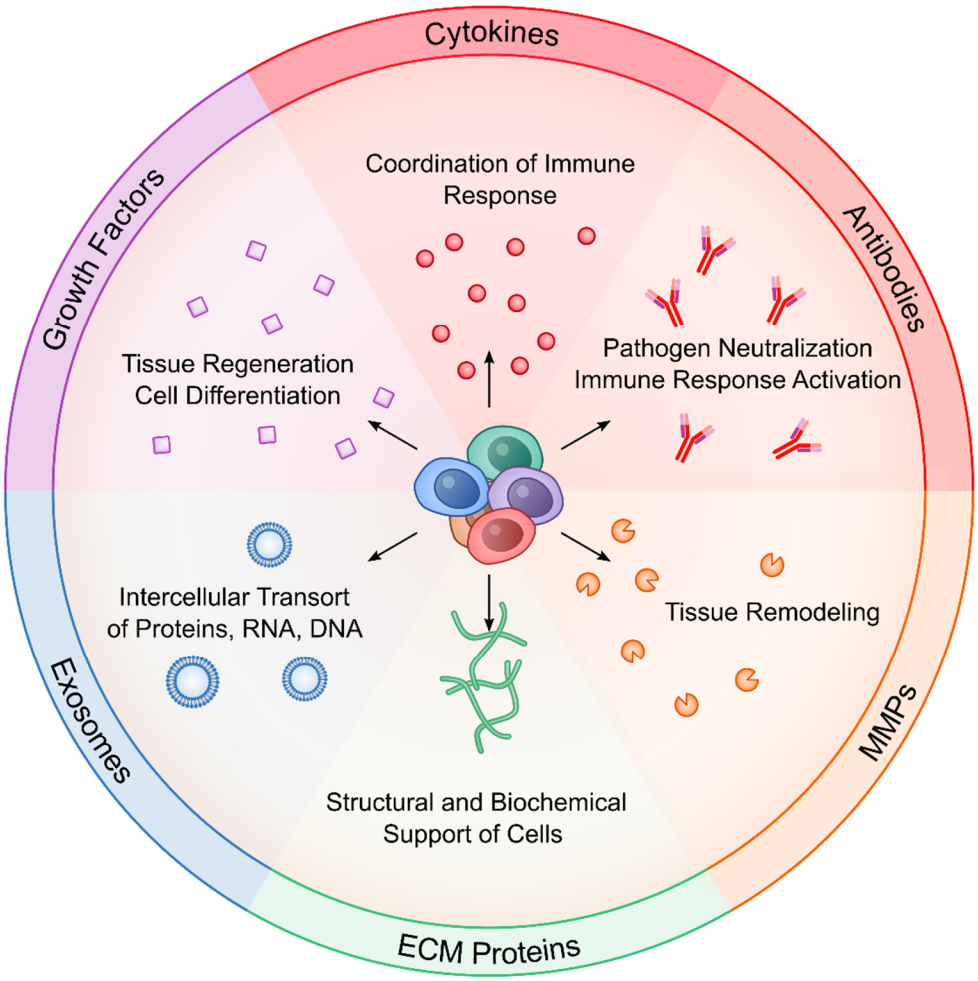


**Figure 1-1 Overview of the cell secretome.** The cell secretome encompasses a wide range of molecules secreted by cells including cytokines, antibodies, matrix metalloproteinases (MMPs), extracellular matrix (ECM) proteins, growth factors, and exosomes. These secreted molecules have a significant role in regulating communication between different cells, directing general cell behavior such as migration, growth, differentiation, and cell death.

able to profile these functional properties at the single cell level is critical in elucidating how the heterogeneity affects the outcome of disease and therapies. Lastly, technologies that can screen and sort these cells can potentially be employed to isolate out subpopulations of highly-functional cells for downstream therapeutic use such as cell and antibody therapies[16]. In this introduction, I will highlight the state of the art in single cell secretion-based profiling technology. Specifically, I will describe the foundational engineering principles guiding the design of functional profiling technologies, and discuss some of the limitations of these current platforms.

### 1.2. **Overview of single cell secretion profiling concepts and design**

Single cell secretion assays rely on three critical functions: (1) partitioning of single cells into individual compartments, (2) detection of secreted molecules via biochemical reaction (3) measurement of the detection signal and isolation of cells of cells based on this signal. In this section we will provide an overview of the various approaches to achieve these functions.

To prevent cross-talk of secreted molecules between individual cells, cells are partitioned in to separate compartments, preferably at a similar length scale to the cells themselves (**Figure 1-2**). Compartmentalization of cells typically relies on either physical confinement using microfabricated channels or through formation of droplets in an immiscible oil solution (i.e. water in oil droplets). Microfabricated geometries may utilize pumps and valves in order to load or unload cells.[17,18] Other approaches utilize microwell arrays which can be loaded with cells by seeding with a micropipette.[19–24] Recent commercial platforms have utilized optofluidic manipulation to load and unload cells into chambers or "nanopens".[25–27] This general physical confinement strategy we will generally define as microchamber based approaches.

Compartmentalization via droplets is typically achieved by loading cells into a microfluidic droplet generator to sequentially pump cells into uniform water in oil droplets.[28–30] More recently, structure microparticles have been used to create uniform droplets templated by the particles using simple agitation (dropicles).[31] Microchamber approaches are advantageous in that both adherent and non-adherent cell types can be analyzed, and the spatial location of the compartments are fixed allowing temporal observation and measurement. Due to the lack of a solid surface, droplet microfluidic approaches are more suited to analysis of non-adherent cell types. An exception to this is the dropicle platform in which the hydrogel particles used to create the droplets can functionalized to maintain adherent cell types.

After confinement, the secreted products accumulate and are measured using various detection approaches (**Figure 1-2**). The most common approach utilizes a sandwich assay to detect the secreted products. Secreted proteins are captured onto a solid surface functionalized with capture antibodies or target antigen and then labeled with a secondary antibody typically conjugated with a visual readout such as a fluorophore. Microchamber approaches can directly conjugate the capture proteins to the channel surface, or conjugate to beads that can be loaded into the channels with the cells to concentrate the signal. To perform a sandwich assay using droplet- based approaches, capture beads are typically co-encapsulated into the drops with cells. In this strategy it is ideal to have only a single capture bead in order to concentrate accumulated signal at to a single point achieve high enough signal over background. A significant limitation of the bead-based approach is that both the loading of the cells and beads into the drops follow Poisson statistics leading to a low fraction of droplets containing both a single cell and single capture bead. Other droplet approaches get around this limitation by adding higher concentrations of microbeads to ensure each cell containing droplet has at least one capture bead.

One issue to this approach is difficulty in detecting signal from background as the signal is no longer concentrated into a single location. Other droplet approaches have mitigated this limitation by developing workflows that are compatible with using many capture microbeads per droplet.[32–34] In one strategy researchers utilize a reversible gel matrix in the media to be able to transfer the cell and capture beads into an aqueous phase after the incubation step, and then label and wash away background signal.[32] Others have used magnetic nanoparticles to locally concentrate the secretion signal using a fixed magnet after incubation to improve signal over background.[33,34] In contrast, the dropicle approach removes the double Poisson loading issue due to each dropicle contains a templating particle that can be used as a solid surface for the sandwich assay.[31] Further this approach also allows for transferring of the cell and associated particle out of the oil phase for labeling and washing which significantly reduces background signal. An alternative approach utilizes the cells as a capture bead by binding capture antibodies directly to the cell surface to capture secreted proteins, removing the double Poisson loading issues. This has been done by directly biotinylating surface proteins or by using bi-functional antibody conjugates.[35–37] Lastly it is important to note that from some secretion assays FRET based methods can be employed to remove the need for a capture surface. However, this approach is not as generalizable, being restricted to custom FRET antibodies or detection of enzymes and in the latter case has its own difficulties due to the higher potential for background signal.[38,39]

Once secreted molecules of interest are captured and labeled, they are measured typically via a fluorescent readout. For nearly all the microchannel confinement approaches readout is performed via fluorescent microscopy or some related fluorescence imaging technique. With this approach spatial patterning can be utilized in order to improve the number of secretions that can

be profiled simultaneously. Barcoding approaches have been used to screen up to 40 secreted proteins simultaneously[40], nearly 10-fold above approaches that only utilize different fluorescent channels to multiplex.[14,19] There are some disadvantages to this approach, namely the throughput is limited to scanning over each of the confined chambers, and typically the approaches are not well suited for sorting which will be discussed below. For standard droplet microfluidic approaches secretion readout is typically performed either using a fluorescent microscope or using a customize microfluidic detection chip.[29,41] By using a flow detection system significantly more cells can be screened in a single assay, up to 1 million cells. Some droplet approaches (e.g. gel microdrops, cell surface binding, and dropicle approaches) allow for transferring of the cells and associated secretion signal back into a water phase allowing readout using standard flow cytometers.[31,32,42,43] This has the advantage of employing well established highly sensitive readout infrastructure while maintaining higher and even higher throughputs.

Lastly for many applications it is desirable to isolate cells based on a particular secretion phenotype. It is important to note that many of the microchamber based approaches are more suited for high information screening and not high-throughput sorting. For many platforms, isolation is not possible or relies on highly slow picking/pipetting.[19,44] In some cases, such as the Berkeley lights platform isolation can be achieved via optofluidic manipulation of the cells, although with limited throughput. In general, droplet-based approaches are better suited for high-throughput sorting applications as custom droplet sorters which employ dielectrophoretic forces can be used to sort desired cells contained in a droplet.[41,45,46] Approaches that are compatible with flow-cytometers are even more amenable to sorting as FACS instruments are well established and are capable of sorting at event rates up to ~$10^4$ $s^{-1}$ for these systems.

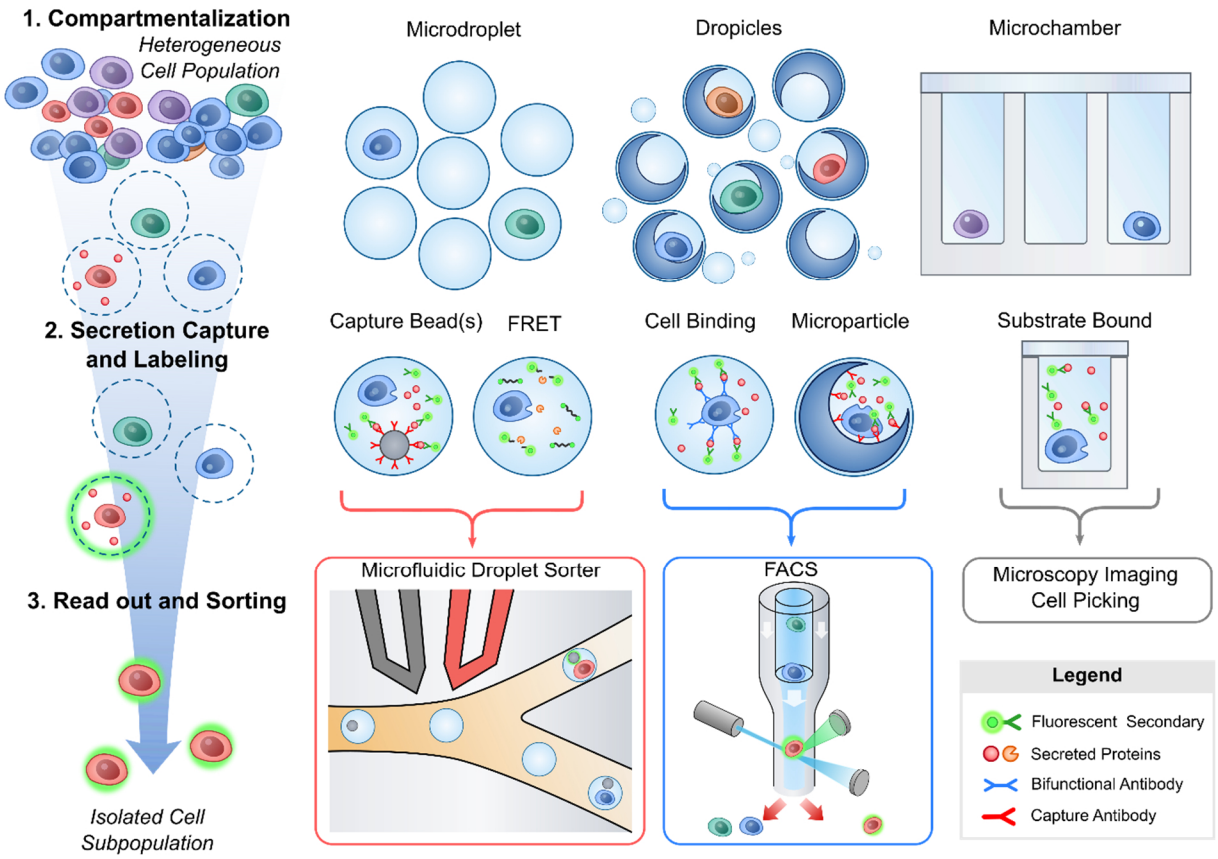


**Figure 1-2 Criteria for single cell secretion analysis and sorting.** (1) Cells are first compartmentalized to prevent crosstalk of signal between individual cells. This can be achieved using a variety of techniques including seeding into microchambers or partitioning into water-in-oil microdroplets using microfluidics or using emerging particle-based approaches. (2) Once compartmentalized cells are incubated and secreted products is detected using a variety of biochemical techniques. A common approach is using a sandwich assay where the secreted molecule is attached to a solid substrate (chamber surface, bead, particle, cell surface) and then labeled with a fluorescent secondary antibody. For some applications FRET-based approaches can be used (e.g. protease secretions, custom detection antibodies). (3) After accumulation of secretion signal the cells and associated signal must be readout and if desired subtypes of interest are isolated. Microscopy approaches are compatible with most techniques but do not facilitate high-throughput sorting. For some droplet approaches sorting has been achieved using microfluidic droplet sorters or by sorting cells directly via FACS.

## 1.3. **Discussion**

In this chapter I presented an overview of single cell secretions and the various platforms available for performing single cell level analysis and sorting. These approaches have their own unique strengths and weaknesses, making some more suitable for specific applications (**Table 1-1**). Microchamber based approaches are limited by their modest cell throughput and difficulty

in downstream cell isolation. However, these approaches are information rich, capable of performing highly multiplexed assays on over 40 proteins simultaneously making them particularly useful for studying cells with more complex secretion profiles (e.g. cytokines produced by T-cells). [20,40,44,48,49] Optofluidic based microchamber approaches have added capabilities for automation and isolation, but the instrumentation required is highly complex and prohibitively expensive, restricting its adoption by resource limited labs.[5,26] Droplet based approaches are typically less information rich then microchamber based approaches, but have the added benefit of increased throughput, capable of screening up to a million cells in a single workflow. Standard droplet based systems require both a device for encapsulation of cells into droplets as well as a specialized device for downstream analysis.[33,34,39,47] Modified workflows have been developed to make some of these droplet assays compatible with FACS in order to improve the accessibility of the systems.[32,42,43] However, these approaches still rely on use of upstream droplet generators to create uniform compartments for cells. Further, these droplet-based approaches are typically only compatible with suspension cells limiting its range of applications. Although, these platforms have achieved a level of technical achievement in performing single cell secretion assays, there is still significant limitations in their accessibility.

The dropicle platform has recently emerged as a droplet-based approach that addresses many of the limitations of the previous single cell secretion analysis platforms.[31] Specifically, by utilizing structured particles to create uniform compartments using simple pipetting steps, the end user is no longer required to acquire specialized microfluidic devices and equipment. Further, downstream analysis and sorting is compatible with standard, widely accessible FACS instruments enabling high-throughput sorting and potential for a high degree of multiplexing. The inclusion of a solid surface with each compartment also makes the system more compatible

adherent cell types which could unlock new applications, for example isolation of mesenchymal stem cells based on functionality for downstream therapies. Due to its superior capabilities, and its compatibility with common lab infrastructure, we see that the dropicle platform has the potential to make single cell secretion assays accessible to significantly more researchers in the near future.

**Table 1-1. Comparison of techniques for single cell analysis/sorting based on secretions.** Accessibility metrics are defined as follows: ‖ Compartmentalization with standard lab infrastructure; † Analysis compatible with standard lab infrastructure; ‡ Sorting compatible with standard lab infrastructure; § No additional capital equipment required. *Higher end not demonstrated but predicted based on current FACS instrument limitations.

| Technique | Throughput (number of cells) | Sorting Capability | Cell Type Compatibility (A – Adherent, S – Suspension) | Surface Marker Staining After Secretion Assay | Multi-plexing | Cells/$1000 | Accessibility (†,‡,§,‖) | References |
|---|---|---|---|---|---|---|---|---|
| Microchamber/ Microarray | $10^4$ – $10^5$ per chip | Possible but difficult | S / A | Yes | 4 – 40 | $10^2$ – $10^3$ | † | [20,40,44,48,49] |
| Optofluidics | $10^3$ – $10^4$ per chip | Yes | S / A | Yes | 4 | $10^2$ – $10^3$ | | [25,26] |
| Droplets - FADS | $10^4$ – $10^6$ | Yes | S | No | 2+ | $10^6$ | † | [34,50,51] |
| Droplets - FACS | $10^5$ – $10^6$ | Yes | S | Yes | 4 – 20* | $10^6$ | †,‡ | [32,42,43] |
| Dropicles | $10^5$ – $10^6$ | Yes | S/A | Yes | 4 – 20* | $10^7$ | ‖,†,‡,§ | [31] |

# Chapter 2. Encapsulation of single cells with structured microparticles and secretion-based flow sorting

In the last chapter I presented a detailed overview of the current state of microtechnology for performing single cell secretion assays as well as discuss the potential implications in microbiology and emerging cell and antibody therapies. In this next chapter I will present our work on using microparticles to address some of the significant limitations of existing cell secretion technology. Specifically, how it can enable these assays to be performed on standard lab equipment without the direct use of microfluidics. I then validate the approach and demonstrate its utility for selecting out sub-populations of a therapeutic antibody producing cell line.

## 2.1. **Introduction**

The ability to analyze and sort cells based on secretions (antibodies, cytokines, proteases, other enzymes, or even exosomes/microvesicles) is fundamental to our understanding of functional cellular heterogeneity underlying biology and to our ability to create new biotechnology products, such as biologics and cell therapies. However, consistent, easily accessible and automatable solutions for this basic biological problem do not exist. Moreover, within the populations of secreting cells are subsets of rare cells with secretion profiles of outsized importance, with a quintessential example being B cells. The ability to sort rare B cells or B cell fusions, such as hybridomas, directly based on their production levels and activity of high affinity antibodies would allow for the acquisition of gene sequences that can be used to make new antibody drugs.[52–57] Further, sorting of stable, production-grade cells, such as Chinese hamster ovary (CHO) cells, based on their production rate of humanized IgG protein would

allow for the selection of specific clones useful for monoclonal antibody (mAb) drug production environments.[58] Both of these use cases are of urgent interest during pandemics, such as the current COVID-19 pandemic, to rapidly discover and produce neutralizing mAbs or characterize vaccine effectiveness.[59] Finally, the ability to sort rare populations of cells for outlier clones with ultra-high-performing secretion profiles promises to enable cycles of selection and mutagenesis important for directed cellular evolution of the next generation of cell therapies and also can enable performance surveillance of the clones themselves over time.[16]

Although secretion of proteins or other biological products is a key function of many cells, approaches to sort cells at high rates based on this function have significant tradeoffs and are not widespread. Intracellular staining of secreted proteins prior to secretion by cells can be performed following fixation and permeabilization. Fluorescence activated cell sorting (FACS) can then be used to isolate sub-populations based on levels of these retained intracellular proteins.[60,61] However, cells are non-viable after this process and intracellular stores of proteins may not directly reflect the secreted amount or functional state of secreted proteins. An alternative approach involves binding capture antibodies directly to the cell surface to capture secreted proteins. This has been done by directly biotinylating surface proteins or by using bi-functional antibody conjugates.[35–37] Captured secretions can then be labeled with fluorescently-conjugated antibodies, and cells can be sorted using standard FACS. Unfortunately, these strategies can affect cell viability or require the presence of specific surface proteins on the cell surface (e.g. CD45). Further, this general approach suffers from significant cross-talk for high secretors due to transport of secreted products away from the secreting cells. More recent approaches place single cells into nanoliter scale compartments to prevent cross-talk of secretions.[42,43]

Screening of live cells based on single cell secretions relies on the ability to isolate single cells into uniform compartments to reduce crosstalk, capture secretions onto a solid substrate, and readout/select cells based on an associated signal.[62] Droplet microfluidics can be used to compartmentalize cells with capture beads or within capture gel matrices and sort droplets containing cells of interest with custom droplet sorters or flow cytometers.[29,41,45,63] Cells can also be seeded into microwells with surfaces modified to capture secretions and following secretion, target cells can be sorted one-by-one with a pipette.[48,64] Optofluidic approaches, e.g. from Berkeley Lights, transport and compartmentalize cells using optically induced dielectrophoretic manipulation, which allows loading and picking cells from specific wells embedded on a chip.[65,66] Despite the utility of these existing platforms, they each require users to acquire specialized, often extremely expensive equipment to perform the assays, which hinders widespread adoption.

We introduce a new approach to collect and quantify single-cell secretions without crosstalk in monodisperse droplets formed by precisely structured microparticles, enabling high-throughput screening based on secretions (**Figure 2-1**). In our "dropicle" approach, uniform **droplets** are templated by **particles** through simple mechanical agitation induced by pipetting in bulk solution. Particles are structured with an open cavity enabling collection and protection of cells. Spherical gel particles have been used to template emulsions,[67,68] however, the lack of a cavity precluded use with mammalian cells, and no secretion assays were performed. In our system, cells are loaded into cavity-containing microparticles and adhere via integrin binding sites on the particle surfaces. Oil and surfactant are added and the suspension is agitated by pipetting to create incrementally smaller water-in-oil droplets. These resulting dropicles retain a fluid volume which is uniform and defined by the particle geometry. Secretions from

encapsulated cells are captured on the associated particles, and particles and associated cells and secretions are transferred back to an aqueous phase by breaking the emulsion, enabling downstream analysis and sorting that is compatible with standard flow cytometers. As a result, the end user can form uniform droplets without the need for microfluidics, eliminating the need for new expensive equipment or specialized skills that would otherwise need to be acquired to perform these assays. Standard flow cytometers have been widely available to most research labs and companies over the past several decades making sorting methods for dropicles easily

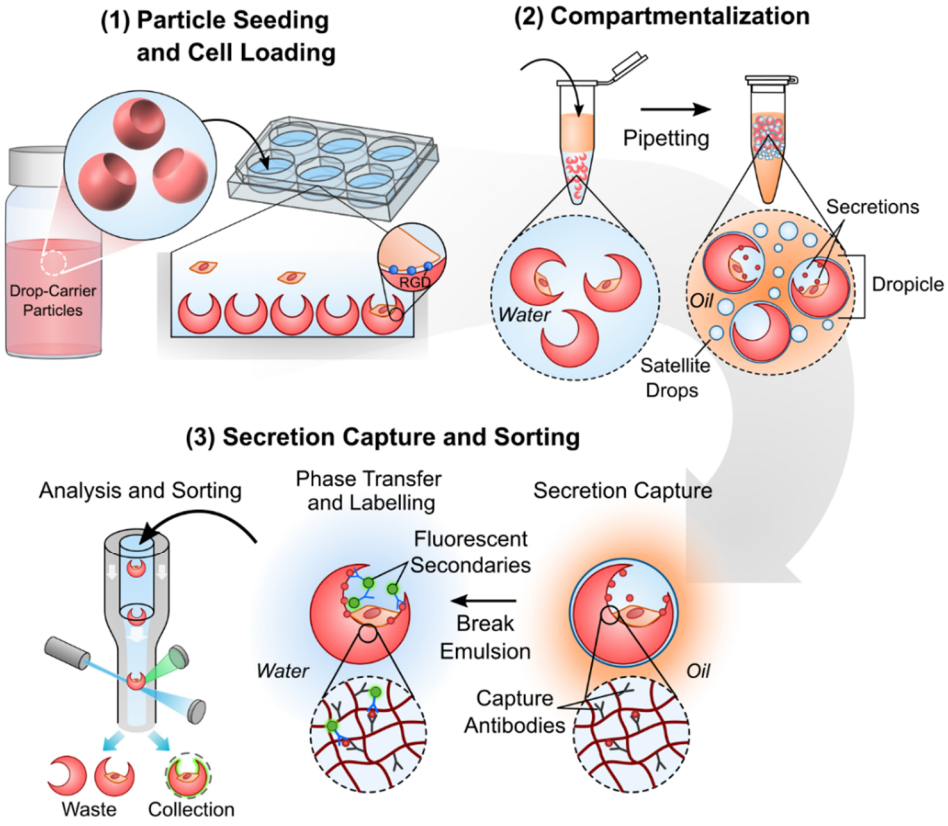


**Figure 2-1. Overview of dropicle-based single cell secretion screening platform.** (1) Prefabricated cavity-containing microparticles are seeded into a well plate and settle with their cavities remaining upright. Cells are seeded and adhere to the particle matrix via integrin binding sites (RGD). (2) Particles and associated cells are transferred into a tube and agitated by pipetting with biocompatible oil and surfactant to generate monodisperse compartments dictated by particle size (Dropicles). (3) Cells are incubated to accumulate secretions on associated particles and transferred back to an aqueous phase for labelling. Particle/cells/secretions can then be analyzed and sorted using high-throughput commercial flow cytometers.

accessible.[69] This dropicle platform has the potential to dramatically increase the accessibility of single-cell screening tools to researchers which can add functional dimensions to our understanding of cell biology as well as accelerate the development of antibody drugs, affinity-based diagnostics, and emerging cellular therapies.

## 2.2. **Results**

### 2.2.1. *Device free encapsulation of single cells into monodisperse droplets*

Our approach to encapsulate single cells in monodisperse drops requires structured microparticles with exposed cavities, biocompatible oils and surfactants, and simple pipetting steps. Structured hydrogel microparticles with a crescent-shaped cross-section are fabricated at high-throughput (~1000 $s^{-1}$) utilizing an aqueous two-phase system combined with droplet microfluidics as adapted from previous work (**Figure A-1-3**).[70] By tuning the fabrication parameters, we achieve highly monodisperse polyethylene glycol (PEG)-based drop-carrier particles (outer diameter CV of 1.5%, cavity opening diameter CV of 2.1%) that are further functionalized with arginine-glycine-aspartate (RGD) peptide for cell adhesion and biotin as a versatile handle for affinity capture. Apart from this initial fabrication step that used a specialized microfluidic device, all further experiments are performed utilizing only standard lab infrastructure. This is a critical feature of our platform as it enables the more complex microfluidic/particle fabrication work to be centralized and performed in advance. We envision that the end user can then directly use the pre-fabricated particles to perform the full single cell secretion assay workflow.

Cell seeding onto the particles uses standard pipetting steps followed by incubation. To seed cells within the particle cavities, a monolayer of drop-carrier particles is first pipetted onto

the bottom of a well plate. Due to the unique morphology of the particles, they settle with their cavities mostly upright (**Figure 2-2a**).[71] Cells are then seeded over the particles and allowed to settle with a sizeable fraction coming to rest in the particle cavities (>15%) (**Figure 2-2b**). It was noted that this seeding approach led to cell occupancies that closely followed Poisson statistics (**Figure 2-2c**), as is expected for loading of single cells into microfluidically-generated droplets.[72,73] Therefore, by controlling the cell seeding density, we can control occupancy such that most particles have either 0 or 1 cells associated with them.

By exploiting the structure of the microparticles, uniform droplets are formed via simple agitation steps with oil and surfactant. An aqueous solution of drop-carrier particles is first concentrated in a conical or microcentrifuge tube by centrifuging and aspirating the supernatant. A layer of biocompatible oil with surfactant is added and the suspension is then pipetted vigorously for 30 seconds to create smaller and smaller water-in-oil droplets. Eventually the droplet size is maintained by the outer periphery of the microparticle (**Figure 2-2d**). We find that, in agreement with minimal energy considerations[74], fluid from the cavity remains stably trapped by the hydrophilic drop-carrier particle. Any excess fluid in the suspension is partitioned into much smaller satellite droplets. The resulting emulsion shows two unique distributions; (1) small non-uniform satellite droplets and (2) monodisperse droplets each templated by single microparticles (Dropicles) (**Figure 2-2e, Figure A-4**). Importantly, we observe that only a small fraction of droplets contain multiple particles (<1%, **Figure 2-2f**).

For functional cell assays it is critical that cells remain viable during the dropicle formation and emulsion breaking process. Using calcein staining we demonstrate that the cell membranes remain intact during the emulsification steps (**Figure A-5**). Live/dead analysis of CHO cells following encapsulation and subsequent emulsion breaking shows high viability over

a 24-hour period (>80%) indicating that the workflow is biocompatible (**Figure A-5**). Further, we observe similar growth rates from cells expanded after dropicle release in comparison to cells

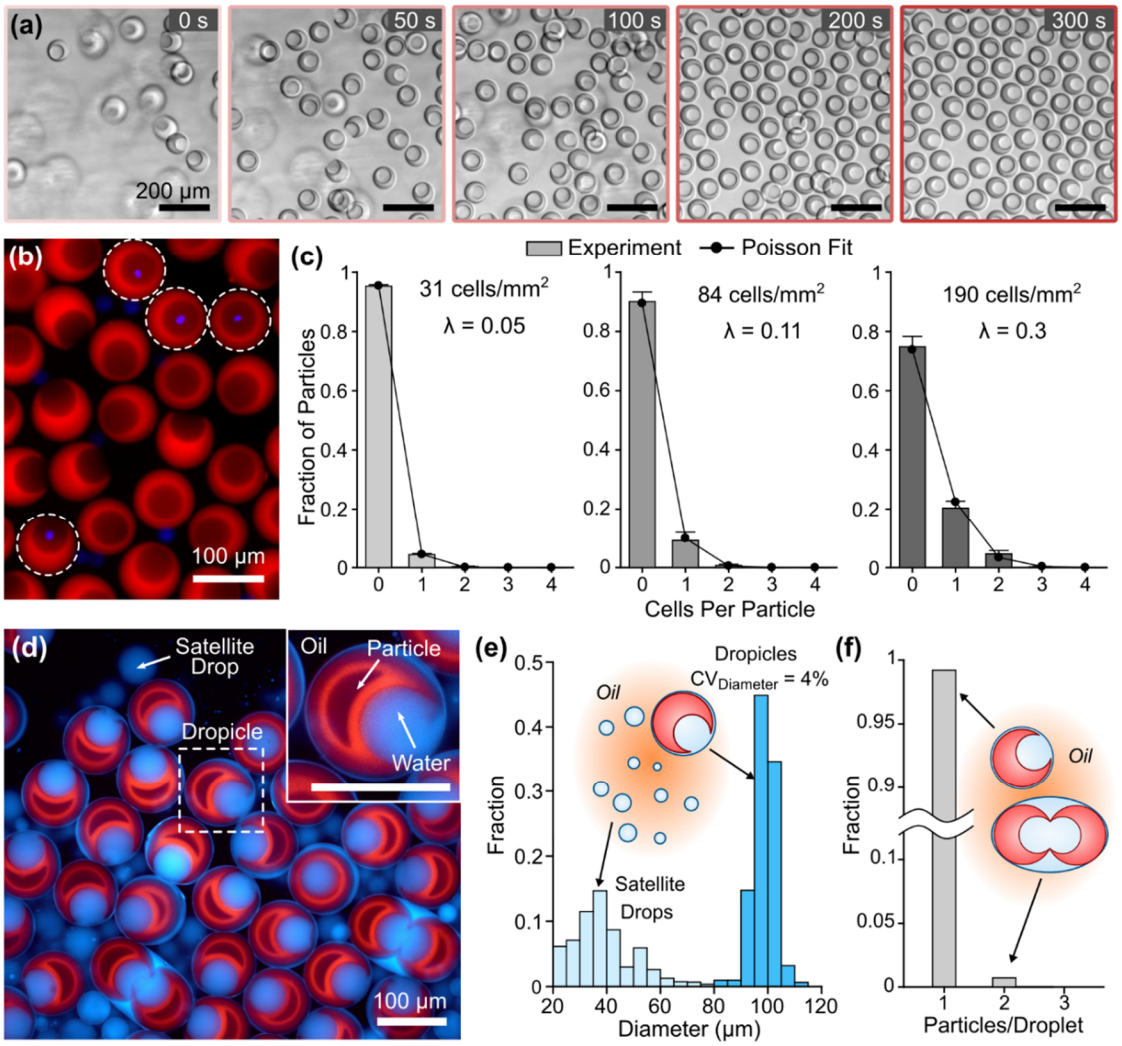


**Figure 2-2. Characterization of cell loading and dropicle formation.** (a) Particles are loaded into wells and settle with their cavities mostly upright due to their asymmetric morphology. (b) Cells are then seeded into the open cavities and adhere via integrin binding sites (RGD peptide) linked to the particle matrix. Fluorescence microscopy image of cells loaded into cavities where particles are labeled red and cell nuclei are labeled blue. (c) Cell loading closely follows single-Poisson statistics where λ is the average number of cells per particle. Loading fraction can be controlled by adjusting the seeding density. Error bars represent standard deviation across three separate samples. (d) Fluorescent image of dropicles formed by pipetting suspended particles with oil and surfactant. To aid in visualization drop-carrier particles were labeled with a red fluorophore and a large molecular weight dye (blue) was included in the water phase. (e) Droplet size analysis after emulsification shows two distinct subpopulations: smaller heterogeneous satellite drops and monodisperse dropicles (n = 561). (f) Nearly all droplets formed have either 0 or 1 particle associated with them, with only a small fraction (<1%) containing 2 or more particles per droplet.

seeded directly into a well plate. (**Figure A-5**).

### 2.2.2. *Single cell secretion analysis using dropicles*

Using the dropicle platform we demonstrate a device free workflow to perform single-cell secretion assays with minimal crosstalk (**Figure 2-3a**). Given the importance of selecting high antibody titer cell lines for therapeutic production,[75] we chose a Chinese hamster ovary (CHO) cell line that produces human IgGs targeting interleukin 8 (IL-8) and particles modified to capture human IgG as our model system. Cells are first loaded into the microparticle cavities and adhere via integrin binding sites as previously described. After initial cell seeding, particles and associated cells are collected and washed to remove background secretions. Particles are then coated with anti-human IgG Fc antibodies by binding to biotin groups linked to the particle matrix. Following this step, the particles and associated cells are rapidly compartmentalized via dropicle formation. The compartmentalized CHO cells are then incubated, and the secreted antibodies are captured onto the associated particle matrix. After incubation, the emulsions are broken and the particles with attached cells and secretions are collected and washed. The particles with the associated cells and secretions are then labeled with secondary fluorescent antibodies targeting the secreted anti-IL-8 antibodies. Using fluorescence microscopy, we confirmed retention of cells and associated secretion signal on the particle surface after recovering out of oil into an aqueous phase (**Figure 2-3b**).

We observe an increase in mean accumulated fluorescence signal on the particles that trends, as expected, with increasing incubation time and corresponding antibody production (**Figure 2-3c,d**). Using fluorescence microscopy we are able to measure significant signal over background (3 standard deviations) after 1 hour of incubation (**Figure 2-3e**). Interestingly, we

note across all incubation times that there are a sizeable population of cells (~25%) that have no measurable secretion signal (**Figure 2-3c,e**). Viability analysis of this population revealed that >50% of these cells were still alive indicating that the lack of signal is likely due to a fraction of the cell population no longer expressing the antibody production gene or secreting the produced antibodies (**Figure A-8**). Further we demonstrate that this assay workflow is compatible with the CHO cells after adapting them to suspension culture (**Figure A-7**). With suspension-adapted CHO cells we also saw distinct punctate signals on particles containing cells that was observable after as little as 1 hour.

Because of the heterogeneity across cell populations, preventing secretion cross-talk between particles is critical to enable quantitative analysis and sorting. Dropicle formation is key to preventing cross-talk of secretions as demonstrated by a side by side comparison of the secretion assay with and without the dropicle formation step. When secretions are captured on particles in bulk (without a surrounding oil), particles without associated cells show high secretion signals indicating significant cross-talk (8.2% of non-cell containing particles have signal above threshold) (**Figure 2-3d**). Conversely, with the dropicle formation step there are two visibly distinguishable populations, particles with and without secreting cells, and only 1% of particles without cells have signal above the cut off threshold. Minimizing the fraction of false positives is particularly critical when secretions can spill over into neighboring particles containing non-secreting cells that would contaminate downstream cultures or sequencing assays.

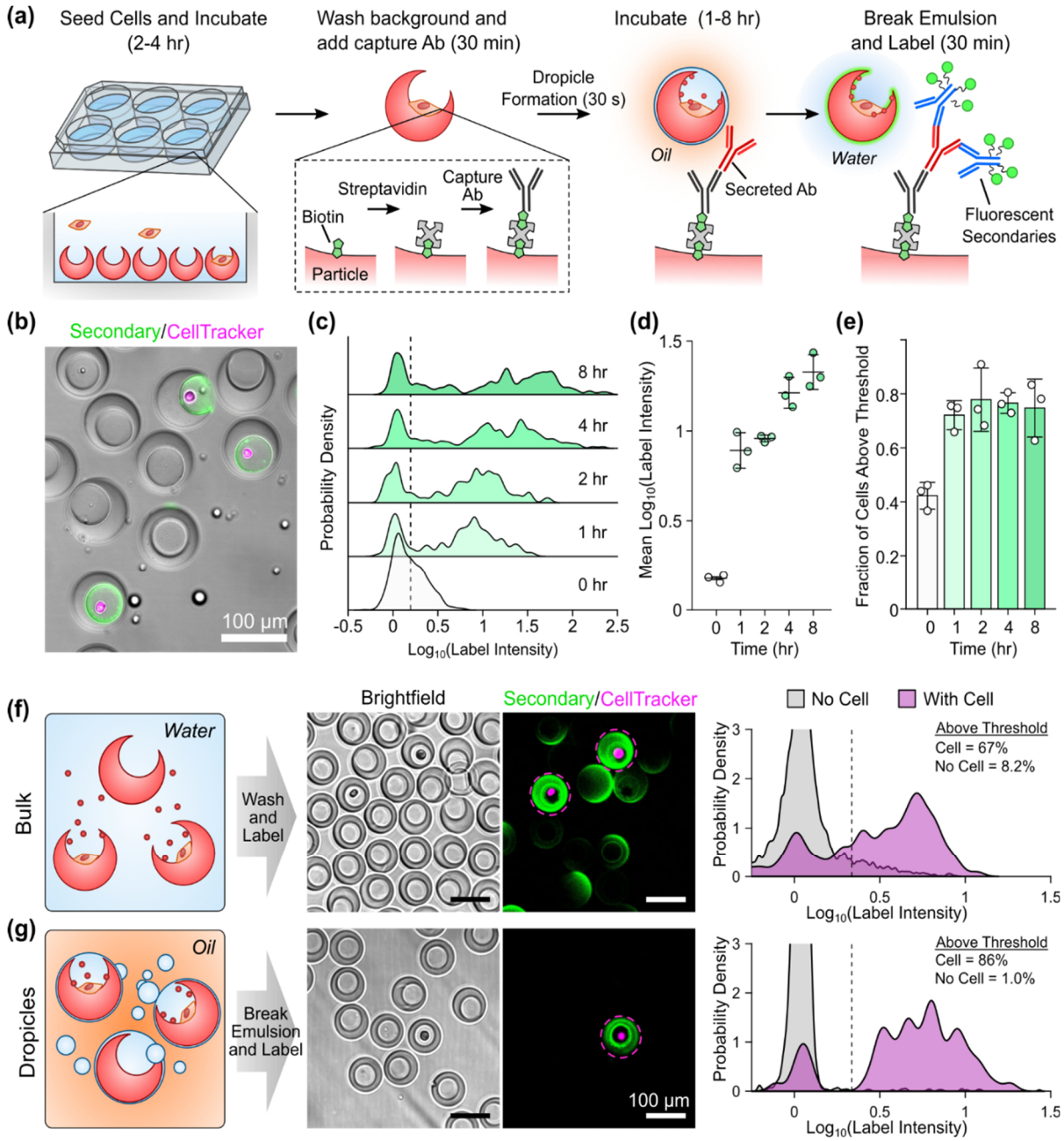


**Figure 2-3. Analysis of single-cell secretions using dropicles.** (a) Single cell secretion assay workflow. Cells are first seeded onto particles and washed. Biotinylated anti-human IgG Fc capture antibody is linked to the particle via biotin-streptavidin interactions. Dropicles are formed and cells are incubated inside. After secretion accumulation, emulsions are broken. Particles and associated cells are then washed and stained using fluorescent secondary anti-human antibodies. (b) Example image of particles with associated cells and secretion signal after performing full secretion assay. Fluorescent images are overlaid onto a brightfield image. (c-d) Sweep of incubation times shows increased accumulation of secretions over time as expected, providing further validation of the assay. Signal intensity of only particles with cells is shown. (d) Mean intensity is consistent across triplicate samples. (e) Fraction of cell population that is secreting human antibodies. Secreting criteria defined as 3 standard deviations above empty particle signal (dashed line shown in (c)). Significant signal over background is observed after as little as 1 hour of incubation. (f) Cross-talk is observed when the secretion assay is performed on particles without the dropicle formation

step. (g) Minimal cross-talk is observed when dropicle formation compartmentalizes cell secretions during the incubation step. Threshold in both (f) and (g) is set at 3 standard deviations above empty particle signal for the dropicle condition (g). Error bars represent s.d.

### 2.2.3. *Isolation of secreting subpopulation using FACS*

Following emulsion breaking, particles with attached viable cells are sorted based on secretion quantity using a commercial flow sorter. We performed secretion-based sorting with a mixed population of the anti-IL-8 producing CHO cells and non-producing CHO cells each labeled with a separate Cell Tracker$^{TM}$ dye (**Figure 2-4a**). After the secretion assay and prior to sorting, fluorescence imaging of the stained particles shows 100-fold higher signal on particles containing the antibody-secreting cells of interest compared to those containing non-secreting cells (**Figure 2-4b**). This further demonstrates the lack of cross-talk in our system as well as the specificity of the labels only to the secretions of interest. The particles with associated cells and secretions were then sorted based on the labeled secretion intensity (**Figure 2-4c**). Downstream analysis shows effective isolation of the sub-population of interest with high-purity (85-99%) (**Figure 2-4d-e**) over a range of target cell dilutions. In the most dilute case (1:1000) an enrichment ratio of 850X was achieved indicating the capability to isolate rare target cell events. Cells isolated using this approach can be expanded directly from the particle matrix enabling a streamlined workflow with minimization of trypsinization steps (**Figure A-5**).

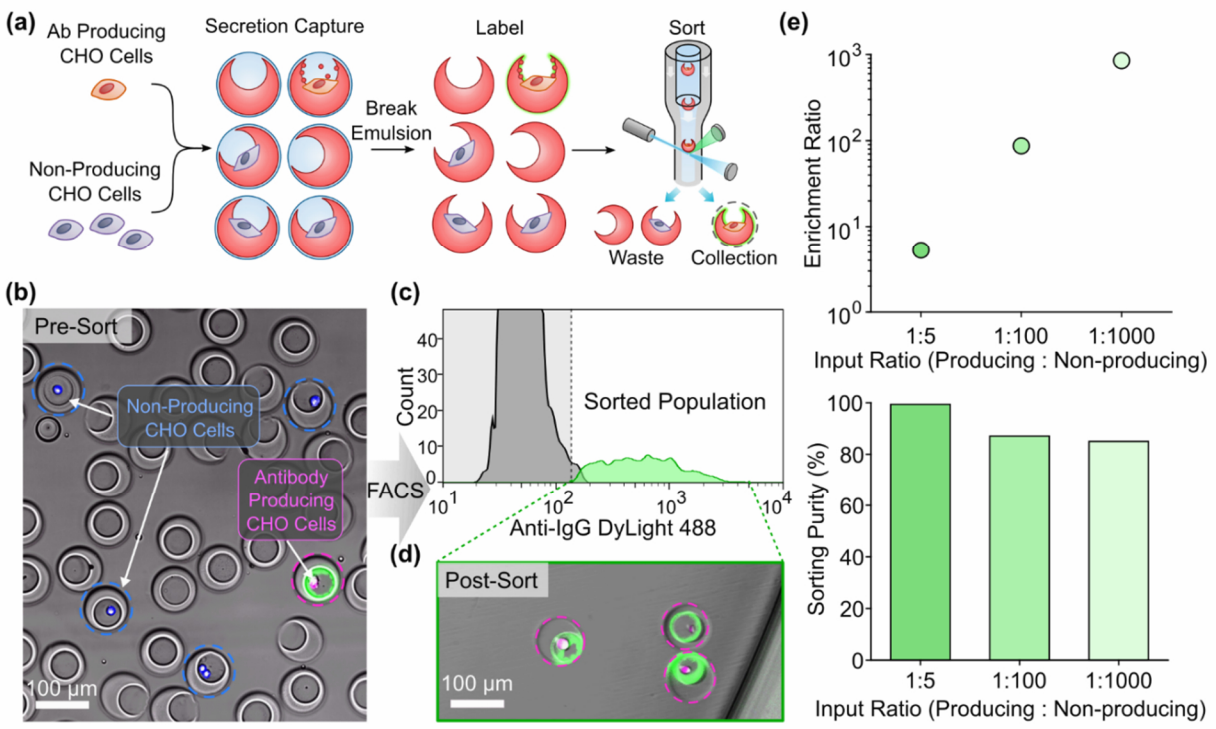


**Figure 2-4. Sorting of cells based on secretions using commercial fluorescent activated cell sorter (FACS).** (a) Selection of secreting cells of interest using FACS. Antibody (Ab) producing cells are mixed with non-producing cells (1:4 ratio), each stained with different colored Cell Tracker dyes and seeded on the particles. A secretion capture assay is performed as previously described and samples are then collected, stained for secretions, and sorted using a commercial flow cytometer. (b) Microscopy image of samples after staining shows particles with Ab producing cells (magenta) yield clear secretion signals (green) which are not observed for non-producing cells (blue). (c) Samples are sorted by gating on the peak fluorescence intensity of the secretion label channel. (d) Collected samples are then imaged and analyzed. (e) Spiked target cells were isolated across a range of initial fractions in a background of non-secreting cells (1:5 – 1:1000) and imaged to determine enrichment ratio and purity.

### 2.2.4. *Viable sorting of high antibody producing cells*

Sorted cells maintain the ability to produce antibodies at levels correlating with the mean intensity of initial secreted signal. In a separate set of experiments, we performed a secretion assay on human anti-IL8 producing CHO cells and selected out sub-populations based on level of secretion signal using FACS (**Figure 2-5**). Cells secreting antibodies were sorted in high-throughput (>200 events/s) by gating off both the fluorescently labeled secretion channel as well as CellTracker$^{TM}$ dye (**Figure 2-5a**). For each separate passage of cells analyzed (n = 4) we

sorted two sub-populations: (1) all particles with cells and detectable secretion signal above background and (2) particles with cells and the top 20% of antibody secretion signal. Microscopy images of the sorted particles and associated cells show successful isolation of secreting cells with signal proportional to their respective FACS gating (**Figure 2-5b**). The sorted sub-populations were seeded into a 96-well plate and expanded out of the particles over the course of ~10 days. Samples were then plated at the same cell density and bulk antibody production of the different subpopulations was measured by ELISA and compared with non-sorted control samples. We observed a 26% increase in total IgG production for the sorted sub-population 1 (all secreting cells) in comparison to the pre-sort control population (**Figure 2-5c**). This increase is most likely due to the removal of cells that are no longer secreting IgG following the sort, which was measured to be ~25% based on microscopy analysis (**Figure 2-3c**) as well as flow analysis (**Figure 2-5a**). For sorted sub-population 2 (the top 20% of secretors) we measured an average increase of 41% in total IgG production (n =4) with a maximum increase among the samples of 58% (**Figure A-9**), indicating the capability of the platform to select out functionally higher producing sub-populations that maintain the phenotype for at least 10 days.

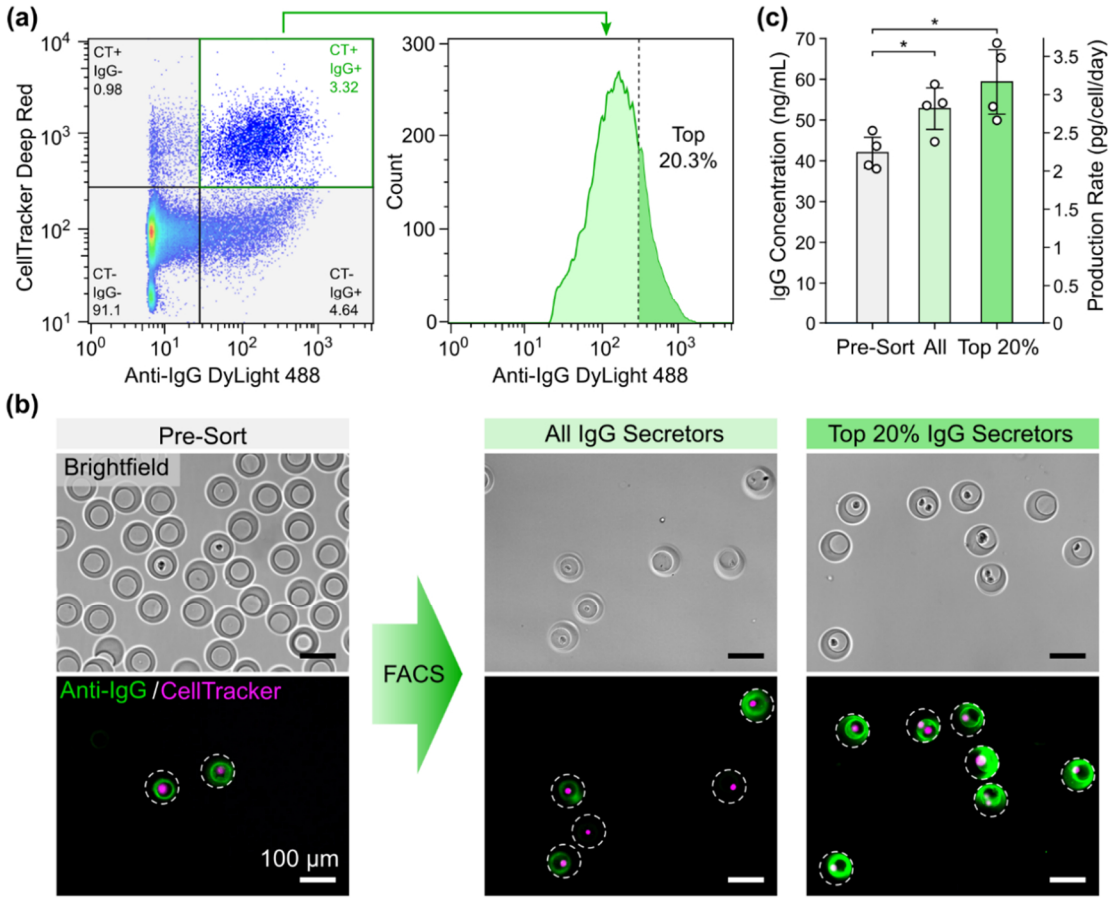


**Figure 2-5. Selection of high secreting cell sub-populations using FACS.** (a) The secreting population of cells were gated and sorted based on IgG secretion signal and CellTracker (CT) labelling. Both cells with any secretion signal disparate from background as well as the top 20% of secretors were separately sorted. (b) Microscopy images before and after sorting show enrichment of secreting cells with fluorescent intensity proportional to the selection criteria. (c) Isolated cells were expanded and bulk ELISA was performed to determine the production rate for the different sub-populations. Full experiment was performed with separate cell passages (n = 4). Statistical significance based on standard two-tailed *t*-test (*p<0.05). Error bars represent s.d.

## 2.3. **Discussion**

The dropicle platform provides specific advantages in sorting cells based on secretions, but also lays the foundation for the next generation of microfluidic assays on single cells and molecules without new instruments. We show that two key features of the dropicle platform allow for widely accessible analysis and sorting of cells based on secretions: (i) the ability to

form uniform compartments containing single cells in small volumes with minimal crosstalk using simple pipetting and no devices, and (ii) the compatibility of the drop-carrier particles with commercially available flow sorters such that viable cells can be sorted based on their associated secretions. Particles allow for seeding of cells into their open cavities and emulsification to form hundreds of thousands to millions of dropicles all in parallel using simple pipetting operations. Parallel encapsulation in < 1 min is an important differentiator from microfluidic techniques which often require tens of minutes to several hours to sequentially form droplets while cells remain mixed and secreting in the input sample volume.[33] Rapid emulsification minimizes cross-talk from cells secreting into the mixed input sample volume during the time over which secreting cells are encapsulated which is critical for enabling screening of large cell populations. Dropicle emulsification and analysis steps can also be more easily performed in a sterile environment (e.g. biosafety hood) using standard sterile plasticware (e.g. well plates, pipette tips), as opposed to bulkier equipment. Although microfluidics is used to manufacture the drop-carrier particles, the particles can be easily produced in batch (>10 million drop-carrier particles per batch, **Figure A-1**) and provided to other labs who do not have expertise in microfluidics. Shipping of particles is significantly more cost-effective and rapid than replicating microfluidic setups for generation and sorting of droplets. Further, the amount of additional expertise required to use the dropicle system is substantially lower than microfluidic based approaches.

The dropicle system is also compatible with commercial flow cytometers which enabled us to screen over 100,000 cells across the experiments described in this report at rates of ~100 events/second. This throughput is comparable to state-of-the-art microfluidic approaches and by further optimizing the loading of cells into the particles as well using higher-throughput FACS machines this throughput could exceed 10 million cells per day. Besides increasing availability

to labs without expertise in microfluidics or specialized commercial instruments, there are some unique advantages of this new approach for encapsulation of mammalian cells.

The structure and surface of the drop-carrier particles provide unique capabilities for tuning the number and type of captured cells, analysis of adherent cell secretions, and analysis and sorting of clonal colonies. The size and opening diameter of the cavity within a drop-carrier particle can be tuned (**Figure A-2**) to improve dropicle uniformity and general encapsulation efficiency of samples (**Appendix B**). By adjust the cavity size to be similar to size of the cells, it is possible to deterministically load single cells based on size exclusion effects (**Figure A-10**). This could enable more rapid screening because cell loading rates may not be limited by Poisson statistics. Besides structural changes to the particles, the surface of particles can also be functionalized with affinity agents that specifically enrich certain populations of cells, such as antibodies to CD3 that enrich T cells from a mixed population. The surface of the particle also enables the attachment and growth of adherent cell populations, such as the CHO cells used herein. Analysis of secretions from adherent cells can be challenging with other microfluidic techniques which require cells to be in suspension to flow into devices and sort afterwards. Adherent cells begin to undergo apoptosis when remaining in suspension and it is expected that secretion rates of biomolecules would change in this condition.[76] The inability to perform these assays has led to a dearth of information on the secretion phenotypes and heterogeneity of adherent cells with important secretion products in health and disease, such as mesenchymal stem cells, glandular epithelial cells, endothelial cells, glial cells, and even adherent bacterial biofilms. Further, in the dropicle system, when single cells are initially seeded onto particles they adhere and grow without nutrient limitations (**Figure A-5**). The clonal colonies can then be encapsulated to form dropicles, enabling high-throughput screening based on the combination of

growth and per cell secretion (i.e. overall biomass produced per unit time), potentially overcoming previous challenges in cell line selection in which growth and biologic production can be in a trade-off relation.[37]

Sorting based on secretions extends beyond selection of high antibody-titer cell lines to many applications of importance in life sciences and biotechnology. Discovering high affinity mAb therapeutics relies on the selection of B cells producing antibodies with high affinity amongst a large background.[57] The activity of immune cells is largely connected to their secretion profiles, which direct communication and effector functions and can be better studied by sorting out specific sub-populations for further functional testing in vivo or in vitro. The effectiveness of chimeric antigen receptor-T cell batches also appears to depend on a multifunctional secretion of cytokines, such that sorting populations based on secretion profiles may enhance therapeutic activity.[13,77] Finally, processes of directed evolution of cell products and cells themselves can benefit from larger numbers of clones being screened, mutagenized, and expanded across multiple cycles using an efficient process relying on standard equipment and expertise.[16]

More broadly, our new approach to encapsulate single entities into uniform compartments with a solid phase can enable a centralized “lab on a particle” platform for a number of single-cell and single-molecule assays. Encapsulation is a key component for single-cell nucleic acid sequencing. Clonal colonies of bacteria, yeast, or algae producing engineered proteins (e.g. fluorescent proteins) can also be maintained in dropicles and sorted based on desirable features (e.g. intensity at particular excitation/emission wavelengths). Moving beyond cells, the compartments formed can enable digital nucleic acid amplification assays and immunoassays, where the solid phase provides potential for barcoding and capturing of

amplified assay signals. Given the ability to rapidly deploy our approach with established lab infrastructure we anticipate widespread applications of lab on a particle technology across a range of these single cell and single molecule assays in the near future. Rapid deployment across the world is of particular importance during emerging pandemics, enabling collective distributed research and development, and removing the bottlenecks of only a few skilled groups being able to contribute to key points in therapeutic and diagnostic pipelines.

## 2.4. **Methods**

**Fabrication of drop-carrier particles.** Particles were fabricated using a standard PDMS microfluidic flow focusing droplet generator. A PEG phase comprised of 17.5% w/w 4-arm PEG-Norbornene (Sigma), 2% w/w LAP (Lithium phenyl-2,4,6-trimethylbenzoylphosphinate,sigma), and 0.5 mg/ml Biotin-PEG-thiol (5000 MW, Nanocs) in Phosphate Buffered Saline (PBS, pH7.2) was co-injected with a dextran phase comprised of 20% w/w 40 kDa dextran (Sigma), 1.3% w/w DTT (dithiothreitol, Sigma), and 5 mM RGD peptide (Ac-RGDSPGERCG-NH2, Genscript) in PBS at a rate of 8 µL/min and 2.67 µL/min, respectively using syringe pumps (Harvard Apparatus PHD 2000). An oil phase comprised of Novec 7500 (3M) and 0.25% w/w PicoSurf (Sphere Fluidics) was injected at a rate of 42 µL/min to partition the aqueous phases into monodisperse water and oil droplets. PEG and Dextran polymers phase separated on chip after approximately 5 seconds. The PEG phase was crosslinked with focused UV light through a DAPI filter set and 4X objective (Nikon, Eclipse Ti-S) at a power of 50 mW/cm$^2$ over an approximate duration of 1-3 seconds near the outlet region of the microfluidic device. Crosslinked particles were collected and oil and dextran were removed using a series of washing steps. Briefly, excess oil was removed by pipetting and a

layer of PBS was added on top of the remaining emulsions. A solution of 20% v/v perfluorooctanol (PFO, Sigma) in Novec 7500 was then added to destabilize the emulsions and transfer particles to the PBS phase. Excess oil was removed and samples were washed 2X with Novec 7500 to remove remaining surfactant. Novec 7500 was removed by pipetting and residual oil was removed by washing 2-3X with hexane (Sigma). Samples were then washed 3X with PBS to remove dextran from the system. For cell experiments particles were sterilized by incubating in 70% Ethanol overnight. Particles were then washed 5X with a storage solution comprised of PBS + 0.1% Pluronic F-127 (Sigma) +1% penicillin/streptomycin (Invitrogen) and stored in a conical tube at 4°C.

**Particle seeding and cell seeding characterization.** Stock drop-carrier particles were first concentrated in a conical tube by centrifugation and supernatant was aspirated. Particles were then fluorescently labeled by diluting at a 1:1 ratio with PBS containing 10 µg/ml of Alexa Fluor 568 streptavidin (Fisher Scientific) and incubating for 10 min. Particles were washed 3X with PBS and then dispersed in a well plate at a concentration of 7.5 µL of concentrated particles per cm of well surface area. Particles were then allowed to settle for 10 min. CHO cells pre-stained with Hoechst were then seeded at a range of concentrations (31-190 cells/$mm^2$) into the well by carefully pipetting evenly across the well area. Cells were allowed to settle for 15 min and then imaged using a fluorescent microscope. Loading statistics was calculated using custom image analysis algorithms in MATLAB. Particles were first identified using the particle fluorescence channel and cell number was calculated by counting nuclei number within each particle cavity.

**Dropicle formation and characterization.** Drop-carrier particles were suspended in DMEM base media (Invitrogen) and then concentrated by centrifuging at 300 g for 2-3 minutes and aspirating supernatant. An oil phase comprised of Novec 7500 and 2% w/w PicoSurf was added to the particle suspension at approximately 2X the remaining volume. The sample was then vigorously pipetted for 30 s (~50 pipettes) using a 200 µL micropipette (Eppendorf). The resulting water-in-oil emulsion was then carefully transferred into a PDMS reservoir by pipetting and imaged. Size distribution characterization was then performed using custom image analysis algorithms in MATLAB. For the fluorescent images shown in **Figure 2-2d**, particles were first labeled with Alexa Fluor 568 streptavidin and the DMEM was replaced with PBS containing 2 mg/ml fluorescein isothiocyanate-dextran (500k MW, Sigma).

**CHO K1 and CHO DP-12 cell culture.** All cells were cultured in incubators at 37°C and 5% $CO_2$. CHO K1 cells (ATCC CCL61) were cultured in F12 base media (Invitrogen) supplemented with 10% fetal bovine serum (FBS, Invitrogen) and 1% penicillin/streptomycin (Invitrogen). CHO DP-12 cells (ATCC CRL-12445) were maintained according to manufacturer's specifications. Cell culture media was comprised of DMEM (Invitrogen) supplemented with 10% FBS, 1% penicillin/streptomycin, 0.002 mg/ml recombinant human insulin (Sigma), 0.1% Trace Elements A (Fisher Scientific), 0.1% Trace Elements B (Fisher Scientific), and 200 nM Methotrexate (MTX, SIGMA). Suspension adapted CHO DP-12 cells were cultured in TC42 base media (Xell) supplemented with 1% penicillin/streptomycin, 0.002 mg/ml recombinant insulin, and 200 nM MTX.

**Cell viability characterization.** 30 µL of concentrated drop-carrier particles and 48k CHO DP-12 cells were suspended in media and sequentially seeded into individual wells of a 12-well plate. A separate well plate control sample containing no particles was prepared in parallel. Cells were allowed to adhere for 4 hours. Samples containing both the cells and particles were transferred into a 15 ml conical tube, exchanged with fresh media and then concentrated via centrifugation. 100 µL of Novec + 2% w/w PicoSurf was added to the concentrated sample and pipetted for 30 s to encapsulate the particles and associated cells into dropicles. 150 µL of light mineral oil was added on top of the samples to mitigate evaporation during incubation. Samples were then incubated for 2, 12, and 24 hours in an incubator at 37°C and 5% $CO_2$. To recover cells back into an aqueous phase excess oil was first removed via pipetting and several ml of media was added on top of the emulsions. To destabilize the droplets 50 µL of 20% v/v PFO in Novec 7500 was then pipetted on top of the emulsion layer and the sample was gently agitated. After 5 min most of the droplets were merged and particles and associated cells transferred into the bulk media phase. Optionally, samples can be centrifuged for 15-30 s at 200g to coalesce remaining droplets. The suspension of particles and cells were then transferred by pipetting into a separate conical tube. Samples were washed with PBS and then sequentially stained with calcein AM and propidium iodide. Particle samples were transferred back into a well plate, imaged, and then analyzed in MATLAB to determine cell viability statistics.

**Cell secretion assay.** To identify cells during downstream analysis CHO DP-12 cells were first stained with CellTracker™ Blue CMAC Dye (Thermo Fisher). Particles and cells were seeded into a 12-well plate as described above and then incubated at 37°C for 2 hours to allow cells to adhere to the particles. Particles were then recovered by tilting the well plate and transferring by

pipetting. In order to remove unattached cells from the background, samples were strained using a 37 µm reversible cell strainer (STEMCELL Technologies) and then particles were recovered by flipping the cell strainer and washing with a washing buffer comprised of PBS ($Ca^{2+}$,$Mg^{2+}$), 0.5% BSA (GeminiBio), 1% penicillin/streptomycin and 0.05% Pluronic F-127. To reduce sample loss all conical tubes and pipette tips were first precoated with washing buffer prior to handling particle containing solutions. After recovering from the well plate, samples were washed 2X by centrifuging particles and associated cells at 300 rpm for 3 min, aspirating, and then resuspending in washing buffer. Particles were then labeled with streptavidin (Thermo Fisher, 434302) by adding 0.415 ng per µL of concentrated particle solution and incubating for 10 min. Samples were then washed 3X with washing buffer and resuspended. Particles were then labeled with Biotin Anti-FC (Thermo Fisher, A18821) by adding 75 pg of the antibodies per µL of concentrated particle solution and incubating for 10 min. After incubation, samples were washed and resuspended in CHO DP-12 media. After re-concentrating, samples were compartmentalized by pipetting with oil and surfactant as described above to create dropicles. Samples were then incubated for a range of times 0, 1, 2, 4, and 8 hours to allow cells to secrete and to facilitate capture of secreted antibodies onto the associated particle matrix via Anti-FC sites. After the incubation period, particles and associated cells were transferred back into media by breaking the emulsions (see live dead section). Samples were then washed and captured secretions were stained with Goat anti-human IgG H&L (Dylight® 488, Abcam ab96911) at a final concentration of 30 pg per µL of initial concentrated particle solution. After 30 min of staining, samples were then washed 5X with a solution of PBS ($Ca^{2+}$, $Mg^{2+}$), 2% FBS, 1% penicillin/streptomycin and 0.05% Pluronic F-127 and optionally stained with propidium iodide. Samples were then imaged in both brightfield and fluorescence channels in a well plate. To

characterize secretion amount per particle a custom MATLAB algorithm was used to identify particles in brightfield and then count the number of cells, check for the presence of dead stain, and integrate the total secretion label fluorescence intensity for each particle.

**Secretion cross-talk assay.** To analyze potential cross-talk in our single cell secretion system, samples were prepared as described in the cell secretion assay section with several modifications to the protocol. Two sets of samples were prepared, a control sample that was incubated in bulk solution and one incubated after dropicle formation. Prior to the incubation step a separate suspension of particles containing no cells and tagged with Alexa Fluor 647 streptavidin were mixed into the samples. This was done in order to ensure signal on empty particles that was measured did not arise from cells that may have detached from the particles during various steps of the assay. Samples were washed and capture sites were then added. The bulk samples were then left to incubate in media while the dropicle samples was emulsified in oil via pipetting. After incubating for 15 hours samples were recovered and washed with washing buffer, stained, and imaged as described in the cell secretion assay section. The amount of cross talk was determined by comparing secretion staining intensity on particles with cells with the intensity on the control particles.

**Secretion based cell isolation using FACS.** Samples were prepared as described in the cell secretion assay with the following modifications. CHO DP-12 cells and CHO K1 cells were prelabeled with CellTracker$^{TM}$ Deep Red and CellTracker$^{TM}$ Blue (Thermo Fisher). After labelling, cells were mixed together at various ratios (1:5, 1:100, 1:1000) and loaded into particles (Seeding density ~84/mm$^2$, lambda ~0.1. All remaining secretion assay steps were as

previously described. After labelling secretions on samples with fluorescent secondary antibodies, samples were sorted using a FACS machine (BioSorter, Unionbio). Samples were excited using both 488 nm and 561 nm lasers. Events were triggered based on particle absorbance from the 561 nm laser. Single particle events were gated based on time of flight. Particles with secretion signal were then sorted by thresholding the peak intensity height collected through a 543/22 nm filter. Samples were sorted directly into a 96-well plate and imaged with a fluorescence microscope.

**Quantification of high producers after sorting.** Samples were prepared as described in the cell secretion assay section. After labelling secretions, a fraction of each sample was kept and imaged using fluorescence microscopy. Remaining samples were then sorted using a FACS machine (On-Chip Sort, On Chip Biotechnologies). Samples were excited with both a 488 nm and 637 nm laser. Particle events were screened based on the forward and side scatter. Particles positive for both cells and secretion signal were gated based on peak fluorescence height collected through a 676/37 nm emission filter and a 543/22 nm emission filter respectively. Two sub-populations were sorted for each sample: (1) particles with cells and positive secretion signal, (2) particles with cells and the top 20% of positive secretion signal. Collected samples were plated and expanded for >10 days. To quantify antibody production of the isolated sub-populations, 30k cells from the expanded sub-populations as well as un-sorted control samples were plated into a 48-well plate. After cells attached the samples were washed, replaced with 400 µL of fresh media, and incubated for 6 hours. Supernatant was then collected and total human IgG amount was measured using ELISA (IgG (Total) Human ELISA Kit, Invitrogen, BMS2091). Production

rate was calculated based off the measured IgG concentration, incubation time, and initial number of cells seeded.

# Chapter 3. Scalable high-throughput production of hydrogel particles

In the previous chapter I discussed how structured microparticles can be used to democratize single-cell secretion assays. Moving forward a key aspect to translating this technology will be manufacturing these particles at larger scale. In this chapter I will discuss my work using a scalable microfluidics approach to fabricate uniform spherical hydrogel particles at high-throughput. To show the biocompatibility of these particles we demonstrate application of these particles for use in tissue engineering applications. In following chapter, I will discuss approaches to adapt this technique to also fabricate structured microparticles in high-throughput.

## 3.1. **Introduction**

Materials that can seamlessly integrate with surrounding tissue at the microscale and are easily delivered *in situ* can be broadly useful in long-term regeneration of functional tissue, development of continuous implanted sensors, and sustained drug delivery.[78,79] Recent work has demonstrated enhanced tissue integration into interconnected microporous scaffolds formed from monodisperse microgel (μgel) building blocks covalently linked in situ, resulting in accelerated wound healing.[80] This general microporous annealed particle (MAP) scaffold approach has been demonstrated with a range of materials including synthetic poly(ethylene) glycol (PEG)-based polymers, and naturally derived polymers such as hyaluronic acid and gelatin methacrylate.[80–85] Highly uniform microgel building blocks, which can be generated using microfluidic droplet generators, enable fabrication of a controlled interconnected microporous environment which facilitates enhanced cell proliferation and cell network formation.[86]

To date, methods used to produce monodisperse microgel building blocks for the formation of microporous scaffolds are fundamentally limited by their low throughput and poor

scalability.[80,82,84,85] This limitation creates a barrier for widespread adoption in research labs as well as translation to clinical settings. An optimal approach would maintain the precise size control of microfluidics while allowing for the potential to scale to larger production scales. Furthermore, this approach should ensure highly uniform physicochemical properties, such as number of integrin binding moieties and local scaffold stiffness, among building blocks to maintain a homogeneous environment to precisely control interactions with cells and surrounding tissue. With the properties of each building block precisely controlled, mixtures of modular building blocks can be used to create well-defined larger-scale structural, mechanical, and chemical functionality.

Previous work has demonstrated the potential to scale microfluidics for droplet generation and particle fabrication.[87–93] These methods typically rely on light-reactive chemistries to induce crosslinking downstream of droplet generation. However, the high diffusivity of radical scavenging oxygen within standard oil phases can lead to non-uniform crosslinking, making it difficult to ensure homogeneous physicochemical properties.[94] Another common approach relies on mixing of a precursor and crosslinker prior to formation of particle templates.[80,82,95] However, this approach is generally difficult to parallelize due to the requirement of additional mixing steps and routing of multiple input streams. Further, fouling can occur at the interface between the crosslinking species prior to droplet formation making the approach ill-suited for more reactive chemistries, effectively limiting the range of material stiffnesses that can be explored (**Figure C-1**).

Herein we describe an approach to fabricate highly uniform microgel building blocks in a continuous scalable high-throughput manner, enabling formation of highly modular microporous environments for cell and tissue growth **(Figure 3-1)**. Hydrogel precursors are injected into a

parallelized step emulsification microfluidic device at a lowered, non-reactive pH to generate uniform spherical microgel templates. We then implement a unique pH modulation approach to induce controllable, uniform crosslinking of the microgel building blocks. This approach achieves consistent production for over 12 hours in a high-throughput manner, demonstrating over an order to two orders of magnitude higher production rate than similar works (**Table C-1**).[80–85] We demonstrate the functionality of the fabricated microgels to create MAP scaffolds *in situ* and independently modulate the stiffness to investigate cell behavior. Lastly, we demonstrate the modularity of this system to create injectable cell-laden mechanically heterogeneous scaffolds.

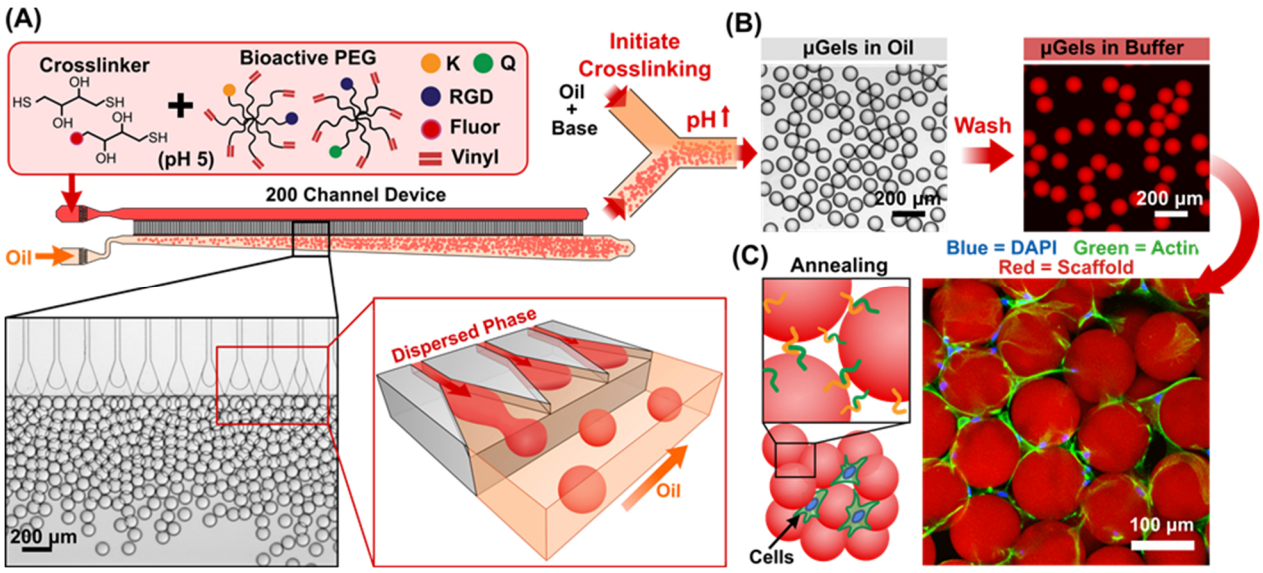


**Figure 3-1 Overview of µgel production and in situ scaffold formation.** (A) Well-mixed bioactive hydrogel precursors and crosslinkers are injected into a parallelized step emulsification device at a non-reactive pH. (B) Organic base is added to the oil phase in flow to increase pH and induce crosslinking. Crosslinked µgels are separated from the oil phase and washed. (C) µgels are seeded with cells in solution and covalently linked together in situ via enzymatic reaction between K and Q peptides to form cell-laden microporous scaffolds.

## 3.2. **Results and Discussion**

### 3.2.1. *Scalable Production of Monodisperse µgel Templates*

Parallelization of droplet production is enabled by the unique droplet formation mechanism in step emulsification. An aqueous phase is flowed among hundreds of identical channels which intersect a taller reservoir channel containing an oil phase. Droplet formation is facilitated by the sudden expansion in channel height at the end of each channel. The larger curvature of the expanding droplet leads to a reduction in Laplace pressure driving additional flow of fluid into the forming droplet and triggering an instability that drives the pinching of a single droplet into the oil phase **(Figure 3-2A)**.[96] To improve uniformity and throughput, the channels were also designed to have a gradual expansion. This achieved lower variance in droplet diameter, especially at higher frequencies, compared to a sharp expansion region (**Figure C-3**).[96–98] Since the driving mechanism of pinch off is not due to an active pinching oil flow, droplet size is insensitive to flow rates, outside of the jetting regime, where droplet filling has a long timescale compared to the instability mechanism [97–100] (**Figure 3-2B**). This unique feature enables highly compact parallelization, allowing for hundreds of droplet generators within a small footprint while maintaining high droplet uniformity (CV<3%). In contrast, droplets produced using flow focusing devices are sensitive to flow rates, making it difficult to parallelize while maintaining monodispersity. Although it has been shown this issue can be mitigated through careful design and optimization,[92,101,102] in general these approaches require significant fine tuning for new operating fluids and droplet sizes. We demonstrate production rates (**Figure 3-2B**) , an order, to multiple orders of magnitude higher then µgels formed using standard flow focusing devices[80,82,85] as well as parallelized flow focusing devices used for similar applications (**Figure 3-2C**, **Table C-1**).[84,103]

Due to the geometry-driven droplet generation, droplet size is invariant to the concentration of the gel precursor, allowing for production of the same sized µgels with various compositions using a single device (**Figure 3-2E**). To change the size of the µgels, the geometry of the device can be modified. For example, reducing the channel height to 11 µm produced ~50 µm droplets compared to ~90 µm droplets with a channel height of 25 µm (**Figure 3-2E**). In flow focusing devices, the droplet size is heavily dependent on solution viscosity, requiring tuning of flow conditions for each new species.[104]

We observe similar maximum production rates for both low and high concentration PEG solutions using our parallelized device (**Figure 3-2B**). This was attributed to the fact that for higher concentration solutions, the dispersed phase tends to fill the channels more evenly resulting in more efficient utilization of the parallel channels (**Figure C-4**). In the case of the lower concentration solutions less even flow was observed. This led to crowding of droplets in different regions of the collection channel, increasing the chance of droplet coalescence.

For this design the production throughput was not limited by maximum production frequency of each of the individual channels (jetting transition), but instead by crowding effects of already generated drops which lead to droplet coalescence. By optimizing channel design and/or using droplet buoyancy to reduce crowding effects and improve even flow,[38] we extrapolate that throughputs of 30 mL/hr can theoretically be achieved while maintaining high monodispersity (CV<3%) (**Table C-2**). Further, previous work has demonstrated parallelization of over 10,000 channels on a single chip,[105] indicating potential to scale to L/hr production rates.

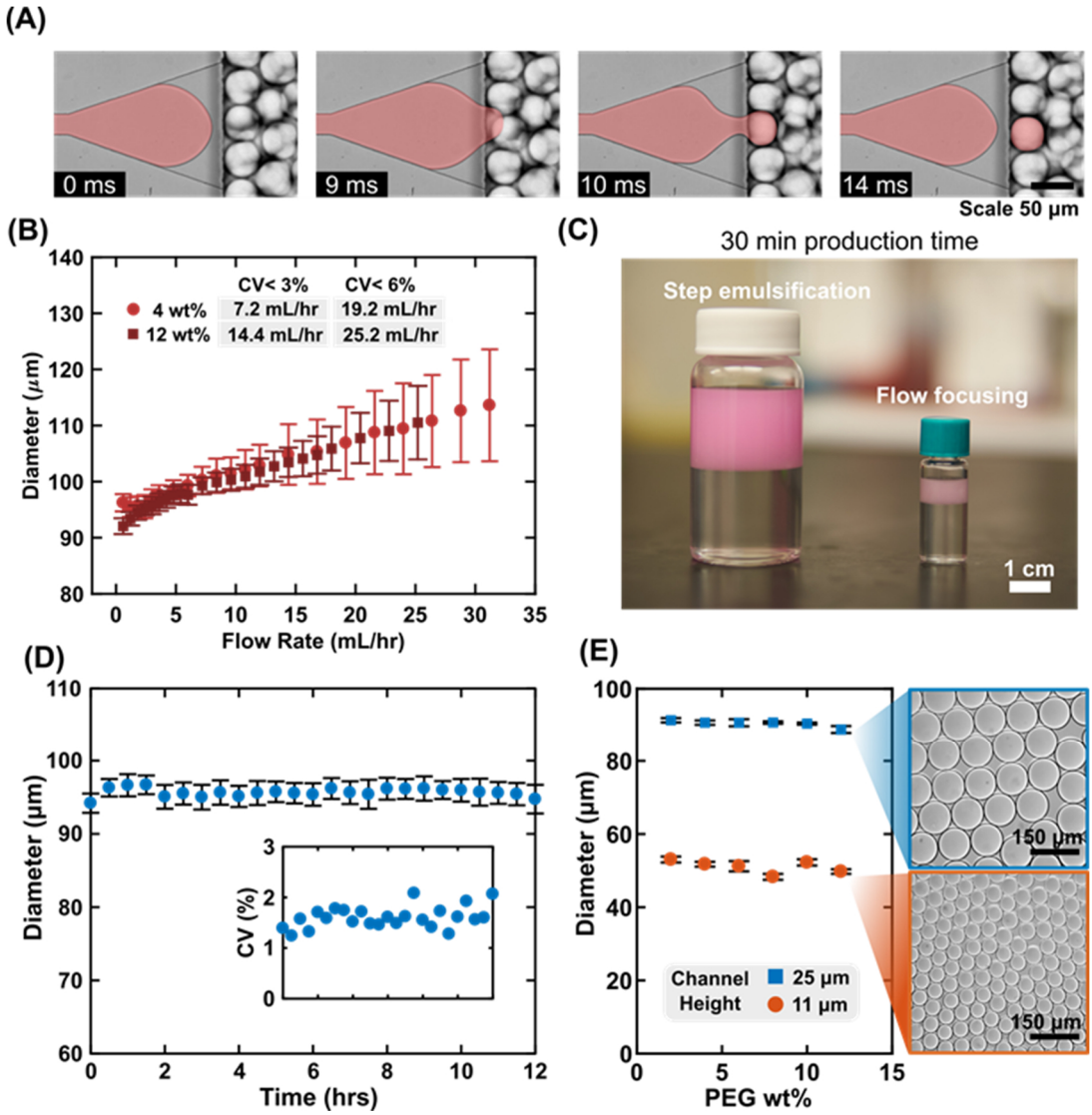


**Figure 3-2 Characterization of droplet formation with step-emulsification device.** (A) Droplet formation process captured with a high-speed camera. Gel precursor is false colored red to aid in visualization. (B) Droplet size is invariant over a large range of flow rates. Max throughput of the droplet generator is minimally affected by the PEG concentration in the dispersed phase. (C) Visual comparison of the production rate of the parallelized step emulsification device vs. a flow focusing device (14.4 mL/hr and 0.6 mL/hr respectively). Rhodamine-dextran added to gel precursor for visualization. (D) Production is robust with consistent droplet formation and uniform size over a 12 hr period. (E) Droplet size is invariant to the viscosity of the dispersed phase and can be tuned by adjusting the device geometry.

### 3.2.2. *Controlled Crosslinking via pH Modulation*

To controllably induce crosslinking of the precursor droplets into PEG µgels downstream of droplet generation, we implemented a unique pH modulation approach **(Figure 3-3A)**. The pH

of the dispersed droplet phase can be altered through the addition of organic base/acids in the continuous phase. Typically this approach has been used in microfluidics to release calcium ions to induce crosslinking of alginate microgels.[106,107] Herein we extend this approach to covalently crosslink synthetic multi-armed poly(ethylene) glycol-vinyl sulfone (PEG-VS) polymers with a dithiol crosslinker via Michael addition reaction. For this study we used dithiothreitol (DTT) as our crosslinker, although other crosslinkers such as PEG-dithiol or cysteine-terminated matrix metalloprotease-sensitive peptide sequences could be used. Gel precursor solution was injected into the droplet generator at pH 5, such that the thiol groups on the crosslinker molecules remain predominantly protonated, inhibiting the Michael addition reaction which relies on a deprotonated thiol to act as a nucleophile (**Figure 3-3A**).[108] Downstream of the droplet production a second oil phase containing an organic base (triethylamine) was co-flowed with the droplet suspension to increase the pH, deprotonating the thiol groups and initiating the crosslinking of the μgels (**Figure C-5**).

The deterministic partitioning of organic base from oil to water enabled precise tuning of the pH in droplets by adjusting the amount of organic base in the oil phase (**Figure C-6**). To evaluate the level of pH control, we generated droplets with a dispersed phase comprising a pH sensitive indicator dye dissolved in a slightly acid buffer solution (**Figure 3-3B**). Various amounts of organic base were then added through the oil phase and pH was measured indirectly using a color camera. The pH change among droplets was highly uniform with less than 1.1% variation in final pH over a range of target values, thus guaranteeing uniform gelation kinetics across μgels (**Figure 3-3B Inset**).

Utilizing this pH modulation approach, we were able to robustly fabricate μgels with a range of material properties (**Figure C-8**) while maintaining uniformity over an extended period.

Specifically, we show consistent production of gel droplet precursors over a 12-hour period with no clogging and no fluctuation in size (**Figure 3-2D**). After crosslinking and washing steps μgels remain monodisperse, with only a slight decrease in uniformity observed among μgels formed using lower concentrations of the hydrogel precursor (**Figure 3-3C**). This was attributed to the fact that the lower concentration gels have a slower reaction rate leading to a higher probability of individual μgels coalescing together before complete gelation occurs.

One advantage of our gelation approach is the relative ease in which high crosslinking uniformity is achieved. To evaluate the uniformity we measured the crosslinking visually using fluorescence microscopy as previously reported.[109] Specifically, we conjugated fluorophores onto our gel crosslinkers and measured both the total intensity as well as line intensity across populations of μgels (**Figure 3-3D,E**). Total intensity had less than a 9% variation (comparable to the variation in volume) and intensity profiles showed high spatial agreement with a theoretical model of uniform crosslink density (**Equation C-1**). In contrast, approaches which rely on injection and mixing of precursor and crosslinker solutions on chip can be susceptible to variations in flow ratios of reactive species leading to non-uniform populations (**Figure C-2**). Further, light-based approaches to control gelation are susceptible to population variation due to non-uniform spatial excitation from the light source and refracting surfaces. Due to the high permeability of radical scavenging oxygen in oil, local variation in crosslinking within individual μgels is difficult to avoid; [94] although it can be mitigated via nitrogen purging and free radical-mediated thiol-ene chemistries.[110]

Uniform crosslinking leads to the ability to better define the properties of unique microgel building blocks, such as stiffness. This is critical to ensure a well-controlled environment for cell culture and integration into modular scaffolds.

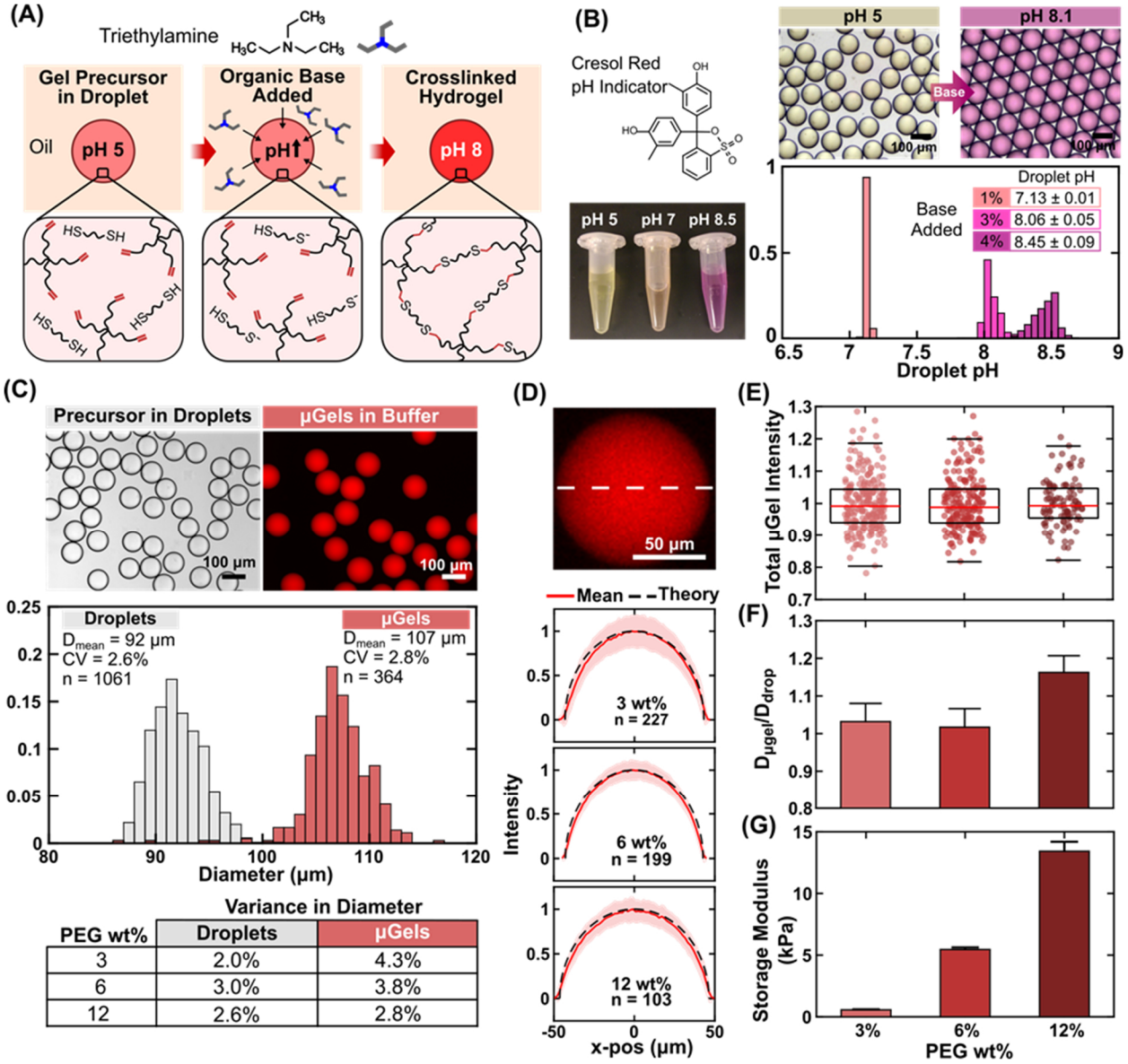


**Figure 3-3 Characterization of microgel crosslinking via pH modulation.** (A) Schematic of crosslinking methodology. Droplets are formed from hydrogel precursor and crosslinker solution at a non-reactive pH. Triethylamine is added through the oil phase and partitions into the aqueous phase of the droplets to increase the pH and deprotonate the thiol groups on the crosslinkers. Deprotonated thiols react with vinyl sulfone groups on the multi-arm PEG. (B) pH change in droplets is measured using a pH indicator dye (Cresol Red). pH is modulated by adjusting concentration of organic base and is shown to be highly uniform among the droplet population. Amount of base added is relative to aqueous volume. (C) The crosslinking process has minimal effects on droplet stability, resulting in high uniformity of the µgels. (D, E) Crosslinking density of swollen µgels is measured indirectly by fluorophores conjugated to the gel matrix. Intensity line profiles are uniform and compare directly to theoretical intensity profiles for a perfectly uniform spherical gel particle. Total fluorescence intensity among µgels is uniform, with variations comparable to volume variation. (F) µgels swell minimally after transferring from oil to water phase. (G) Over an order of magnitude range of gel stiffnesses is achieved by changing PEG precursor concentration.

### 3.2.3. *Effect of Scaffold Stiffness on Cell Proliferation In Vitro*

Understanding effects of scaffold stiffness on proliferation in a 3D environment has implications in enhancing wound regeneration or in promoting selective cell growth using only material physical properties (as opposed to added growth factors or cells which can require more time and cost to translate to clinical use). To demonstrate the flexibility of our platform in creating microporous 3D environments, μgel building blocks were fabricated over a range of physiologically relevant tissue stiffnesses while maintaining uniform presentation of integrin binding sites. Specifically, μgels with storage moduli of 0.5, 5.5, and 13.5 kPa were produced by increasing the concentration of PEG precursor, while maintaining the same RGD ligand density. Due to the high crosslinking density of the 8-arm PEG-VS the swelling of the μgels after transfer from the oil phase was minimal, only noticeable for relatively high concentrations (**Figure 3-3F**). Because of this we can maintain final μgel sizes largely independent of stiffness using the same device. This capability allows for more practical control of the final microporous environment both in terms of structure and mechanics (**Figure 3-3F,G**).

To study the effects of stiffness on cell proliferation and network formation *in* vitro, we cultured human dermal fibroblasts (HDF) in our MAP scaffolds with three different stiffnesses. Cells were dispersed into a concentrated μgel slurry and injected into a PDMS mold where the μgels covalently link together via an enzymatic reaction to create an interconnected microporous scaffold with cells occupying the interstitial spaces between μgels. After 3 days we observed higher relative cell densities within the stiffer microporous scaffold conditions (5.5, 13.5 kPa) compared to the soft microporous (0.5 kPa) and nanoporous conditions **(Figure 3-4)**. For the nanoporous gel scaffold cells must first break down the hydrogel environment to spread and grow, unlike the microporous conditions where there is pre-defined interconnected microporous

space which allows cells to spread and grow immediately, leading to faster proliferation. In addition, the connected microporous scaffolds allow for rapid formation of 3D cellular networks as shown by actin staining (**Figure 3-4**). Increased cell spreading and network formation of HDFs was observed for increasing gel stiffnesses with the MAP scaffolds, with less observed for the nanoporous condition. This corroborates the findings of previous work by Xin et al. which reported increased activation of mechanosensing pathways and mesenchymal stem cell proliferation in stiff microporous gels.[81]

Using MAP scaffolds the stiffness of the matrix is decoupled from the microporosity of the hydrogel scaffold allowing for cells to maintain mobility while probing their response to different stiffness environments in 3D. Notably, it is not possible to effectively explore cell growth behavior in bulk 3D scaffolds with high stiffness. For bulk hydrogel matrices, cells have limited motility and space within the higher stiffness gels which prevents spreading and growth.[111] In other microporous scaffold approaches, the hydrogel matrices must be formed prior to cell seeding, making it difficult to study cell growth behavior decoupled from cell migration.[112,113] In our work cells can be mixed into the μgel slurry prior to scaffold formation, ensuring a homogenous composition of cells such that effects of migration on cell growth are decoupled.

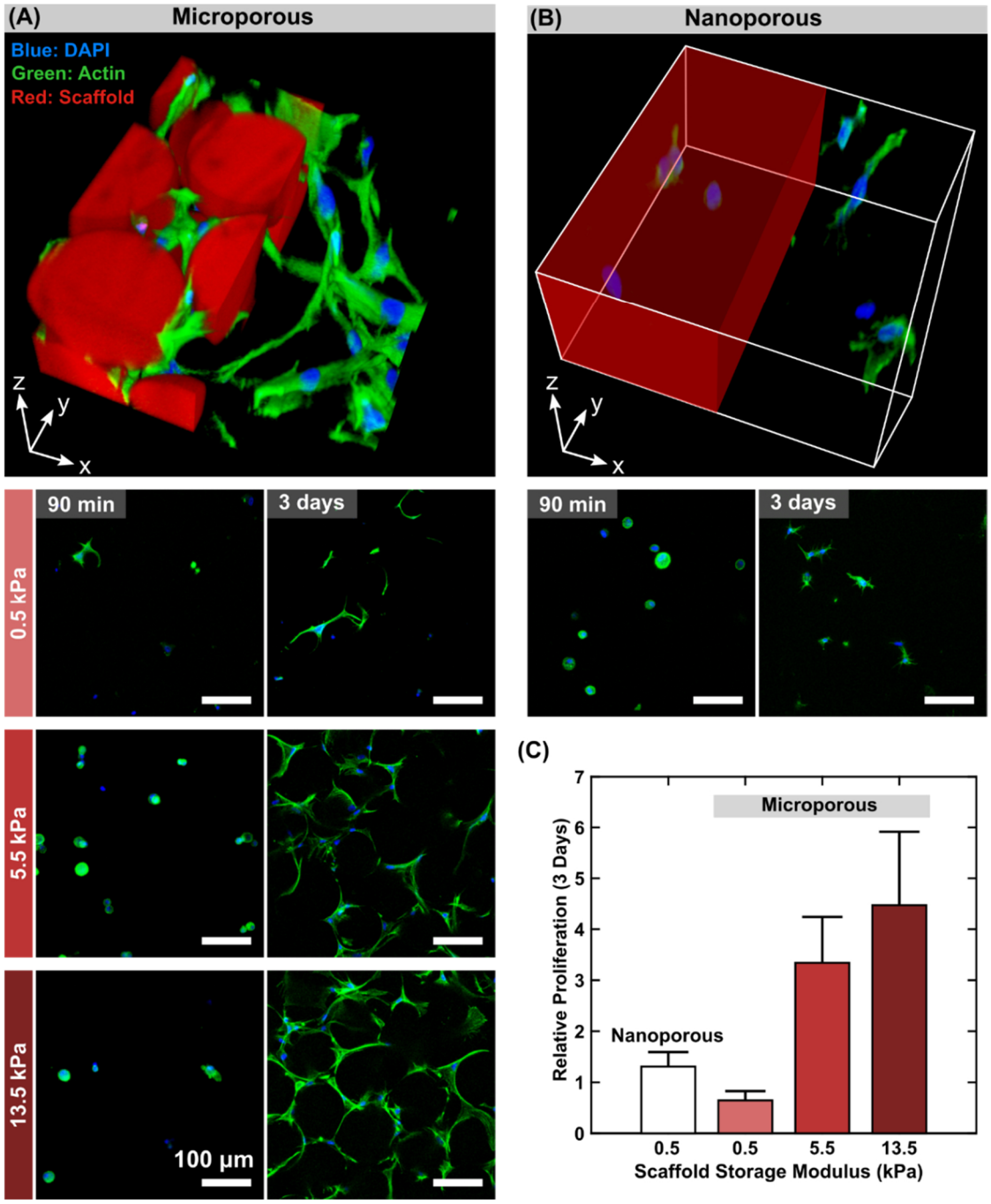


**Figure 3-4 Increased scaffold stiffness enhances cell proliferation and network formation *in vitro*.** (A) Microporous environment facilitates cell spreading as shown by filamentous actin staining. A stiffer microenvironment shows increased cell spreading and faster formation of connected 3D cellular networks. (B) In the nanoporous scaffolds, cells show a more spherical morphology and limited connection between cells. (C) Relative proliferation as determined by cell density at day 3 normalized by cell density at day 0. Cell proliferation was measured to be highest for the stiffest microporous condition. Limited proliferation was shown for both the nanoporous condition and the soft microporous condition. 3D confocal stack size is 258 x 258 x 150 µm. Condition for 3D microporous image is 13.5 kPa. For the nanoporous 3D image, the shown scaffold was overlaid in post for visual demonstration.

### 3.2.4. *Formation of Modular Mechanically Heterogenous Scaffolds*

Leveraging the ability to fabricate highly uniform µgels with a large range of material stiffnesses at reasonable throughputs, we also explore formation of mechanically variant microporous tissue scaffolds with large gradients in stiffness. Traditionally, formation of heterogenous scaffolds is limited to multi-material printing [114,115], or use of UV dosage/patterning to adjust scaffold mechanical properties.[116–118] A unique feature of using µgel building blocks to assemble microporous scaffolds is the ability to construct spatially variant environments *in situ*. Previous work has utilized this to fabricate scaffolds with spatial variation in gel degradability [84], and fluorescent markers [119]. Using our platform, we are able to extend this to variation/gradations in stiffness by forming cell-laden scaffolds composed of both stiff (13.5 kPa) and soft (0.5 kPa) µgel building blocks (**Figure 3-5**). By mixing different ratios of µgel components we are able to create 3D granular structures with subregions of distinct stiffnesses, as shown by confocal microscopy (**Figure 3-5C, Figure C-9**). Further, using sequential loading of a pipette we demonstrate the formation of layered scaffolds with a distinct interface between the two regions **(Figure 3-5B, Figure C-9)**. For this extreme case, a 10-micrometer cell bridging between two of these neighboring regions would experience a gradient in stiffness of approximately 1 kPa/µm.

Mechanically heterogeneous scaffolds led to region-specific responses for associated cells. HDFs were seeded into µgel slurries prior to scaffold formation and confocal imaging was performed on samples following fixation after 12 hours of incubation. Confocal imaging revealed preferred adhesion of cells to the stiffer µgels as well as increased spreading and actin formation in those regions. In this study we only looked at a simple binary model, however,

more complex systems can easily be constructed by incorporating additional gel types and by conjugating different densities of binding motifs such as RGD.

The ability to create gradations in stiffness at the microscale could provide benefits for healing of tissues that have distinct native tissue mechanical properties, or to create mechanical gradients to drive cell migration.[120–122] Further, spatial variation in mechanical properties could be used to direct multiple stem cell fates within a localized environment without the need for soluble cues, [123] or to create more complex microenvironments to study cancer initiation and progression both *in vitro* and *in vivo*.[124,125]

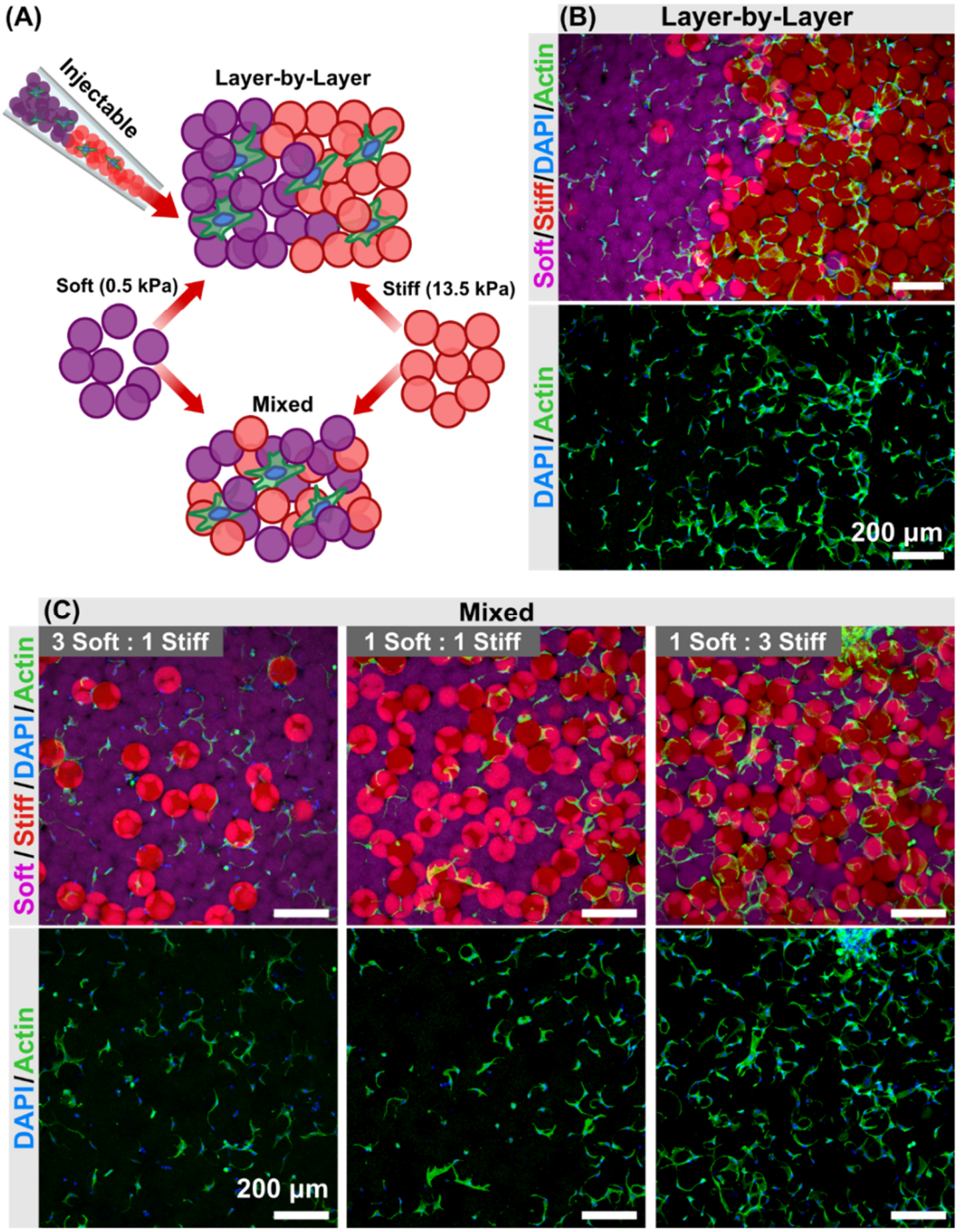


**Figure 3-5 *In situ* formation of cell laden mechanically heterogeneous scaffolds from modular building blocks.** (A) Schematic showing various schemes of cell-laden heterogeneous scaffolds. We demonstrate both the formation of (B) layer-by-layer scaffolds as well as (C) mixed granular scaffolds. Cell location and adhesion was examined using confocal microscopy. In general, we observe preferential adhesion of the fibroblasts around the stiff gel regions as well as increased spreading and actin formation at 12 hours.

## 3.3. **Conclusion**

We demonstrate a unique approach to fabricate highly uniform microgel building blocks in a continuous scalable high-throughput manner, enabling formation of highly modular microporous environments for cell and tissue growth (**Figure 3-1**). This approach has a host of advantages compared to typical microparticle fabrication approaches. Namely, the flow invariant nature of step emulsification device allows for straightforward scaling, and simplifies the adoption of less expensive pressure-based pump systems. Using proton acceptors dissolved in the oil phase to initiate crosslinking we ensure uniform physicochemical properties among microgel particles. Further, this approach is simple to implement, not requiring complex fabrication or UV setups, and is easily adapted to large scale systems. This ease of scalability is fundamental in realizing translation of microfluidic material fabrication from a niche research tool to an industrial scale production platform.

Due to the increased robustness of the gelation mechanism and increased throughput, we are able to produce monodisperse μgels over a large range of stiffnesses with relative ease compared to previous work. We demonstrate enhanced proliferation and spreading of HDFs in higher stiffness microporous environments. Stiffer or more highly cross-linked microgel building blocks can also enable longer degradation rates or drug release profiles to tune long-term regeneration or cell niche formation. Taking advantage of the modularity of this approach, we demonstrate, for the first time, the formation of cell-laden microporous scaffolds with heterogeneous mechanical properties across an order of magnitude *in situ*. This unique approach could be used to create stiffness gradations *in vivo* to enhance stem cell recruitment for tissue repair or to create spatially arranged tissue micro environments that can be used in the regeneration of complex tissues or to study cancer initiation and progression. Further, these modular microparticle "inks"

are compatible with 3D bioprinting technologies enabling formation of more complex macroscale structures with intrinsic microscale porosity that can enhance nutrient and waste transport and lead to immediate cell infiltration.[126–129]

## 3.4. **Materials and Methods**

**Device Fabrication.** Step emulsification devices were fabricated using soft lithography. Master molds were fabricated on mechanical grade silicon wafers (University wafer) using a two-layer photolithography process with KMPR 1010 and 1050 (MicroChem Corp). The first and second layers defining the nozzle channel height and the inlet/outlet reservoir region channel height, respectively. A nozzle channel height of 25 µm and 11 µm was used to produce ~50 µm and ~90 µm droplets respectively. Reservoir height for each device was ~150 µm. Precise device geometries are reported in the supporting information. Devices were molded from the masters using poly(dimethyl)siloxane (PDMS) Sylgard 184 kit (Dow Corning). The base and crosslinker were mixed at a 10:1 mass ratio, poured over the mold, degassed, and cured at 65°C overnight. The PDMS devices and glass microscope slides (VWR) were then activated via air plasma (Plasma Cleaner, Harrick Plasma) and bonded together. The bonded devices were then treated with Aquapel™ for 1 min and rinsed with Novec 7500 oil (3M) to render the channels fluorophilic. After modification devices were placed in an oven at 70°C for 1 hour to evaporate residual oil in the channels. For throughput comparison experiments, a flow focusing device with a channel height of 70 µm and junction width of 65 µm was fabricated using the same general procedure.

**Device Characterization Experiments.** For all droplet characterization experiments a dispersed phase comprised of various concentrations of 8-arm PEG-VS (JenKem) in 0.15 M triethanolamine buffer (pH 5, Sigma) and continuous phase composed of Novec 7500 oil (3M) and 0.5 wt% PicoSurf (Sphere Fluidics). Solutions were injected into a step emulsification device at defined flow rates using syringe pumps (Harvard Apparatus PHD 2000). Unless otherwise noted, the continuous phase was injected at twice the flow rate of the dispersed phase. A high-speed camera (Phantom V2010) was used to capture droplet formation dynamics at 2000 fps. For droplet size characterization, droplets were collected in a second reservoir chamber and brightfield images were taken using an inverted microsope (Nikon, Eclipse Ti-S fluorescence microscope). A custom MATLAB algorithm was used to analyze droplet size distribution. For all measurements >300 droplets were measured. For the throughput demonstration we imaged an aqueous phase composed of 15 wt% PEG 6000 (Sigma) with 100 μM rhodamine isothiocyanate dextran (10 kDa, Sigma) for visualization.

**pH Modulation Characterization.** A colorimetric pH indicator dye (Cresol Red, Sigma) was used to characterize pH change in the droplets. Droplets were formed from a dispersed phase comprised of 0.5 mg/mL indicator dye in 0.3 M triethanolamine buffer (pH 5). Various amounts of Novec 7500 oil with 3% vol/vol triethylamine (Sigma) were introduced into the droplet suspensions to increase the pH of the aqueous phase. Triethylamine was chosen due to its miscibility in both the oil and water phases, however, other bases that fulfill this criteria could be used. Reported triethylamine wt% refers to the amount in proportion to the aqueous volume. Droplets were imaged using a color camera (Nikon, DS-Fi3) and corresponding pH was

converted from mean droplet hue values using a calibration curve and custom MATLAB algorithm (**Figure C-7**).

**µGel Fabrication.** The precursor solutions consisted of 8 arm PEG-VS was dissolved in 0.3 M triethanolamine (pH 5) at 2X concentration. For cell experiments 500 µM K-peptide (Ac-FKGGERCG-$NH_2$, Genscript), 500 µM Q-peptide (Ac-NQEQVSPLGGERCG-$NH_2$, Genscript), and 1 mM RGD (Ac-RGDSPGERCG-$NH_2$, Genscript) was added to the precursor solution. For all conditions the crosslinker concentration was calculated such that 0.8 of the vinyl sulfone groups are occupied. DTT crosslinker was dissolved in DI water at 2X concentration needed for 0.8 crosslinking ratio and was pre-reacted with 10 µM Alexa Fluor 488 maleimide (Life Technologies). Precursor and crosslinker solutions were then added together at equal volume and mixed by vortexing. The combined solution was injected at defined flowrates along with the continuous phase to generate water in oil emulsions. The outlet tubing (PTFE, Zeus) was connected to a Y junction (IDEX Health & Science) where a second continuous phase containing organic base was introduced to increase the pH of the gel precursor droplets and initiate gelation. Oil containing the organic base was injected using a Hamilton™ gas-tight syringe. The residence time in the tubing between introduction of the organic base and the collection tube was approximately 4 min.

After incubation overnight at room temperature, crosslinked µgels were extracted from the oil using a series of washing steps. Excess oil was removed by pipetting and a solution of 20 wt% perfluorooctanol (Sigma) in Novec 7500 oil was added (approximately equal volume to remaining solution) to break down the emulsions. HEPES buffer was added to swell and disperse the µgels. The remaining Novec 7500 oil was removed by addition of hexane (Sigma) to lower

the density of the oil, and μgels were pelleted using a table top centrifuge at 2000 x g for 5 min. Supernatant was removed and the hexane wash was repeated 3X. For non-cell experiments μgels were washed multiple times with HEPES buffer until residual hexane was removed. For cell experiments, μgels were sterilized by washing 3X with 70% Ethanol in DI (MilliQ) followed by incubation at 4°C overnight. Gels were then washed 5X with sterile HEPES buffer (pH 7.4 + 10 mM $CaCl_2$) prior to use.

**Mechanical Characterization.** Rheological measurements were performed on bulk gel samples using a TA Instruments DHR-2 rheometer. A 2X concentration solution of PEG was dissolved in 0.3 M TEOA and combined with equal volume of 2X DTT crosslinker dissolved in DI water. The mixture was vortexed and pipetted between two silane treated glass slides with a 1 mm Teflon spacer and incubated at room temperature overnight. Samples were removed and incubated in HEPES buffer for at least 2 hours prior to measurements. A frequency sweep of 0.1 to 10 Hz was performed using an 8 mm disk and storage modulus was calculated from the average of the linear range.

**Cell Culture.** Human dermal fibroblasts (HDF, ATCC® PCS-201-012™) were maintained according to manufacturer's specifications. Fibroblast basal medium and fibroblast growth kit-low serum were purchased from ATCC. Cell media was supplemented with 0.1% penicillin/streptomycin (Invitrogen). Cells were cultured at 37°C and 5% $CO_2$.

**In Vitro Culture in Microporous Scaffolds.** A suspension of μgels was incubated in a solution of HEPES pH 7.4 + 10 mM $CaCl_2$ + 5 U/ml FXIII (Abcam) overnight at 4°C. Prior to annealing

excess solution was removed and µgels were spiked with thrombin (Abcam) to a final concentration of 2 U/ml, and concentrated HDF suspensions to a final concentration of 1000 cells/µl. The µgel and cell slurry was mixed and then injected into custom PDMS wells with a positive displacement pipette (MICROMAN, Gilson, Inc.) and incubated at 37°C for 90 min to form annealed microporous scaffolds. Cell samples were fixed at day 0 and day 3 with 4% PFA at 4°C overnight. Samples were permeabilized with 0.1% solution of Triton X-100 (Sigma) for 30 min, and then washed with PBS. Fixed samples were stained with Alexa Fluor 647 phalloidin (Invitrogen) for 3 hours at room temperature and washed with PBS. The samples were then counterstained with 2 µg/ml DAPI solution in PBS for 1 hour at room temperature.

**In Vitro Culture in Nanoporous Scaffolds.** PEG-VS scaffolds (3 wt%) were formed with the same concentration of reagents as described above, with the exception that an MMP degradable crosslinker (Ac-GCRDGPQGIWGQDRCG-$NH_2$, Genscript) was used in place of DTT. Briefly, 2X Precursor and 2X crosslinker solution were mixed, spiked with cells and incubated for 15 minutes at 37°C before being placed in appropriate media. Gels were fixed and stained following the same procedure as the microporous samples.

**In Vitro Proliferation Quantification.** Cell proliferation was assessed by counting the number of cell nuclei present in the scaffolds after 90 min and 3 days of culture *in vitro* as previously reported [80]. Briefly, 50 z slices at 3µm increments (150 µm total z height) were taken with a 10X objective. To count number of cells in the image stack every 10 slices were compressed into a maximum intensity projection image and counted using a custom MATLAB script. For each

condition a minimum of 5 samples were analyzed. All confocal images were taken using a Leica inverted SP5 confocal microscope.

**Cell-Laden Heterogeneous Scaffold Formation.** Two populations of 100 µm gels were fabricated as previously described: (1) Stiff µgels (13.5 kPa) conjugated with Alexa Fluor 488 maleimide and (2) soft µgels (0.5 kPa) conjugated with Alexa Fluor 568 maleimide. Gels were prepared for annealing as previously described. For layer-by-layer scaffold formation µgel slurries were loaded with a concentrated suspension of HDFs and mixed such that the final concentration was 2000 cells/µL. The two respective µgel types were sequentially loaded into a positive displacement pipette and injected into a PDMS well. After annealing, samples were incubated and then fixed at 12 hours. For the mixed scaffolds, samples were prepared by first mixing appropriate volumes of the different gel types at the desired ratio and mixed via pipetting. Sample were then spiked with a concentrated cell suspension and mixed again to achieve a final concentration of 2000 cells/µL. The samples were then injected into the PDMS molds, cultured, and then fixed at 12 hours.

# Chapter 4. Scalable fabrication of 3D structured microparticles using induced phase separation

In the previous chapter we utilized a parallelized microfluidic droplet generator to manufacture spherical biocompatible hydrogel microparticles in a scalable manner. In this chapter I will briefly discuss our preliminary results to extend this approach to fabricate microparticles with 3D morphology. The objective of this chapter is not to provide a comprehensive study of the approach, but to motivate the need and show proof-of-concept demonstration.

## 4.1. Introduction

Shaped microparticles have been explored for numerous industrial uses, such as in biotechnology, medical devices, or in life science research. For example, spherical hydrogel microparticles can be assembled in vitro or in vivo to create porous scaffolds which allow rapid cellular ingrowth or act as a depot for delivering cells or drugs.[78,80,130–132] Modulation of the shape of the particles to include completely enclosed voids or cavities opening to the surrounding environment can increase the effective space in assembled scaffolds, yielding improved cellular infiltration. Spherical particles with open cavities (e.g. particles with a crescent shaped cross-section) can also act as carriers for cell attachment, protecting cells from shear stress in the surrounding fluid.[31] Similar crescent shape particles can also be used to isolate cells and scaffold the formation of uniform aqueous droplets in oil, or dropicles/particle-drops.[31] These cell-carrier particles can also be used to capture biomolecules released from attached cells, bind fluorescent molecules or magnetic beads to the captured biomolecules and analyzed using microscopy, flow cytometry, or magnetic activated cell sorting.

Previous approaches to manufacture shaped microparticles rely on complex processes and have limited throughput. A number of approaches have been proposed to manufacture microscale materials with defined structures. Photolithography and two-photon polymerization have been utilized to generate asymmetric microparticles.[133,134] Microfluidic approaches such as stop-flow lithography, continuous flow lithography, and maskless lithography approaches have been utilized to create 2D extruded shapes.[135–137] Slightly more advanced approaches have utilized fluid sculpting to add another degree of geometric freedom in stop flow lithography.[138–142] Despite the complexity of shapes that can be fabricated with these approaches, fabrication throughputs are typically limited to 10,000 - 100,000 particles per hour. Further, many of these approaches depend on very costly equipment. These two factors create a significant barrier for the use of these materials in downstream research and industrial applications.

Aqueous two-phase systems (ATPS), including a pre-polymer precursor, combined with flow focusing microfluidic devices have been used previously to manufacture crescent-shaped microparticles.[31,70,71] Flow focusing devices are used since co-flowing streams of the two aqueous phase precursors meeting at the droplet generation point allows quantities proportional to the flow rates of the two phases into each droplet generated. Mixing of the aqueous phases prior to introduction leads to local domains of the separate phases forming in the device prior to entering the droplet generator leading to non-uniform sizes for the crescent shaped void in the particles formed, including particles that may not contain cavities at all. Notably, a flow focusing design which has multiple co-flowing streams meeting prior to droplet generation is difficult to operate and balance all of the specific flow rates across numerous input channels.

By starting with two precursor phases which are miscible, creating a homogenous solution, but then become immiscible upon a physical or chemical stimulus we overcome the

challenges with scalable production in previous approaches. Induced phase-separation of droplets following microfluidic emulsification is a key to high-throughput production of monodisperse multi-phased droplets (and particles). Previously, a parallelized step emulsification device, which is compatible with a homogeneous solution, enabled scalable high-throughput generation of monodisperse homogeneous spherical droplets.[143] By using triggered phase separation after droplet formation in a parallelized microfluidic step emulsification device we can create uniform 3D-structured particles with cavities or completely enclosed voids.

## 4.2. **Methods and Results**

### 4.2.1. *Temperature induced phase separation and particle fabrication*

In this section I discuss one approach to fabricate crescent shaped particles with a parallelized step emulsification device by exploiting the temperature sensitivity of gelatin. In our previous work dextran was used as the second polymer phase of our aqueous two-phase system for generating crescent shaped particles (**Figure A-2**).[31] In this study we replaced dextran with gelatin as the resulting ATPS system was more sensitive to temperature fluctuations. For example, previous studies showed that in a critical concentration range, lowering temperature can induce phase separation in a PEG-Gelatin ATPS system.[144] Here we show an example workflow where we exploit this sensitivity to induce phase separation after droplet generation and crosslink the resulting two-phased droplets to fabricate crescent particles.

A solution of 7.5% w/w PEGDA 1500 Da (Sigma), 15% w/w cold water fish gelatin (Sigma) and 1 % w/w LAP (Lithium phenyl-2,4,6-trimethylbenzoylphosphinate, Sigma) in Phosphate Buffered Saline (PBS, pH7.2) was prepared. Next, the solution was injected into a parallelized step-emulsification device at a rate of 10 µL/min along with an oil phase comprising

Novec 7500 (3M) and 0.25% w/w PicoSurf (Sphere Fluidics) at a rate of 42 µL/min to generate monodisperse water and oil droplets. The microfluidic device was operated at room temperature to maintain a mixed state for the precursor materials. Droplets were collected and incubated in a 4 °C refrigerator for 1 hour to induce phase separation of PEG and gelatin polymers (**Figure 4-1**). After phase separation, the PEG phase was crosslinked with UV light. Crosslinked particles were collected and oil and gelatin were removed using a series of washing steps. Briefly, excess oil was removed by pipetting and a layer of PBS was added on top of the remaining emulsions. A solution of 20% v/v perfluorooctanol (PFO, Sigma) in Novec 7500 was then added to destabilize the emulsions and transfer particles to the PBS phase. Excess oil was removed and samples were washed 2X with Novec 7500 to remove remaining surfactant. Novec 7500 was removed by pipetting and residual oil was removed by washing 2-3X with hexane (Sigma). Samples were then washed 3X with PBS to remove gelatin from the system. The resulting particle shapes were similar to those used for cell secretion assays, containing an exposed inner cavity that can be used to load cells.

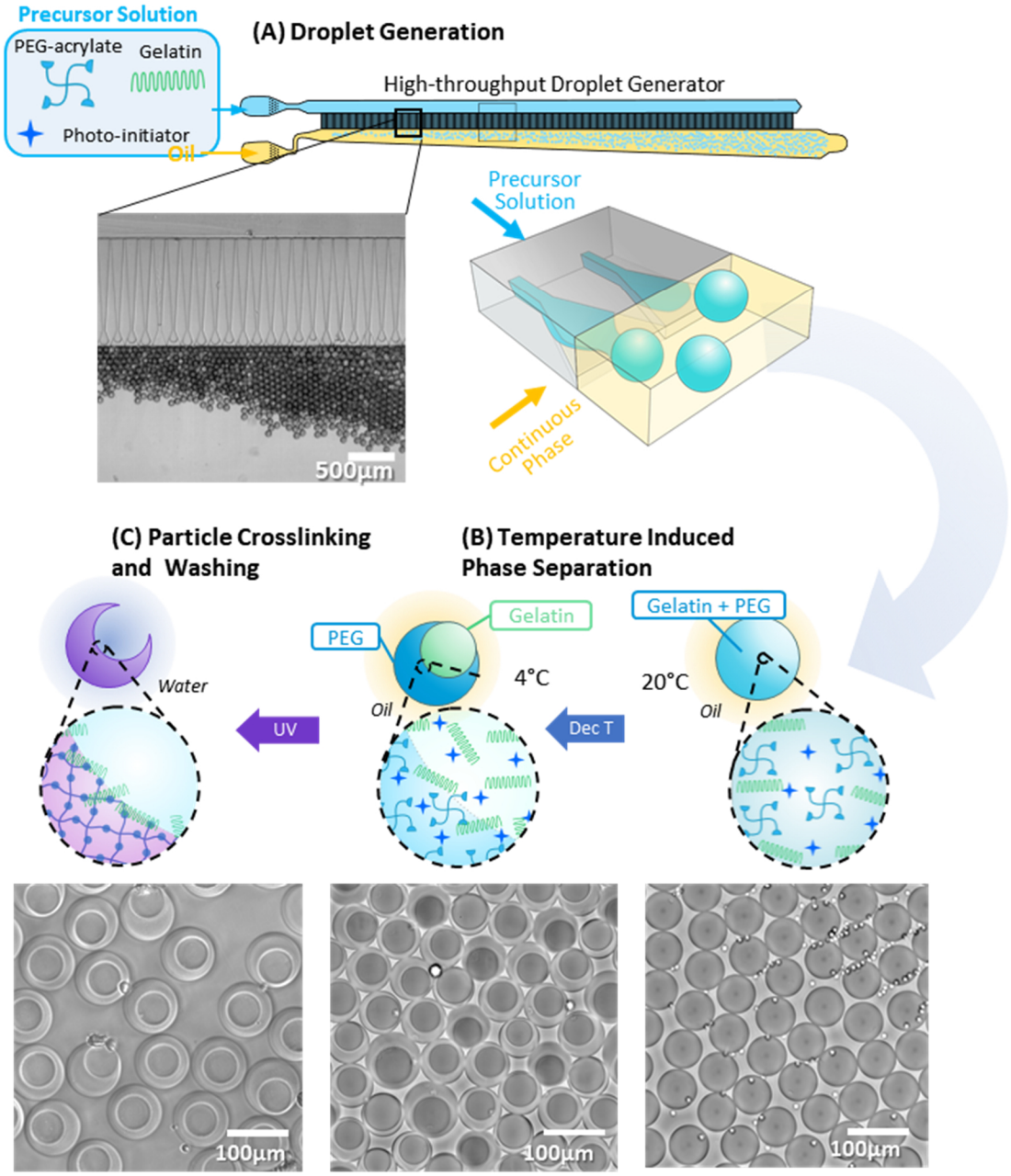


**Figure 4-1. PEG-Gelatin ATPS approach to generate structured microparticles.** Photo-reactive PEG, gelatin, and photoinitiator are premixed and injected into a high-throughput droplet step-emulsification device. (B) The resulting single-phase droplets are then cooled down to 4°C to induce phase separation between the PEG and gelatin phases. (C) After phase separation the two-phase droplets are then exposed with UV light to crosslink the PEG phase and the resulting particles are then recovered from oil and washed.

### 4.2.2. *Crosslinking Induced Phase-Separation and Particle Fabrication*

In this section I will discuss another approach to fabricate structured microparticles with the step-emulsification by exploiting crosslinking induced phase-separation. ATPS systems can be sensitive to a number of different properties including temperature, pH, salinity, molecular weight, and polymer concentration.[145,146] Here we exploit the known fact that the concentration at which phase separation occurs can be very sensitive to the molecular weight of the PEG. In general, as the molecular weight of PEG increases the concentration at which phase separation occurs decreases. Here we show that by partially crosslinking the PEG component of an ATPS system after droplet generation, the effective increase in apparent molecular weight can induce phase separation. Once phase separation occurs crosslinking can be accelerated to preserve the resulting morphology and create 3D structured particles.

Here we demonstrate crosslinking induced 3D particle fabrication using a pH sensitive PEG polymer precursor along with dextran (**Figure 4-2**). 2% w/w 8-arm PEG vinylsulfone, 3.2 mM dithiotreitol, and 6.6% w/w 40 kDa dextran are mixed together in 0.3 M thriethanolamine buffer at slightly acidic pH (pH 5). At this condition precursors were found to be sufficiently miscible. The precursor is then emulsified into Novec™ 7500 fluorinated oil with 0.5% v/v Pico-Surf™ using the step-emulsification device described before. Additional Novec™ 7500 fluorinated oil containing 1% triethylamine by volume is then added to the oil phase of the emulsion at equal volume to the precursor phase to increase the pH to ~7 to initiate crosslinking. It was found that after 2 minutes the PEG and dextran undergo sufficient phase separation. Additional Novec™ 7500 fluorinated oil containing 2% triethylamine by volume was then added to the oil phase of the emulsion at equal volume to the precursor phase to increase the pH again to ~8.1 to accelerate the crosslinking and preserve the particle morphology. After incubating at

37°C the particles were then recovered from the oil phase and washed. For this particular set of conditions, the final particles were observed to have a shallow-bowl like morphology (**Figure 4-2**).

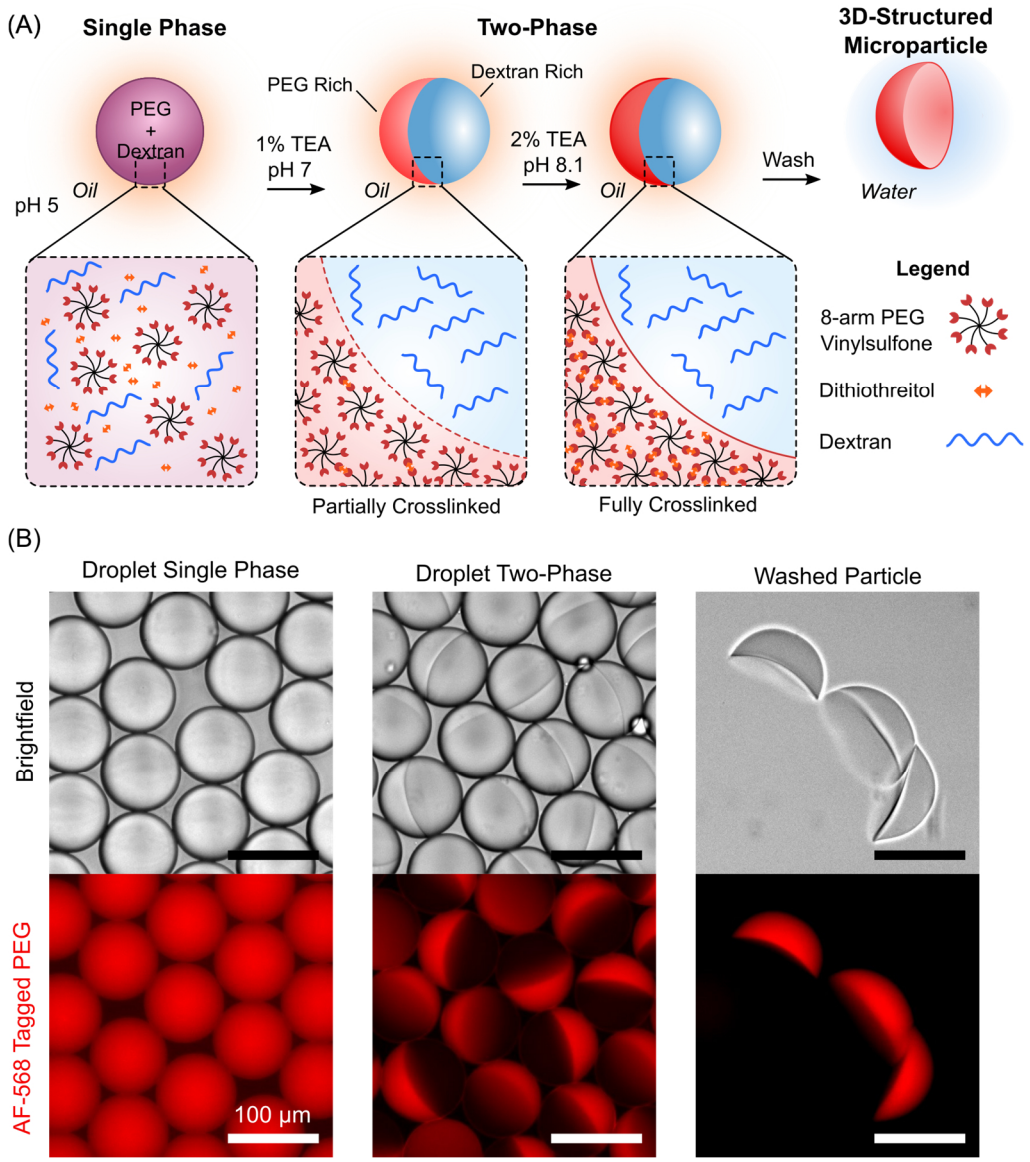


**Figure 4-2. Fabrication of structured microparticles using crosslinking induced phase separation.** (A) pH reactive PEG polymer, dithiol crosslinker, and dextran are mixed together in an acidic buffer (pH 5) below the binodal point and droplets are formed. Organic base is added through the oil phase to increase the pH to 7 and partially crosslink the PEG to effectively increase the molecular weight and induce phase separation. Additional organic base is added to increase the reaction rate and crosslink particles fully. Particles are then recovered by washing away the oil. (B) Example experiments showing fabrication of bowl shaped microparticles using this approach. Fluorescent dye is conjugated to the PEG to help visualize PEG and dextran separation.

## 4.3. **Discussion**

In this chapter we demonstrate two proof-of-concept workflows to fabricate 3D-structured microparticles using induced phase separation. The first approach exploited the temperature sensitivity of gelatin to induce phase separation and fabricate crescent shaped particles similar to those used in Chapter 2. In the second approach we show that partial crosslinking of PEG can also be exploited to induce phase separation and successfully fabricate particles with a shallow-bowl or Janus morphology.

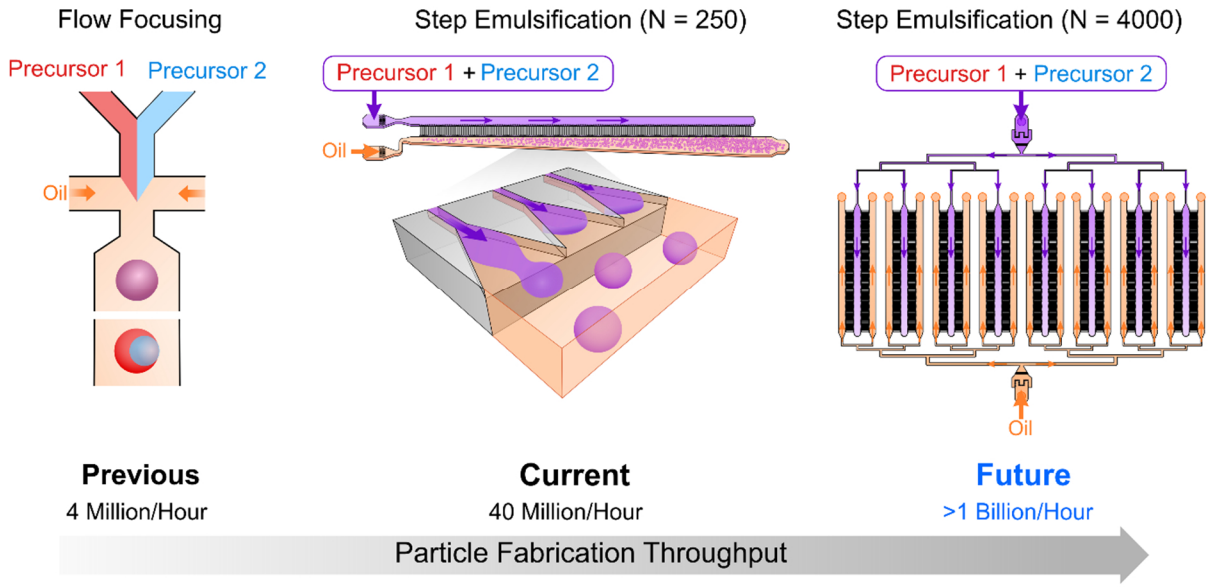


**Figure 4-3. Comparison of approaches to produce structured microparticles.** The original flow focusing approach used to fabricate 3D structured particles achieved throughputs of ~4 million/hour. By combining induced phase separation and a high-throughput step emulsification device this throughput was increased to 40 million/hour in this preliminary work. Due to the scalability of this method, it is possible to scale this significantly to achieve rates > 1 billion/hr in the future.

These results are a promising next step in scaling the production of more complex shaped microparticles. Using our previous flow-focusing approach we achieved throughputs of ~ $4 \times 10^6$ particles/hr. Here we are able to increase our particle manufacturing throughput by approximately an order of magnitude using a 250-channel step-emulsification device, generating ~$4 \times 10^7$ particles/hr (**Figure 4-3**). In the future larger scaled devices can be used to improve this

even more, potentially generating particles at rates > $10^9$ particles/ hr. In later work we will further explore these workflows to generate particles with more morphologies and demonstrate the functionality of the resulting particles.

## References


1. Hathout, Y. Approaches to the study of the cell secretome. *Expert Rev. Proteomics* **4**, 239–248 (2007).
2. Uhlén, M. *et al.* Tissue-based map of the human proteome. *Science (80-. ).* (2015) doi:10.1126/science.1260419.
3. Bennett, N. T. & Schultz, G. S. Growth factors and wound healing: Biochemical properties of growth factors and their receptors. *The American Journal of Surgery* vol. 165 728–737 (1993).
4. Alexander, W. S. & Hilton, D. J. THE ROLE OF SUPPRESSORS OF CYTOKINE SIGNALING (SOCS) PROTEINS IN REGULATION OF THE IMMUNE RESPONSE. *Annu. Rev. Immunol* **22**, 503–532 (2004).
5. Arai, K. *et al.* Cytokines: Coordinators of immune and inflammatory responses. *Annual Review of Biochemistry* vol. 59 783–836 (1990).
6. Birkedal-Hansen, H. Proteolytic remodeling of extracellular matrix. *Curr. Opin. Cell Biol.* **7**, 728–735 (1995).
7. Delves, P. J. & Roitt, I. M. The Immune System. *N. Engl. J. Med.* **343**, 37–49 (2000).
8. Scott, A. M., Wolchok, J. D. & Old, L. J. Antibody therapy of cancer. *Nature Reviews Cancer* vol. 12 278–287 (2012).
9. Chaput, N. & Théry, C. Exosomes: Immune properties and potential clinical implementations. *Seminars in Immunopathology* vol. 33 419–440 (2011).
10. Greening, D. W., Gopal, S. K., Xu, R., Simpson, R. J. & Chen, W. Exosomes and their roles in immune regulation and cancer. *Seminars in Cell and Developmental Biology* vol. 40 72–81 (2015).

11. Abdelsamed, H. A. *et al.* Beta cell-specific CD8+ T cells maintain stem cell memory-associated epigenetic programs during type 1 diabetes. *Nat. Immunol.* **21**, 578–587 (2020).

12. Fraietta, J. A. *et al.* Disruption of TET2 promotes the therapeutic efficacy of CD19-targeted T cells. *Nature* **558**, 307–312 (2018).

13. Rossi, J. *et al.* Preinfusion polyfunctional anti-CD19 chimeric antigen receptor T cells are associated with clinical outcomes in NHL. *Blood* **132**, 804–814 (2018).

14. Han, Q. *et al.* Polyfunctional responses by human T cells result from sequential release of cytokines. *Proc. Natl. Acad. Sci. U. S. A.* **109**, 1607–1612 (2012).

15. Di Carlo, D., Tse, H. T. K. & Gossett, D. R. Introduction: Why analyze single cells? *Methods Mol. Biol.* **853**, 1–10 (2012).

16. Di Carlo, D. Technologies for the Directed Evolution of Cell Therapies. *SLAS Technol. Transl. Life Sci. Innov.* **24**, 359–372 (2019).

17. Unger, M. A., Chou, H. P., Thorsen, T., Scherer, A. & Quake, S. R. Monolithic microfabricated valves and pumps by multilayer soft lithography. *Science (80-. ).* **288**, 113–116 (2000).

18. Junkin, M. *et al.* High-Content Quantification of Single-Cell Immune Dynamics. *Cell Rep.* **15**, 411–422 (2016).

19. Love, J. C., Ronan, J. L., Grotenbreg, G. M., van der Veen, A. G. & Ploegh, H. L. A microengraving method for rapid selection of single cells producing antigen-specific antibodies. *Nat. Biotechnol.* **24**, 703–707 (2006).

20. Ma, C. *et al.* A clinical microchip for evaluation of single immune cells reveals high functional heterogeneity in phenotypically similar T cells. *Nat. Med.* (2011) doi:10.1038/nm.2375.

21. Varadarajan, N. *et al.* Rapid, efficient functional characterization and recovery of HIV-specific human CD8 + T cells using microengraving. *Proc. Natl. Acad. Sci. U. S. A.* **109**, 3885–3890 (2012).

22. Lu, Y. *et al.* High-throughput secretomic analysis of single cells to assess functional cellular heterogeneity. *Anal. Chem.* (2013) doi:10.1021/ac400082e.

23. Torres, A. J., Hill, A. S. & Love, J. C. Nanowell-based immunoassays for measuring single-cell secretion: Characterization of transport and surface binding. *Anal. Chem.* (2014) doi:10.1021/ac4030297.

24. Heath, J. R., Ribas, A. & Mischel, P. S. Single-cell analysis tools for drug discovery and development. *Nature Reviews Drug Discovery* vol. 15 204–216 (2016).

25. Le, K. *et al.* A novel mammalian cell line development platform utilizing nanofluidics and optoelectro positioning technology. *Biotechnol. Prog.* **34**, 1438–1446 (2018).

26. Winters, A. *et al.* Rapid single B cell antibody discovery using nanopens and structured light. *MAbs* **11**, 1025–1035 (2019).

27. Le, K. *et al.* Assuring Clonality on the Beacon Digital Cell Line Development Platform. *Biotechnol. J.* (2020) doi:10.1002/biot.201900247.

28. Anna, S. L., Bontoux, N. & Stone, H. A. Formation of dispersions using " flow focusing " in microchannels. *Cit. Appl. Phys. Lett.* **82**, (2003).

29. Mazutis, L. *et al.* Single-cell analysis and sorting using droplet-based microfluidics. *Nat. Protoc.* **8**, 870–891 (2013).

30. Konry, T., Dominguez-Villar, M., Baecher-Allan, C., Hafler, D. A. & Yarmush, M. L. Droplet-based microfluidic platforms for single T cell secretion analysis of IL-10 cytokine. *Biosens. Bioelectron.* **26**, 2707–2710 (2011).

31. de Rutte, J., Dimatteo, R., van Zee, M., Damoiseaux, R. & Di Carlo, D. Massively parallel encapsulation of single cells with structured microparticles and secretion-based flow sorting. *bioRxiv* 2020.03.09.984245 (2020) doi:10.1101/2020.03.09.984245.

32. Chokkalingam, V. *et al.* Probing cellular heterogeneity in cytokine-secreting immune cells using droplet-based microfluidics. *Lab Chip* **13**, 4740 (2013).

33. Eyer, K. *et al.* Single-cell deep phenotyping of IgG-secreting cells for high-resolution immune monitoring. *Nat. Biotechnol.* **35**, 977–982 (2017).

34. Gérard, A. *et al.* High-throughput single-cell activity-based screening and sequencing of antibodies using droplet microfluidics. *Nat. Biotechnol.* 1–7 (2020) doi:10.1038/s41587-020-0466-7.

35. Manz, R., Assenmacher, M., Pflüger, E., Miltenyi, S. & Radbruch, A. Analysis and sorting of live cells according to secreted molecules, relocated to a cell-surface affinity matrix. *Proc. Natl. Acad. Sci. U. S. A.* **92**, 1921–1925 (1995).

36. Assenmacher, M., Löhning, M. & Radbruch, A. Detection and Isolation of Cytokine Secreting Cells Using the Cytometric Cytokine Secretion Assay. *Curr. Protoc. Immunol.* **46**, (2001).

37. Borth, N., Zeyda, M. & Katinger, H. Efficient selection of high-producing subclones during gene amplification of recombinant Chinese hamster ovary cells by flow cytometry and cell sorting. *Biotechnol. Bioeng.* **71**, 266–273 (2000).

38. Dhar, M. *et al.* Functional profiling of circulating tumor cells with an integrated vortex capture and single-cell protease activity assay. *Proc. Natl. Acad. Sci. U. S. A.* **115**, 9986–9991 (2018).

39. Josephides, D. *et al.* Cyto-Mine: An Integrated, Picodroplet System for High-Throughput

Single-Cell Analysis, Sorting, Dispensing, and Monoclonality Assurance. *SLAS Technol. Transl. Life Sci. Innov.* **25**, 177–189 (2020).

40. Lu, Y. *et al.* Highly multiplexed profiling of single-cell effector functions reveals deep functional heterogeneity in response to pathogenic ligands. *Proc. Natl. Acad. Sci. U. S. A.* **112**, E607–E615 (2015).

41. Baret, J. C. *et al.* Fluorescence-activated droplet sorting (FADS): Efficient microfluidic cell sorting based on enzymatic activity. *Lab Chip* **9**, 1850–1858 (2009).

42. Dimatteo, R. & Di Carlo, D. Droplet-Enhanced On-Cell Encoding of Single Cell Secretory Function. in *23rd International Conference on Miniaturized Systems for Chemistry and Life Sciences, MicroTAS 2019* (2019).

43. Wimmers, F. *et al.* Single-cell analysis reveals that stochasticity and paracrine signaling control interferon-alpha production by plasmacytoid dendritic cells. *Nat. Commun.* **9**, (2018).

44. Shi, Q. *et al.* Single-cell proteomic chip for profiling intracellular signaling pathways in single tumor cells. doi:10.1073/pnas.1110865109/-/DCSupplemental.

45. Ahn, K. *et al.* Dielectrophoretic manipulation of drops for high-speed microfluidic sorting devices. *Appl. Phys. Lett.* **88**, 1–3 (2006).

46. Isozaki, A. *et al.* Sequentially addressable dielectrophoretic array for high-throughput sorting of large-volume biological compartments. *Sci. Adv.* **6**, eaba6712 (2020).

47. Mazutis, L. *et al.* Single-cell analysis and sorting using droplet-based microfluidics. *Nat. Protoc.* **8**, 870–91 (2013).

48. Love, J. C., Ronan, J. L., Grotenbreg, G. M., Van Der Veen, A. G. & Ploegh, H. L. A microengraving method for rapid selection of single cells producing antigen-specific

antibodies. *Nat. Biotechnol.* **24**, 703–707 (2006).

49. Choi, J. H. *et al.* Development and optimization of a process for automated recovery of single cells identified by microengraving. *Biotechnol. Prog.* **26**, 888–895 (2010).

50. Mazutis, L. *et al.* Single-cell analysis and sorting using droplet-based microfluidics. *Nat. Protoc.* **8**, 870–891 (2013).

51. Eyer, K. *et al.* Single-cell deep phenotyping of IgG-secreting cells for high-resolution immune monitoring. *Nat. Biotechnol.* **35**, 977–982 (2017).

52. Tiller, T. *et al.* Efficient generation of monoclonal antibodies from single human B cells by single cell RT-PCR and expression vector cloning. *J. Immunol. Methods* **329**, 112–124 (2008).

53. Tiller, T., Busse, C. E. & Wardemann, H. Cloning and expression of murine Ig genes from single B cells. *J. Immunol. Methods* **350**, 183–193 (2009).

54. Dekosky, B. J. *et al.* High-throughput sequencing of the paired human immunoglobulin heavy and light chain repertoire. *Nat. Biotechnol.* **31**, 166–169 (2013).

55. DeKosky, B. J. *et al.* In-depth determination and analysis of the human paired heavy- and light-chain antibody repertoire. *Nat. Med.* **21**, 86–91 (2015).

56. Mcdaniel, J. R., DeKosky, B. J., Tanno, H., Ellington, A. D. & Georgiou, G. Ultra-high-throughput sequencing of the immune receptor repertoire from millions of lymphocytes. *Nat. Protoc.* **11**, 429–442 (2016).

57. Parola, C., Neumeier, D. & Reddy, S. T. Integrating high-throughput screening and sequencing for monoclonal antibody discovery and engineering. *Immunology* vol. 153 31–41 (2018).

58. Wurm, F. M. Production of recombinant protein therapeutics in cultivated mammalian

cells. *Nature Biotechnology* vol. 22 1393–1398 (2004).

59. Hodgson, J. The pandemic pipeline. *Nat. Biotechnol.* (2020) doi:10.1038/d41587-020-00005-z.

60. Sander, B., Andersson, J. & Andersson, U. Assessment of Cytokines by Immunofluorescence and the Paraformaldehyde-Saponin Procedure. *Immunol. Rev.* **119**, 65–93 (1991).

61. Freer, G. & Rindi, L. Intracellular cytokine detection by fluorescence-activated flow cytometry: Basic principles and recent advances. *Methods* **61**, 30–38 (2013).

62. Chen, Z., Chen, J. J. & Fan, R. Single-Cell Protein Secretion Detection and Profiling. *Annu. Rev. Anal. Chem.* **12**, 431–449 (2019).

63. Li, M. *et al.* A Gelatin Microdroplet Platform for High-Throughput Sorting of Hyperproducing Single-Cell-Derived Microalgal Clones. *Small* **14**, 1803315 (2018).

64. Park, S., Han, J., Kim, W., Lee, G. M. & Kim, H. S. Rapid selection of single cells with high antibody production rates by microwell array. *J. Biotechnol.* **156**, 197–202 (2011).

65. Chiou, P. Y., Ohta, A. T. & Wu, M. C. Massively parallel manipulation of single cells and microparticles using optical images. *Nature* **436**, 370–372 (2005).

66. Le, K. *et al.* A novel mammalian cell line development platform utilizing nanofluidics and optoelectro positioning technology. *Biotechnol. Prog.* **34**, 1438–1446 (2018).

67. Novak, R. *et al.* Single-Cell Multiplex Gene Detection and Sequencing with Microfluidically Generated Agarose Emulsions. *Angew. Chemie Int. Ed.* **50**, 390–395 (2011).

68. Hatori, M. N., Kim, S. C. & Abate, A. R. Particle-Templated Emulsification for Microfluidics-Free Digital Biology. *Anal. Chem.* **90**, 9813–9820 (2018).

69. Herzenberg, L. A. *et al. The History and Future of the Fluorescence Activated Cell Sorter and Flow Cytometry: A View from Stanford*. (2002).

70. Ma, S. *et al.* Fabrication of Microgel Particles with Complex Shape via Selective Polymerization of Aqueous Two-Phase Systems. *Small* **8**, 2356–2360 (2012).

71. Liu, Q. *et al.* Self-Orienting Hydrogel Micro-Buckets as Novel Cell Carriers. *Angew. Chemie Int. Ed.* **58**, 547–551 (2019).

72. Collins, D. J., Neild, A., deMello, A., Liu, A. Q. & Ai, Y. The Poisson distribution and beyond: Methods for microfluidic droplet production and single cell encapsulation. *Lab on a Chip* vol. 15 3439–3459 (2015).

73. Basu, A. S. Digital Assays Part II: Digital Protein and Cell Assays. *SLAS Technol.* **22**, 387–405 (2017).

74. Ha, K., de Rutte, J., Di Carlo, D. & Bertozzi, A. Minimal surface configurations for axisymmetric microparticles. *Prep.*

75. Hong, J. K., Lakshmanan, M., Goudar, C. & Lee, D. Y. Towards next generation CHO cell line development and engineering by systems approaches. *Current Opinion in Chemical Engineering* vol. 22 1–10 (2018).

76. Zhong, X. & Rescorla, F. J. Cell surface adhesion molecules and adhesion-initiated signaling: Understanding of anoikis resistance mechanisms and therapeutic opportunities. *Cellular Signalling* vol. 24 393–401 (2012).

77. Fraietta, J. A. *et al.* Determinants of response and resistance to CD19 chimeric antigen receptor (CAR) T cell therapy of chronic lymphocytic leukemia. *Nat. Med.* **24**, 563–571 (2018).

78. Dimatteo, R., Darling, N. J. & Segura, T. In situ forming injectable hydrogels for drug

delivery and wound repair. *Adv. Drug Deliv. Rev.* **127**, 167–184 (2018).

79. Shibata, H. *et al.* Injectable hydrogel microbeads for fluorescence-based in vivo continuous glucose monitoring. *Proc. Natl. Acad. Sci. U. S. A.* **107**, 17894–8 (2010).

80. Griffin, D. R., Weaver, W. M., Scumpia, P. O., Di Carlo, D. & Segura, T. Accelerated wound healing by injectable microporous gel scaffolds assembled from annealed building blocks. *Nat. Mater.* **14**, 737–744 (2015).

81. Xin, S., Wyman, O. M. & Alge, D. L. Assembly of PEG Microgels into Porous Cell-Instructive 3D Scaffolds via Thiol-Ene Click Chemistry. *Adv. Healthc. Mater.* **7**, 1800160 (2018).

82. Sideris, E. *et al.* Particle Hydrogels Based on Hyaluronic Acid Building Blocks. *ACS Biomater. Sci. Eng.* **2**, 2034–2041 (2016).

83. Nih, L. R., Sideris, E., Carmichael, S. T. & Segura, T. Injection of Microporous Annealing Particle (MAP) Hydrogels in the Stroke Cavity Reduces Gliosis and Inflammation and Promotes NPC Migration to the Lesion. *Adv. Mater.* **29**, 1606471 (2017).

84. Mealy, J. E. *et al.* Injectable Granular Hydrogels with Multifunctional Properties for Biomedical Applications. *Adv. Mater.* **30**, 1705912 (2018).

85. Sheikhi, A. *et al.* Microfluidic-enabled bottom-up hydrogels from annealable naturally-derived protein microbeads. *Biomaterials* (2018) doi:10.1016/J.BIOMATERIALS.2018.10.040.

86. Koh, J. *et al.* Delivery within a self-assembling, monodisperse particle hydrogel forms a microporous scaffold niche for enhanced tissue maintenance of mesenchymal stem cells in vivo. *Submitted.*

87. Nisisako, T. & Torii, T. Microfluidic large-scale integration on a chip for mass production

of monodisperse droplets and particles. *Lab Chip* **8**, 287–293 (2008).

88. Jeong, H.-H., Yelleswarapu, V. R., Yadavali, S., Issadore, D. & Lee, D. Kilo-scale droplet generation in three-dimensional monolithic elastomer device (3D MED). *Lab Chip* **15**, 4387–4392 (2015).

89. Li, W., Greener, J., Voicu, D. & Kumacheva, E. Multiple modular microfluidic (M3) reactors for the synthesis of polymer particles. *Lab Chip* **9**, 2715 (2009).

90. Ofner, A. *et al.* High-Throughput Step Emulsification for the Production of Functional Materials Using a Glass Microfluidic Device. *Macromol. Chem. Phys.* **218**, 1600472 (2017).

91. Håti, A. G., Szymborski, T. R., Steinacher, M. & Amstad, E. Production of monodisperse drops from viscous fluids. *Lab Chip* **18**, 648–654 (2018).

92. Yadavali, S., Jeong, H.-H., Lee, D. & Issadore, D. Silicon and glass very large scale microfluidic droplet integration for terascale generation of polymer microparticles. *Nat. Commun.* **9**, 1222 (2018).

93. Conchouso, D., Castro, D., Khan, S. A. & Foulds, I. G. Three-dimensional parallelization of microfluidic droplet generators for a litre per hour volume production of single emulsions. *Lab Chip* **14**, 3011 (2014).

94. Krutkramelis, K., Xia, B. & Oakey, J. Monodisperse polyethylene glycol diacrylate hydrogel microsphere formation by oxygen-controlled photopolymerization in a microfluidic device. *Lab Chip* **16**, 1457–1465 (2016).

95. Rossow, T. *et al.* Controlled Synthesis of Cell-Laden Microgels by Radical-Free Gelation in Droplet Microfluidics. *J. Am. Chem. Soc.* **134**, 4983–4989 (2012).

96. Sugiura, S., Nakajima, M., Iwamoto, S. & Seki, M. Interfacial Tension Driven

Monodispersed Droplet Formation from Microfabricated Channel Array. *Langmuir* **17**, 5562–5566 (2001).

97. Shinji, S., Nakajima, M. & Seki, M. Effect of Channel Structure on Microchannel Emulsification. *Langmuir* **18**, 5708–5712 (2002).

98. Amstad, E. *et al.* Robust scalable high throughput production of monodisperse drops. *Lab Chip* **16**, 4163–4172 (2016).

99. Sugiura, S., Nakajima, M., Tong, J., Nabetani, H. & Seki, M. Preparation of Monodispersed Solid Lipid Microspheres Using a Microchannel Emulsification Technique. *J. Colloid Interface Sci.* **227**, 95–103 (2000).

100. Dangla, R., Kayi, S. C. & Baroud, C. N. Droplet microfluidics driven by gradients of confinement. *Proc. Natl. Acad. Sci.* **110**, 853–858 (2013).

101. Nisisako, T. & Torii, T. Microfluidic large-scale integration on a chip for mass production of monodisperse droplets and particles. *Lab Chip* **8**, 287–293 (2008).

102. Amstad, E. *et al.* Parallelization of microfluidic flow-focusing devices. *Phys. Rev. E* **95**, 043105 (2017).

103. Headen, D. M., García, J. R. & García, A. J. Parallel droplet microfluidics for high throughput cell encapsulation and synthetic microgel generation. *Microsystems Nanoeng.* **4**, 17076 (2018).

104. Nie, Z. *et al.* Emulsification in a microfluidic flow-focusing device: effect of the viscosities of the liquids. *Microfluid. Nanofluidics* **5**, 585–594 (2008).

105. Kobayashi, I., Wada, Y., Uemura, K. & Nakajima, M. Microchannel emulsification for mass production of uniform fine droplets: integration of microchannel arrays on a chip. *Microfluid. Nanofluidics* **8**, 255–262 (2010).

106. Tan, W.-H. & Takeuchi, S. Monodisperse Alginate Hydrogel Microbeads for Cell Encapsulation. *Adv. Mater.* **19**, 2696–2701 (2007).

107. Utech, S. *et al.* Microfluidic Generation of Monodisperse, Structurally Homogeneous Alginate Microgels for Cell Encapsulation and 3D Cell Culture. *Adv. Healthc. Mater.* **4**, 1628–1633 (2015).

108. M. P. Lutolf & Hubbell, J. A. Synthesis and Physicochemical Characterization of End-Linked Poly(ethylene glycol)-co-peptide Hydrogels Formed by Michael-Type Addition. *Biomacromolecules* **4**, 713–722 (2003).

109. Darling, N. J., Hung, Y.-S., Sharma, S. & Segura, T. Controlling the kinetics of thiol-maleimide Michael-type addition gelation kinetics for the generation of homogenous poly(ethylene glycol) hydrogels. *Biomaterials* **101**, 199–206 (2016).

110. Hoyle, C. E., Lee, T. Y. & Roper, T. Thiol-enes: Chemistry of the past with promise for the future. *J. Polym. Sci. Part A Polym. Chem.* **42**, 5301–5338 (2004).

111. Bott, K. *et al.* The effect of matrix characteristics on fibroblast proliferation in 3D gels. *Biomaterials* **31**, 8454–8464 (2010).

112. Stachowiak, A. N., Bershteyn, A., Tzatzalos, E. & Irvine, D. J. Bioactive Hydrogels with an Ordered Cellular Structure Combine Interconnected Macroporosity and Robust Mechanical Properties. *Adv. Mater.* **17**, 399–403 (2005).

113. Koshy, S. T., Ferrante, T. C., Lewin, S. A. & Mooney, D. J. Injectable, porous, and cell-responsive gelatin cryogels. *Biomaterials* **35**, 2477–2487 (2014).

114. Hockaday, L. A. *et al.* Rapid 3D printing of anatomically accurate and mechanically heterogeneous aortic valve hydrogel scaffolds. *Biofabrication* **4**, 035005 (2012).

115. Rhee, S., Puetzer, J. L., Mason, B. N., Reinhart-King, C. A. & Bonassar, L. J. 3D

Bioprinting of Spatially Heterogeneous Collagen Constructs for Cartilage Tissue Engineering. *ACS Biomater. Sci. Eng.* **2**, 1800–1805 (2016).

116. Yin, H., Ding, Y., Zhai, Y., Tan, W. & Yin, X. Orthogonal programming of heterogeneous micro-mechano-environments and geometries in three-dimensional bio-stereolithography. *Nat. Commun.* **9**, 4096 (2018).

117. Norris, S. C. P., Tseng, P. & Kasko, A. M. Direct Gradient Photolithography of Photodegradable Hydrogels with Patterned Stiffness Control with Submicrometer Resolution. *ACS Biomater. Sci. Eng.* **2**, 1309–1318 (2016).

118. Hribar, K. C., Choi, Y. S., Ondeck, M., Engler, A. J. & Chen, S. Digital Plasmonic Patterning for Localized Tuning of Hydrogel Stiffness. *Adv. Funct. Mater.* **24**, 4922–4926 (2014).

119. Darling, N. J., Sideris, E., Hamada, N., Carmichael, S. T. & Segura, T. Injectable and Spatially Patterned Microporous Annealed Particle (MAP) Hydrogels for Tissue Repair Applications. *Adv. Sci.* 1801046 (2018) doi:10.1002/advs.201801046.

120. Discher, D. E., Janmey, P. & Wang, Y. Tissue Cells Feel and Respond to the Stiffness of Their Substrate. *Science (80-. ).* **310**, 1139–1143 (2005).

121. Isenberg, B. C., DiMilla, P. A., Walker, M., Kim, S. & Wong, J. Y. Vascular Smooth Muscle Cell Durotaxis Depends on Substrate Stiffness Gradient Strength. *Biophys. J.* **97**, 1313–1322 (2009).

122. Vincent, L. G., Choi, Y. S., Alonso-Latorre, B., del Álamo, J. C. & Engler, A. J. Mesenchymal stem cell durotaxis depends on substrate stiffness gradient strength. *Biotechnol. J.* **8**, 472–84 (2013).

123. Engler, A. J., Sen, S., Sweeney, H. L. & Discher, D. E. Matrix Elasticity Directs Stem

Cell Lineage Specification. *Cell* **126**, 677–689 (2006).

124. Plodinec, M. *et al.* The nanomechanical signature of breast cancer. *Nat. Nanotechnol.* **7**, 757–765 (2012).

125. Xiao, W., Sohrabi, A. & Seidlits, S. K. Integrating the glioblastoma microenvironment into engineered experimental models. *Futur. Sci. OA* **3**, FSO189 (2017).

126. Matsunaga, Y. T., Morimoto, Y. & Takeuchi, S. Molding Cell Beads for Rapid Construction of Macroscopic 3D Tissue Architecture. *Adv. Mater.* **23**, H90–H94 (2011).

127. Highley, C. B., Song, K. H., Daly, A. C. & Burdick, J. A. Jammed Microgel Inks for 3D Printing Applications. *Adv. Sci.* **6**, (2019).

128. Xin, S., Chimene, D., Garza, J. E., Gaharwar, A. K. & Alge, D. L. Clickable PEG hydrogel microspheres as building blocks for 3D bioprinting. *Biomater. Sci.* (2019) doi:10.1039/C8BM01286E.

129. Jeon, O., Lee, Y. B., Hinton, T. J., Feinberg, A. W. & Alsberg, E. Cryopreserved cell-laden alginate microgel bioink for 3D bioprinting of living tissues. *Mater. Today Chem.* **12**, 61–70 (2019).

130. Sheikhi, A. *et al.* Microfluidic-enabled bottom-up hydrogels from annealable naturally-derived protein microbeads. *Biomaterials* **192**, 560–568 (2019).

131. de Rutte, J. M., Koh, J. & Di Carlo, D. Scalable High-Throughput Production of Modular Microgels for In Situ Assembly of Microporous Tissue Scaffolds. *Adv. Funct. Mater.* 1900071 (2019) doi:10.1002/adfm.201900071.

132. Koh, J. *et al.* Enhanced In Vivo Delivery of Stem Cells using Microporous Annealed Particle Scaffolds. *Small* **15**, 1903147 (2019).

133. Kawata, S., Sun, H. B., Tanaka, T. & Takada, K. Finer features for functional

microdevices - Micromachines can be created with higher resolution using two-photon absorption. *Nature* (2001).

134. Huang, F. *et al.* Two-Photon Lithographic Patterning of DNA-Coated Single-Microparticle Surfaces. *Nano Lett.* (2019) doi:10.1021/acs.nanolett.8b04975.

135. Dendukuri, D., Pregibon, D. C., Collins, J., Hatton, T. A. & Doyle, P. S. Continuous-flow lithography for high-throughput microparticle synthesis. *Nat. Mater.* **5**, 365–369 (2006).

136. Dendukuri, D., Gu, S. S., Pregibon, D. C., Hatton, T. A. & Doyle, P. S. Stop-flow lithography in a microfluidic device. *Lab Chip* **7**, 818–828 (2007).

137. Chung, S. E. *et al.* Optofluidic maskless lithography system for real-time synthesis of photopolymerized microstructures in microfluidic channels. *Appl. Phys. Lett.* **91**, 041106 (2007).

138. Wu, C.-Y., Owsley, K. & Di Carlo, D. Rapid Software-Based Design and Optical Transient Liquid Molding of Microparticles. *Adv. Mater.* **27**, 7970–7978 (2015).

139. Stoecklein, D. *et al.* FlowSculpt: Software for efficient design of inertial flow sculpting devices. *Lab Chip* (2019) doi:10.1039/c9lc00658c.

140. Destgeer, G., Ouyang, M., Wu, C.-Y. & Di Carlo, D. Formation of uniform reaction volumes using concentric amphiphilic microparticles. *bioRxiv* 2020.03.15.992321 (2020) doi:10.1101/2020.03.15.992321.

141. Paulsen, K. S., Di Carlo, D. & Chung, A. J. Optofluidic fabrication for 3D-shaped particles. *Nat. Commun.* **6**, 6976 (2015).

142. Yuan, R. *et al.* Designable 3D Microshapes Fabricated at the Intersection of Structured Flow and Optical Fields. *Small* **14**, 1803585 (2018).

143. de Rutte, J. M., Koh, J. & Di Carlo, D. Scalable High-Throughput Production of Modular

Microgels for In Situ Assembly of Microporous Tissue Scaffolds. *Adv. Funct. Mater.* (2019) doi:10.1002/adfm.201900071.

144. Yanagisawa, M., Nigorikawa, S., Sakaue, T., Fujiwara, K. & Tokita, M. Multiple patterns of polymer gels in microspheres due to the interplay among phase separation, wetting, and gelation. *Proc. Natl. Acad. Sci. U. S. A.* **111**, 15894–15899 (2014).

145. Forciniti, D., Hall, C. K. & Kula, M. R. Influence of polymer molecular weight and temperature on phase composition in aqueous two-phase systems. *Fluid Phase Equilib.* **61**, 243–262 (1991).

146. Snyder, S. M., Cole, K. D. & Sziag, D. C. Phase Compositions, Viscosities, and Densities for Aqueous Two-Phase Systems Composed of Polyethylene Glycol and Various Salts at 25 °C. *J. Chem. Eng. Data* **37**, 268–274 (1992).

# Appendix A

## Supporting information for Chapter 2

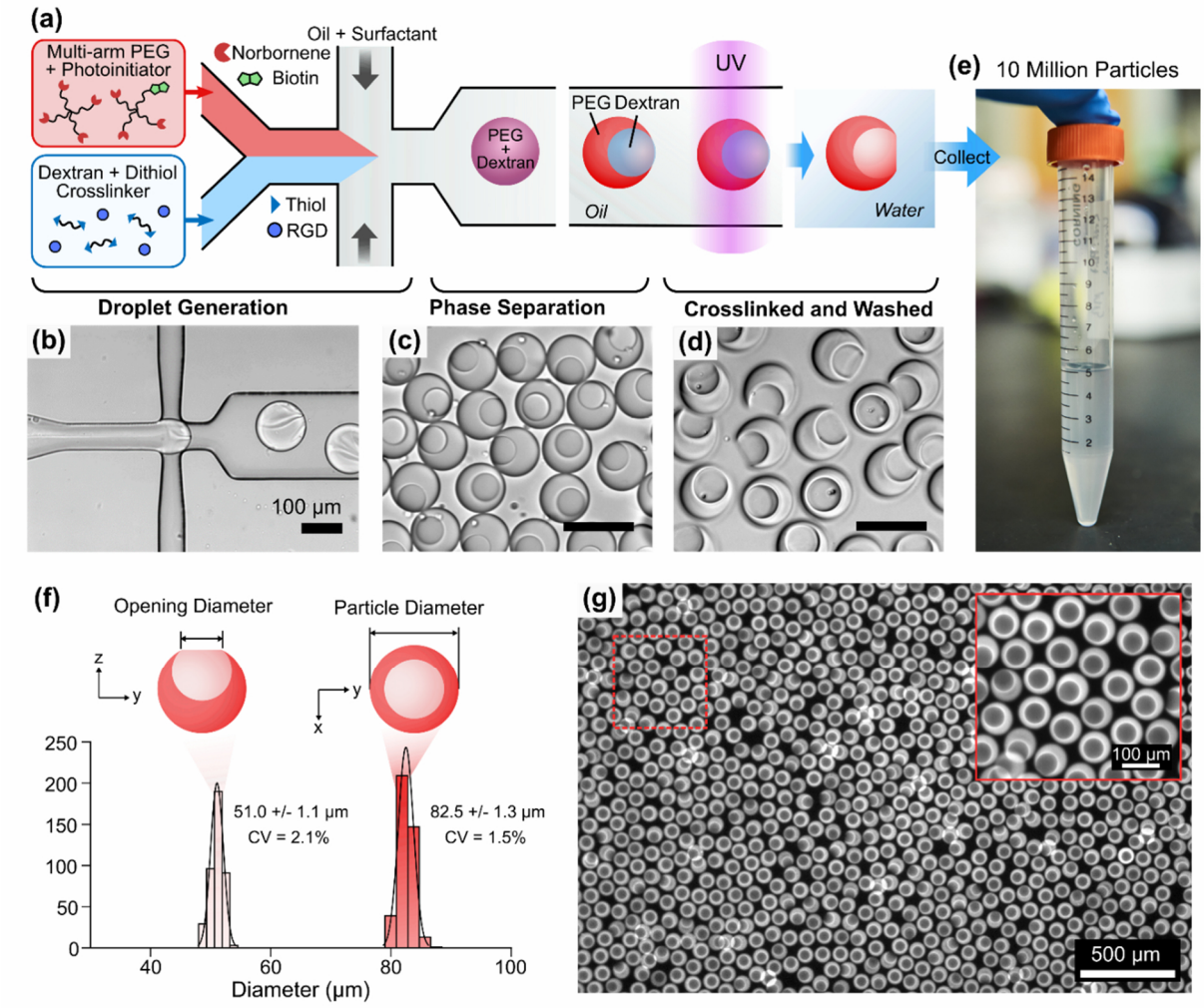


**Figure A-1. Drop-carrier particle fabrication using an aqueous two-phase system combined with droplet microfluidics.** (a) A solution comprised of UV reactive PEG and photoinitiator is co-flowed with a solution containing dextran, dithiol crosslinkers, and RGD peptides in a microfluidic droplet generator. (b) A third solution of oil and surfactant is injected into the device to generate water-in-oil droplets at a rate of ~1000 Hz. (c) Downstream on the device PEG and dextran undergo phase separation resulting in two distinct regions in the droplet. The droplets are exposed with UV light at the end of the device to crosslink the PEG rich portion of the droplet, while the dextran rich region remains as a liquid. (d) The resulting microparticles are then collected, washed to remove oil and dextran, and stored for later use. (e) Photograph of a 15 mL conical tube with 10 million drop-carrier particles fabricated in ~3 hours. (f) Drop-carrier particles fabricated using this approach are highly monodisperse with outer diameter CV of 1.5% and cavity opening diameter CV of 2.1% (n = 409). Particle uniformity was calculated by analyzing fluorescence microscopy images using a custom image analysis algorithm in MATLAB. (g) Example fluorescence microscopy image of biotinylated drop-carrier particles stained with Alexa Fluor 568 Streptavidin. A large fraction of the seeded particles settles with their cavities exposed upright.

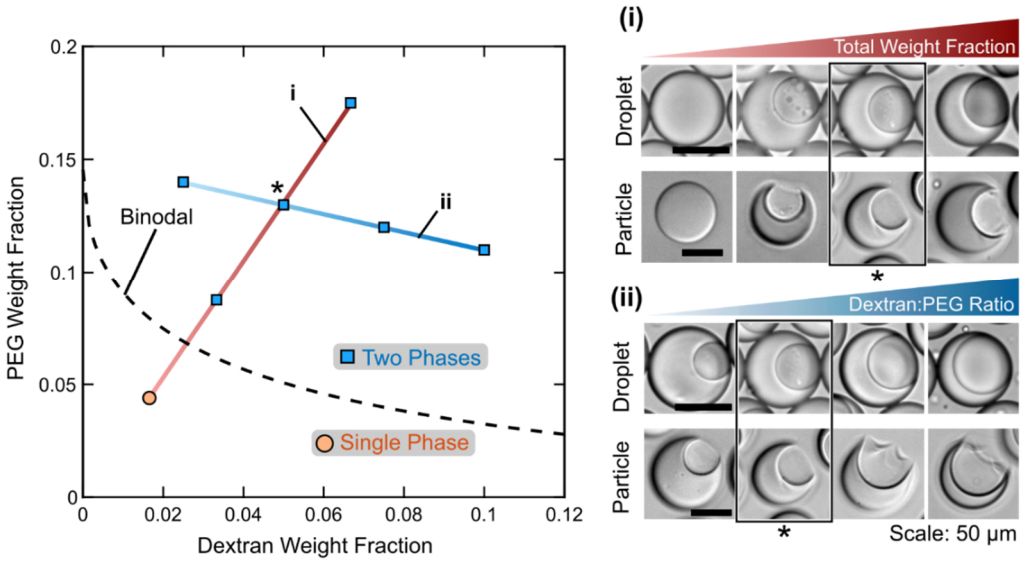


**Figure A-2. Drop-carrier particle morphology can be tuned by adjusting the concentrations of PEG and dextran in the droplet precursors.** At very low concentrations phase separation does not occur resulting in a spherical particle (i). As the total concentration of PEG and dextran is increased above the binodal line, phase separation occurs enabling fabrication of cavity-containing microparticles. The relative opening diameter of the particle cavity is increased by increasing the total polymer concentration (i). By adjustizng the concentration ratio of dextran and PEG, particles can be fabricated with different relative cavity sizes (inner cavity diameter : outer particle diameter). Particles fabricated using a PEG concentration of 13% and dextran concentration of 5% (denoted by *) were found to have high structural integrity while maintaining a relatively large cavity opening to enabled efficient cell loading. This condition was used for all other experiments in this work.

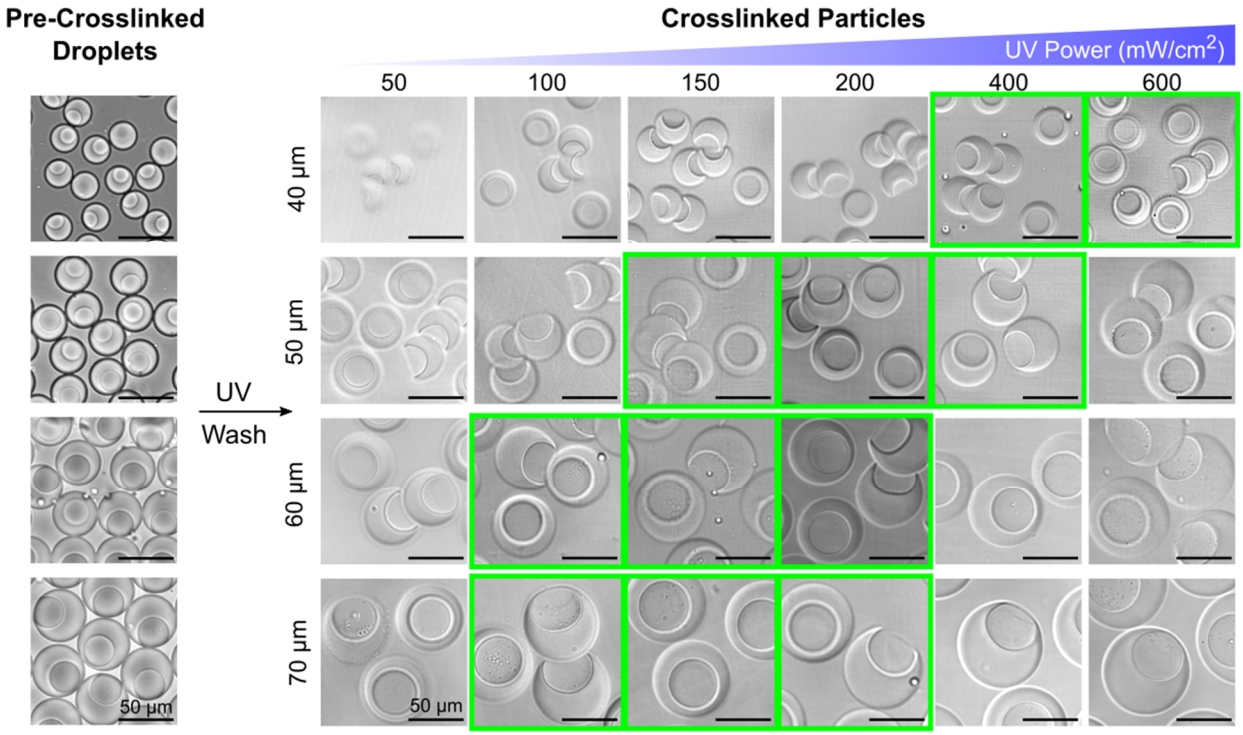


**Figure A-3. Fabrication of different sizes of drop-carrier particles.**Pre-crosslinked droplets containing PEG and dextran were fabricated using flow focusing devices with a range of channel heights (18, 35, 55 µm). For each size a range of UV intensities was tested to determine the optimal conditions for proper particle fabrication. When the intensity is too low particles lightly cross-linked and are mechanically unstable. When the intensity is too high excess PEG in the dextran rich phase begins to crosslink resulting in particles that tend to swell more and have less exposed cavities. Here the optimal range of UV intensities is highlighted in green.

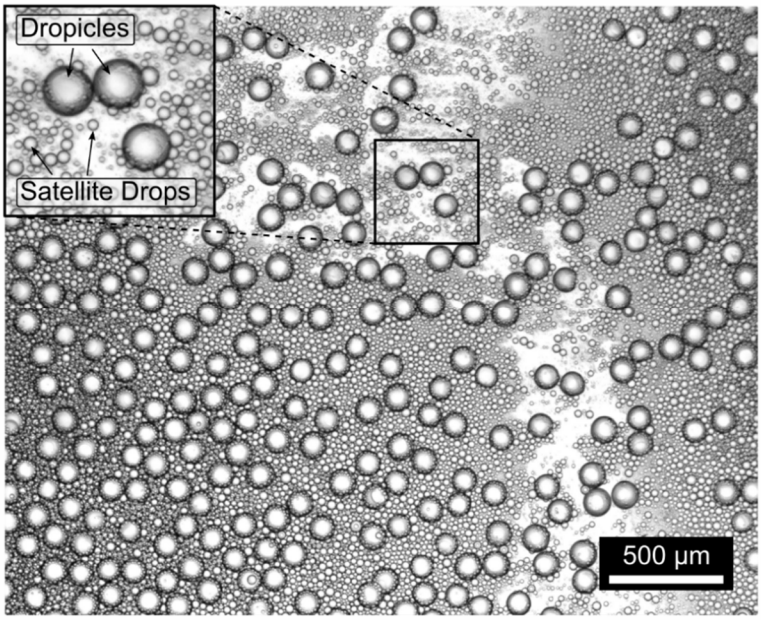


**Figure A-4. Brightfield image of dropicles and satellite droplet formed via pipetting.** Droplets formed with the particles (dropicles) are uniform in size while excess fluids are broken up into smaller non-uniform satellite droplets which are observed in the background of the image.

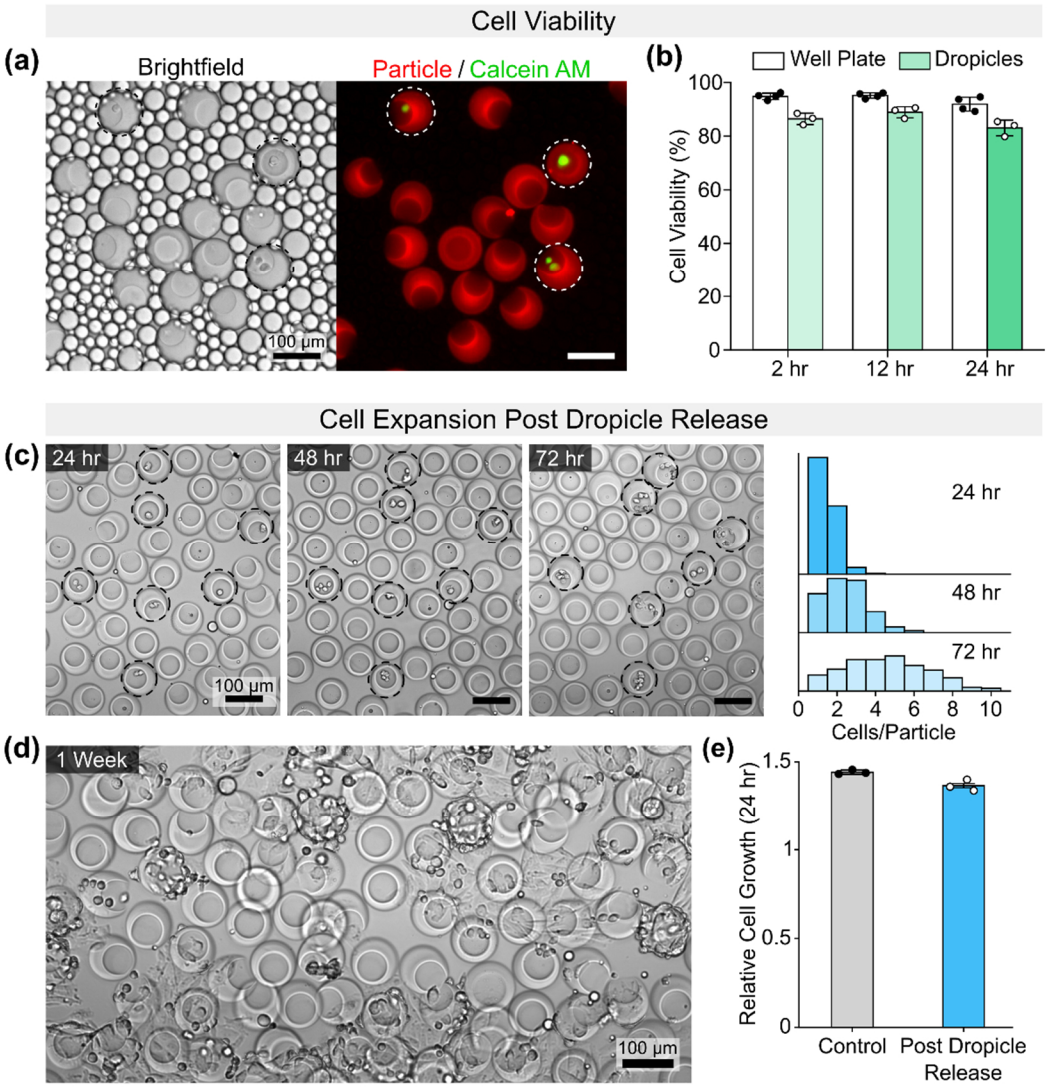


**Figure A-5. Characterization of cell viability and growth after dropicle formation and release.**(a) Brightfield and fluorescence microscopy image of cells encapsulated in dropicles. Biotinylated drop-carrier particles are stained with Alexa Fluor 568 streptavidin and cells are stained with calcein AM. (b) Cells maintained high viability after dropicle formation and release. Viability was assessed by staining with calcein AM and propidium iodide after recovering particles and cells from droplets. Live/dead assay was performed with a minimum of n =3 samples, cell number > 1000 per condition. (c) Cells initially remain in the drop-carrier particle cavities after releasing them. Colonies derived from single cells remain in the particle cavities during initial expansion. (d) After significant accumulation of cells in the cavities, cells begin to spread to the outside of the cavities and onto the well plate surface. (e) Cell growth in drop-carrier particles post dropicle release is comparable to cell growth on standard well plates (control) (n = 3). Growth is characterized by fold change in cell number over a 24 hr period as characterized by counting cell number using CellTracker staining.

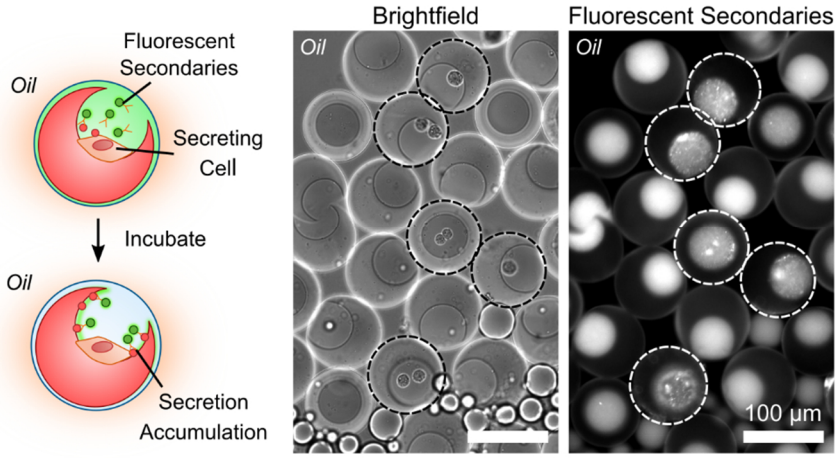


**Figure A-6. Visualization of secretion accumulation on the particle surface during single cell dropicle incubation.** Fluorescent anti-human IgG secondaries were included in the dispersed phase prior to dropicle formation. After incubating CHO cells for 24 hours, fluorescence imaging revealed accumulation of the secondaries onto the surface of particles containing cells while dropicles without cells see a uniformly diffuse fluorescent signal. It was also noted that cells were able to divide during the longer incubation step.

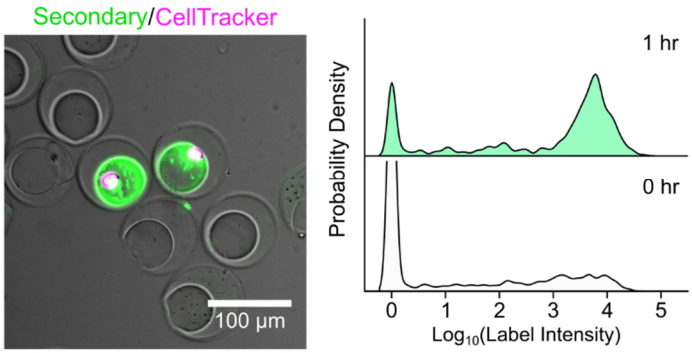


**Figure A-7. Secretion Assay performed on suspension-adapted CHO DP-12 cells using the dropicle platform.** (Left) Example microscopy image of particles with associated cells and secretion signal after performing the assay. Cells remain attached to particles through the assay steps despite being adapted to suspension culture. (Right) An increase in secretions is observed after 1 hr of incubation as expected, providing validation that the assay is compatible with suspension-adapted CHO cells. For each condition > 700 particles with cells were analyzed.

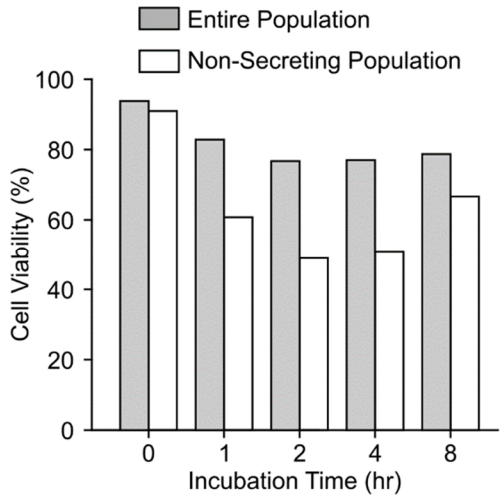


**Figure A-8. Viability assessment of CHO DP-12 cells after dropicle incubation sweep.** The viability of the non-secreting population is less than the entire population. However, a substantial fraction of non-secreting cells remains viable indicating there is a subpopulation of cells not producing human IgG.

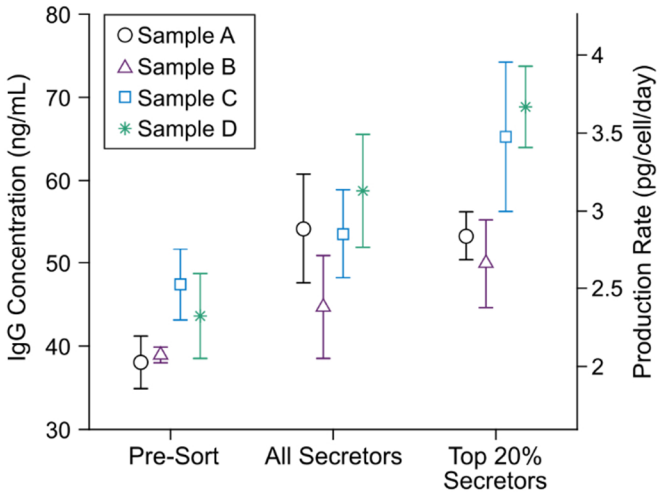


**Figure A-9. ELISA measurements of each sorted sub-population of Anti-IL8 secreting CHO cells.** For each sample (n = 4) two separate sorting conditions were performed: (1) All cells with signal distinguishable from background (All Secretors) and (2) top 20% of secreting cells by measured secretion amount. An increase in IgG production was measured for all the sorted samples relative to the pre-sort control samples. In the highest producing sample (Top 20% Secretors, Sample D), a 58% increase in IgG production was measured relative to the pre-sort control sample.

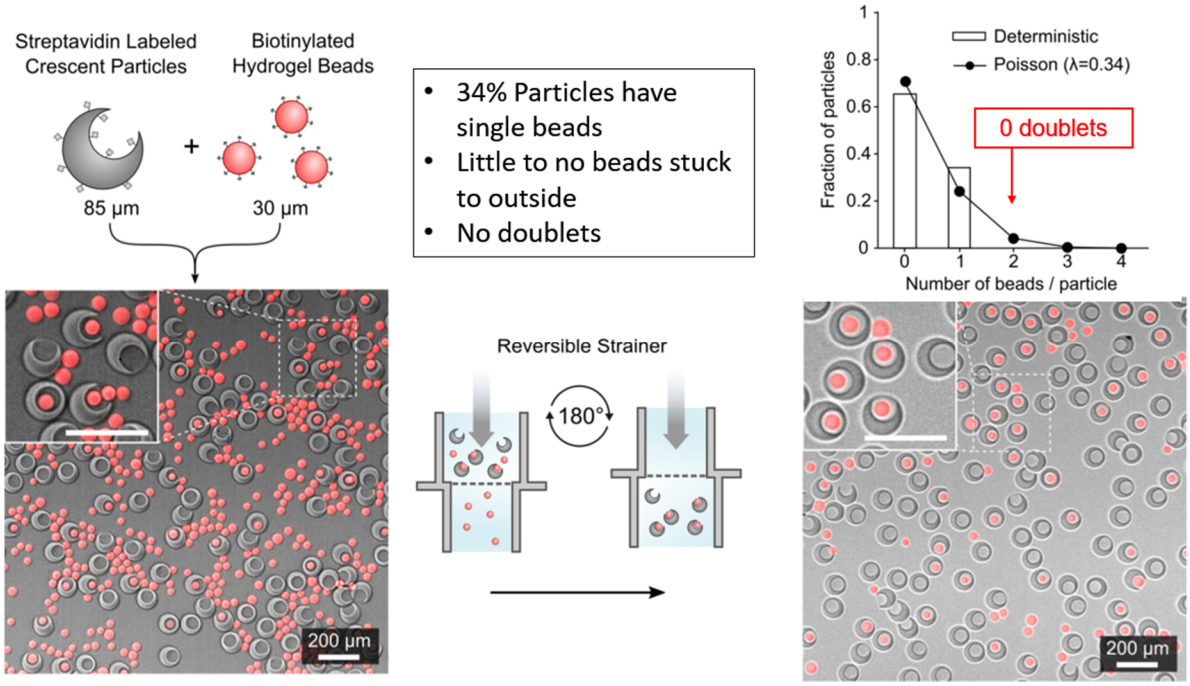


**Figure A-10. Demonstration of deterministic loading of hydrogel beads into crescent shaped drop-carrier particles.** Here biotinylated hydrogel beads that are 30 µm in diameter are mixed with streptavidin labeled crescent particles with an outer diameter of 85 µm and a cavity opening size of ~ 50 µm. After incubation and removal of excess beads we see a high fraction of crescent particles with a single bead captured in its cavity (34%). Here the specific size of the particle cavities prevented multiple beads from being loaded into the particles. This size restriction feature can potentially be employed to improve single cell loading efficiency for cell-based assays.

# Appendix B

## Dropicle Volume Uniformity and Encapsulation Efficiency Theory

Here I will discuss a theoretical analysis of **(1)** the volume uniformity of droplets formed using dropicles with different morphologies as well as **(2)** the efficiency of the encapsulation of the sample of interest into the dropicles. For the analysis we will assume that the water or sample volume is only contained in the space outside of the physical body of the particles. This assumption is appropriate for applications where the sample species cannot freely diffuse through the particle matrix. Examples include biomolecules larger than the pores of the hydrogel particles (e.g. large proteins, DNA), or microscale objects such as cells.

### Volume Uniformity

Here we consider drop-carrier particles with both a spherical morphology as well as the crescent morphology used in chapter 2. We assume that the particle geometry is fixed while the diameter of the droplet formed around the particle has some variability. For a given variation in this diameter we ask: what is the corresponding variation in encapsulated water volume outside of the body of the particle (volume between the particle and outer droplet boundary as well as the volume within the cavity).

For a standard droplet, volume variation is related to the variation in diameter by:

$$CV_{drop}^{Vol} = 3 \times CV_{diameter} \qquad \textbf{Equation B-1}$$

where $CV$ is the coefficient of variation defined as

$$CV = \frac{Standard\ Deviation}{Mean}. \qquad \textbf{Equation B-2}$$

For a spherical dropicle (i.e. a droplet formed with a spherical particle), the variation in volume is defined as

$$CV_{sphere}^{Vol} = CV_{drop}^{Vol} \times \frac{V_{drop}}{V_{water}^{sphere}} \qquad \textbf{Equation B-3}$$

where

$$V_{droplet} = \frac{\pi}{6}\left(D_{drop}\right)^3$$

$$V_{water}^{sphere} = V_{drop} - V_{sphere}$$

$$V_{sphere} = \frac{\pi}{6}(D_{out})^3.$$

and $D_{droplet}$ is the diameter of the droplet and $D_{out}$ is the outer diameter of the particle. For a dropicle formed with the crescent shaped particles depicted in **Figure B-1**, the volume variation can be approximated as

$$CV_{crescent}^{Vol} = CV_{drop}^{Vol} \times \frac{V_{drop}}{V_{water}^{crescent}} \qquad \textbf{Equation B-4}$$

where

$$V_{drop} = \frac{\pi}{6}\left(D_{drop}\right)^3$$

$$V_{water}^{crescent} = V_{drop} - V_{crescent}$$

$$V_{crescent} = \frac{\pi}{6}(D_{out})^3 - \frac{\pi}{6}(D_{in})^3$$

and $D_{in}$ is the diameter of the excluded sphere that makes up the particle cavity.

Using these expressions for volume variations we can now apply them to gain insight on how parameters such as particle shape and thickness of the outer droplet layer affects the variation for some perturbation in droplet diameter $\Delta D_{drop}$. Here we normalize the thickness of the outer water layer and define it as

$$(D_{drop} - D_{out})/D_{drop}. \qquad \textbf{Equation B-5}$$

For the same perturbation $\Delta D_{drop}$, volume variation is expected to be minimal for a spherical droplet, therefor we will normalize the variation in dropicle volume by this value. For a spherical dropicle this normalized volume variation is then

$$\frac{CV_{sphere}^{Vol}}{CV_{drop}^{Vol}} = \frac{CV_{drop}^{Vol} \times \frac{V_{drop}}{V_{water}^{sphere}}}{CV_{drop}^{Vol}} = \frac{V_{drop}}{V_{water}^{sphere}} \qquad \textbf{Equation B-6}$$

and for a dropicle formed with a crescent particle

$$\frac{CV_{crescent}^{Vol}}{CV_{drop}^{Vol}} = \frac{CV_{drop}^{Vol} \times \frac{V_{drop}}{V_{water}^{crescent}}}{CV_{drop}^{Vol}} = \frac{V_{drop}}{V_{water}^{crescent}}. \qquad \textbf{Equation B-7}$$

This normalized volume variation plotted over a range of conditions in **Figure B-1.** We see that for all cases volume variation for dropicles formed with crescent particles is substantially less than for spherical particles. This intuitively makes sense as the whole volume supported by a

spherical particle is contained in the layer between the particle and the droplet interface and is thus substantially affected by any variation in this thickness. For the crescent particles a fraction of the volume is contained within the cavity of the particle which helps to buffer against this variation. In case (i) we see nearly a 10-fold higher variation in volume for the spherical dropicle compared with the crescent dropicle with a large cavity. Further, we note that in general increasing the relative size of the cavity compared to the outer diameter of the particle will reduce variation. In the limit that the cavity is the size of the particle we see that the expression asymptotically approaches the solution for variation of a standard droplet.

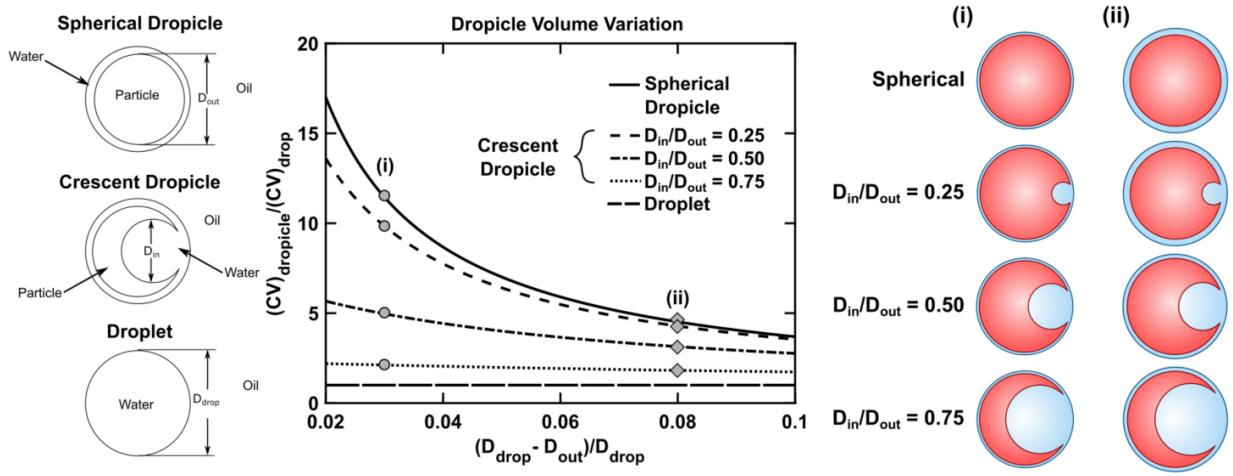


**Figure B-1 Theoretical dropicle volume variation for different geometries.** Here we consider variation in normalize dropicle volume as a function of the normalized outer water layer thickness. Variation is reduced with the addition of a cavity, and improves as the cavity size increases relative to the outer diameter of the particle. In cases where the water layer between the particle and the oil interface decreases (i), we note nearly a 10-fold improvement in volume uniformity for the crescent dropicle in comparison to the spherical dropicle.

## Encapsulation Efficiency

Here we will explore numerically how variation in various particle parameters effect the efficiency of encapsulation of samples into dropicles. Specifically, we consider concentrated drop-carrier particles dispersed in some aqueous sample phase to be encapsulated (e.g. suspension of biomolecules or cells). This theory can be used as an approximation of expected encapsulation efficiency of suspended cells (**Figure B-2** Depiction of suspended cells being encapsulated with the dropicle system. with the dropicle platform or for predicting expected efficiency of digital nucleic acid assays.

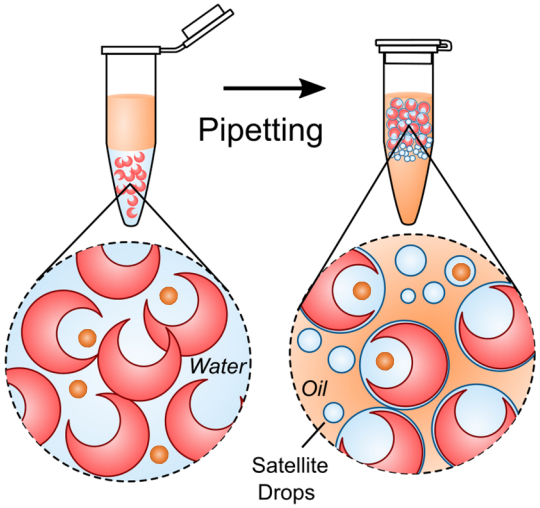


**Figure B-2 Depiction of suspended cells being encapsulated with the dropicle system.** For this approach it is expected that some fraction of the cells will be associated with the dropicles while another fraction will be associated with the satellite droplets that form after agitation.

We assume that there is some volume fraction of water in between particles and that sample entities are randomly distributed in these water volume fraction ($VF$). We will define this volume fraction as the void fraction

$$VF \equiv \frac{Volume\ of\ water\ in\ between\ particles}{Total\ suspension\ volume} \qquad \textbf{Equation B-8}$$

and the encapsulation efficiency ($E$) is defined as

$$E \equiv \frac{Water\ volume\ associated\ with\ dropicles}{Total\ water\ volume}. \qquad \textbf{Equation B-9}$$

For dropicles formed with spherical particles the loading efficiency is expressed as

$$E_{sphere} = \left(\frac{1-VF}{VF}\right)\left(\frac{V_{water}}{V_{sphere}}\right) \qquad \textbf{Equation B-10}$$

where

$$V_{sphere} = \frac{\pi}{6}(D_{out})^3$$

$$V_{water} = \frac{\pi}{6}\left(D_{drop}\right)^3 - V_{sphere}$$

and $D_{out}$ is the particle outer diameter and $D_{drop}$ is diameter of the surrounding droplet. For cavity containing particles we consider a new void fraction $VF_{crescent}$ in which the nanovial cavity is taken into account

$$VF_{crescent} = VF + (V_{in}/V_{out})(1 - VF) \qquad \textbf{Equation B-11}$$

where

$$V_{in} = \frac{\pi}{6}(D_{in})^3$$

$$V_{out} = \frac{\pi}{6}(D_{out})^3$$

and $D_{in}$ and $D_{out}$ are inner cavity diameter and outer particle diameter. Encapsulation efficiency is defined as

$$E_{crescent} = \left(\frac{1-VF_{crescent}}{VF_{crescent}}\right)\left(\frac{V_{water}}{V_{crescent}}\right) \qquad \textbf{Equation B-12}$$

where

$$V_{crescent} = V_{out} - V_{in}$$

$$V_{water} = \frac{\pi}{6}\left(D_{drop}\right)^3 - V_{crescent}.$$

Using these expressions, we can now predict the expected encapsulation efficiency for dropicles formed with various particle morphologies (spherical vs crescent) and different operating conditions such as the starting void fraction (**Figure B-3,4**). We also explore how less predictable parameters such as the final droplet layer thickness affect efficiency.

It is noted that for all conditions, inclusion of a cavity in the particles improves the expected encapsulation efficiency. In the case of the spherical particles only the thin outer water layer is associated with the dropicles leading to relatively low efficiencies. For crescent shaped particles the cavity increases the volume that can be associated with each particle. As the cavity size is increased the efficiency increases as there is a larger water capacity per particle. In practice the size of the cavity is limited by manufacturability (how consistently they can be fabricated) and the physical stability of the shape (i.e. do the particles collapse under mechanical stress).

In general, as the void fraction is reduced the encapsulation efficiency is improved as less sample is partitioned into satellite droplets (**Figure B-3**). In practice the lower limit of the void fraction is limited by the packing density of the particles as well as the ability to break apart the particles during the dropicle formation when they are tightly packed. For many systems the void

fraction can be less the what is predicted by the packing density of rigid spheres since most particles are composed of soft materials such as PEG-based hydrogels which are compressible.

As the outer water layer thickness of the dropicle system is increased we note that the predicted encapsulation efficiency is increased (**Figure B-3,4**). This makes intuitive sense since this layer is reduced via shedding of fluid into satellite droplets. It should be noted however that it is difficult to design a system to achieve a specific droplet layer thickness as the energetically minimal state is when the outer water layer approaches zero.

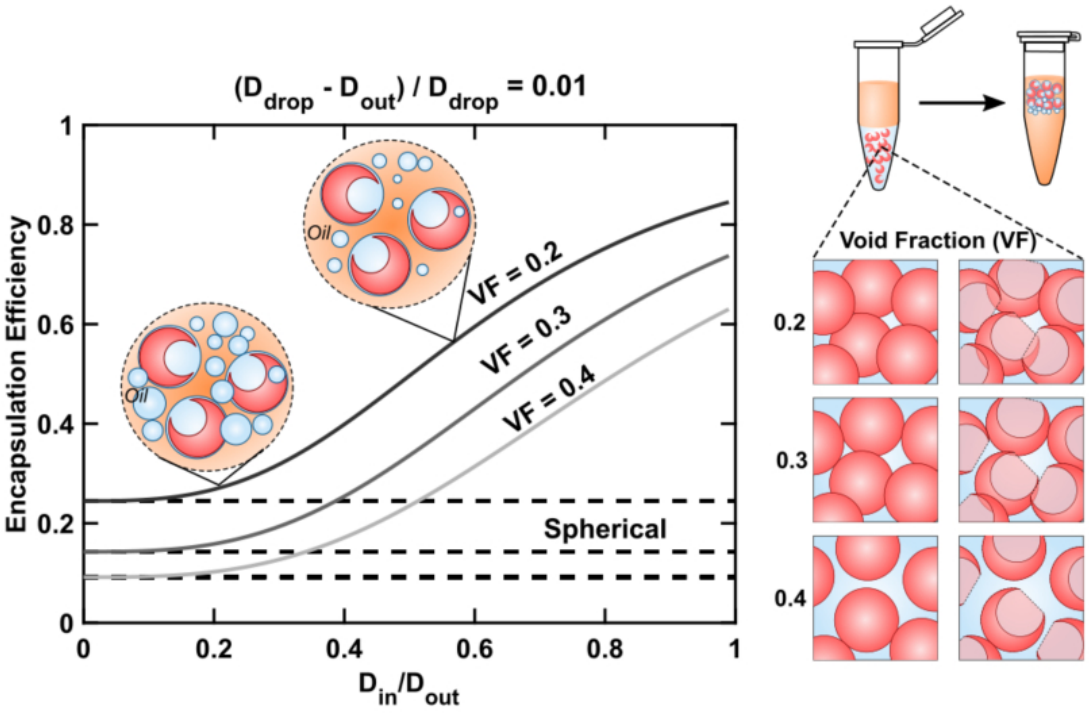


**Figure B-3 Effect of particle packing density and particle shape on theoretical encapsulation efficiency.** Cavity containing particles have improved encapsulation efficiency compared to dropicles formed with spherical particles. Decreasing the void fraction reduces fraction of sample volume that partitions into satellite droplets increasing the efficiency.

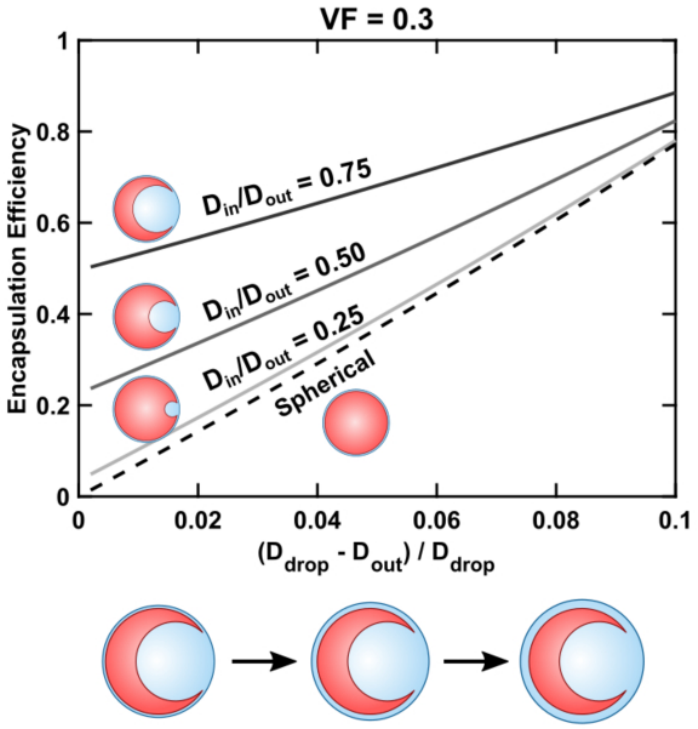


**Figure B-4 Effect of particle shape and resulting outer water layer thickness on theoretical encapsulation efficiency.** As the thickness of the water layer between the outside of the particle and the oil layer is decreased the encapsulation efficiency decreases and larger variation between the different particle shapes is observed.

# Appendix C

## Supporting information for Chapter 3.

### Theoretical fluorescence intensity for a spherical microgel

To estimate the line intensity across a single μgel we consider it as a perfect sphere with completely uniform fluorescence intensity. Assuming the depth of focus is larger than the depth of the entire sphere the line intensity ($I$) is proportional to the local height of the microgel ($h$), the intensity profile across the centerline of the gel particle is as follows:

$$I(x) \propto h(x) = 2\sqrt{r^2 - x^2} \qquad \textbf{Equation C-1}$$

where $x$ is the distance from the center of the gel, and $r$ is the outer radius.

**Table C-1 Throughput comparison of devices used to fabricate microgels from similar polymeric materials**

| Paper | Device | Oil | Material | wt% | microgel Size [μm] | CV [%] | Throughput [mL/hr] |
|---|---|---|---|---|---|---|---|
| This work | Step emulsification (200X) | HFE 7500 | 8-arm PEG, 20 kDa | 4% | 100 | 5 | 7.2 |
| | | | | 12% | 107 | 3 | 14.4 |
| Griffin et al. (2015) | Flow focusing | Mineral Oil | 4-arm PEG, 20 kDa | 5% | 100 | <6 | 0.12 |
| Sideris et al. (2016) | Flow focusing | Mineral Oil | Hyaluronic acid, 60 kDa | 3.50% | 74 | 13[a] | 0.072 |
| Sheikhi et al. (2018) | Flow focusing | HFE 7500 | Gelatin methacrylate, 50-100 kDa | 20% | 140 | <5[a] | 0.03 |
| Koh et al. (In Submission) | Flow focusing | HFE 7500 | 4-arm PEG, 20 kDa | 5% | 100 | | 1.2 |
| | | | | 12% | 100 | | 0.6 |
| Mealy et al. (2018) | Parallel flow focusing (8X) | Hexadecane | Hyaluronic Acid, 75 kDa | 5% | 43 | ~23[a] | 0.6 |
| Headen et al. (2018) | Parallel flow focusing (6X) | Mineral Oil | 4-arm PEG 20 kDa | 6.50% | 65.1 | 12.7 | 0.072 |
| | | | | | 104.5 | 9.6 | 0.6 |

[a] CV estimated from reported data.

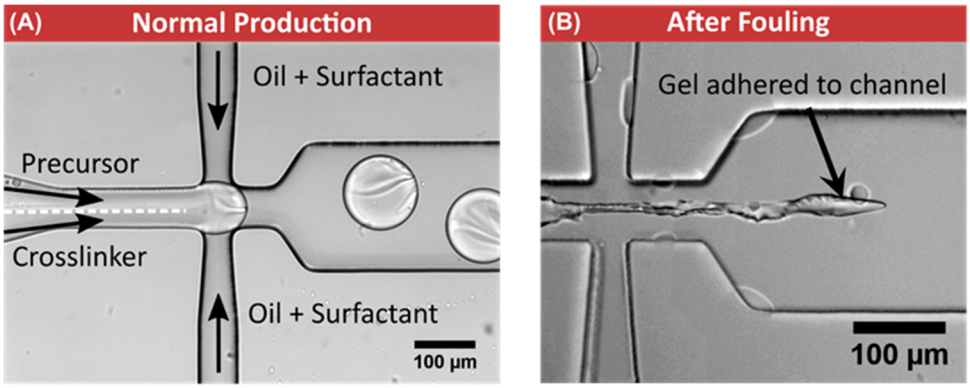


**Figure C-1 Fouling of flow focusing device due to polymerization at the precursor/crosslinker interface.** 4 wt% 8-arm PEG and PEG dithiol were used as the precursor and crosslinker. Fouling limits this approach to slow reacting chemistries and prevents long term production.

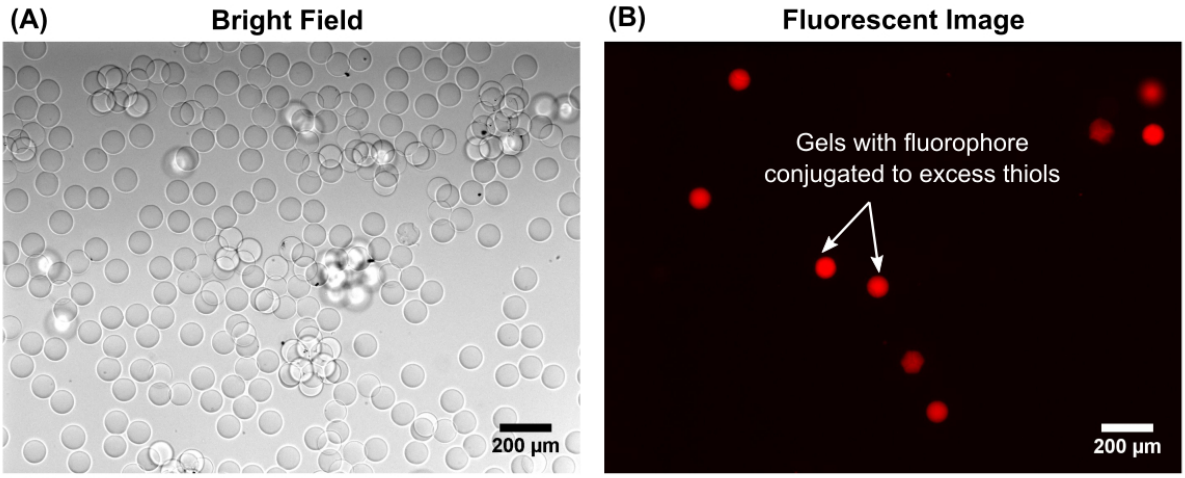


(C)

| | Total | Fraction |
|---|---|---|
| Free thiols present | 20 | 2.95% |
| No free thiols | 659 | 97.05% |

**Figure C-2 Microgel fabrication variation due to improper mixing of precursor and crosslinker solutions using previous flow focusing device.** Microgels were fabricated such that only 80% of the vinyl sulfone groups in the precursor would be occupied by thiol groups on the crosslinking molecules. The resulting microparticles were post modified with a Maleimide conjugated fluorophore to tag in remaining thiol groups in the particle matrix. Results showed that there was a sizeable population of gels with large excess of thiol groups suggesting fluctuation in the precursor crosslinker ratios. This could be due to fluctuations in controlling the volumetric ratios of co-flowing streams over long periods of time in microfluidic systems.

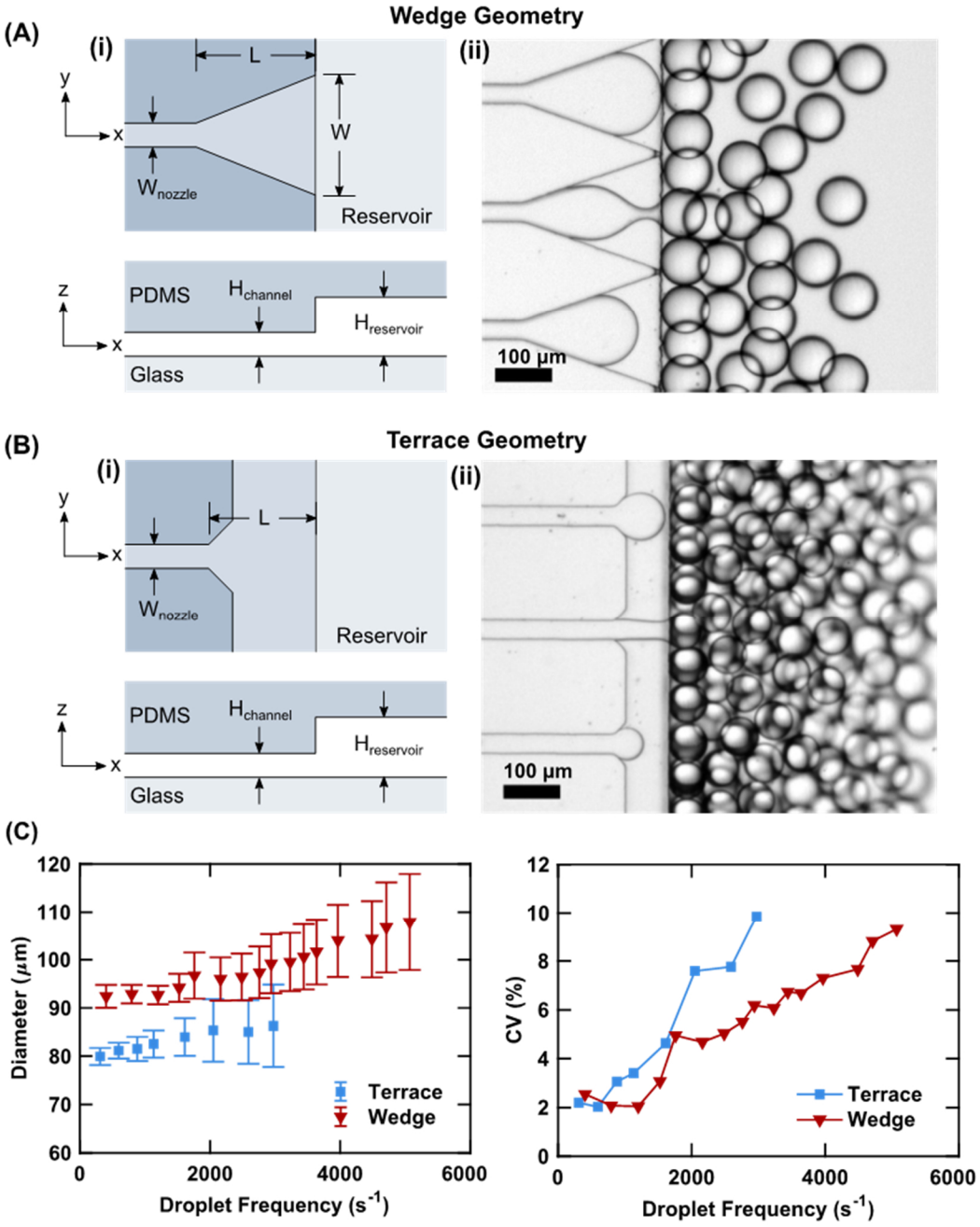


**Figure C-3 Comparison of nozzle geometries in a step emulsifier device.** Here we looked at both a wedge geometry (A) and more traditional terrace geometry (B). It was noted that, in general, the wedge geometry maintained higher uniformity at higher droplet production frequencies (C). 100 Nozzle devices were compared for both geometries using 4 wt% PEG as the dispersed phase.

**Table C-2 Dimensions of devices used in this study. All dimensions given in micrometers.**

| Channel Geometry | Droplet Size [µm] | $H_{channel}$ [µm] | $H_{reservoir}$ [µm] | $W_{nozzle}$ [µm] | L [µm] | W [µm] |
|---|---|---|---|---|---|---|
| Terrace | 80 | 25 | 150 | 30 | 100 | NA |
| Wedge | 90 | 25 | 150 | 30 | 247 | 200 |
| Wedge | 50 | 11 | 130 | 20 | 190 | 150 |

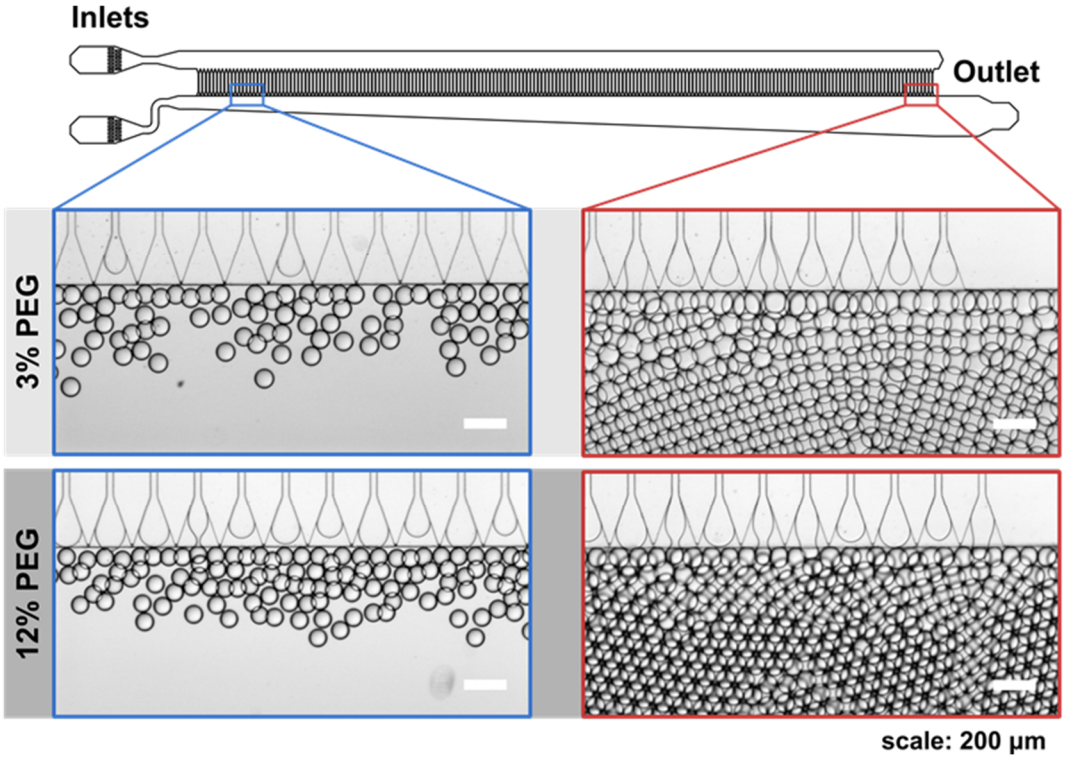


**Figure C-4 Viscosity of dispersed phase appeared to effect droplet generation across the whole length of parallel channels.** For low viscosity solutions we observed nonuniform utilization of droplet producing channels, leading to crowding in regions (3% PEG, right). In general, we noticed a more even utilization of channels for more viscous materials (12% PEG).

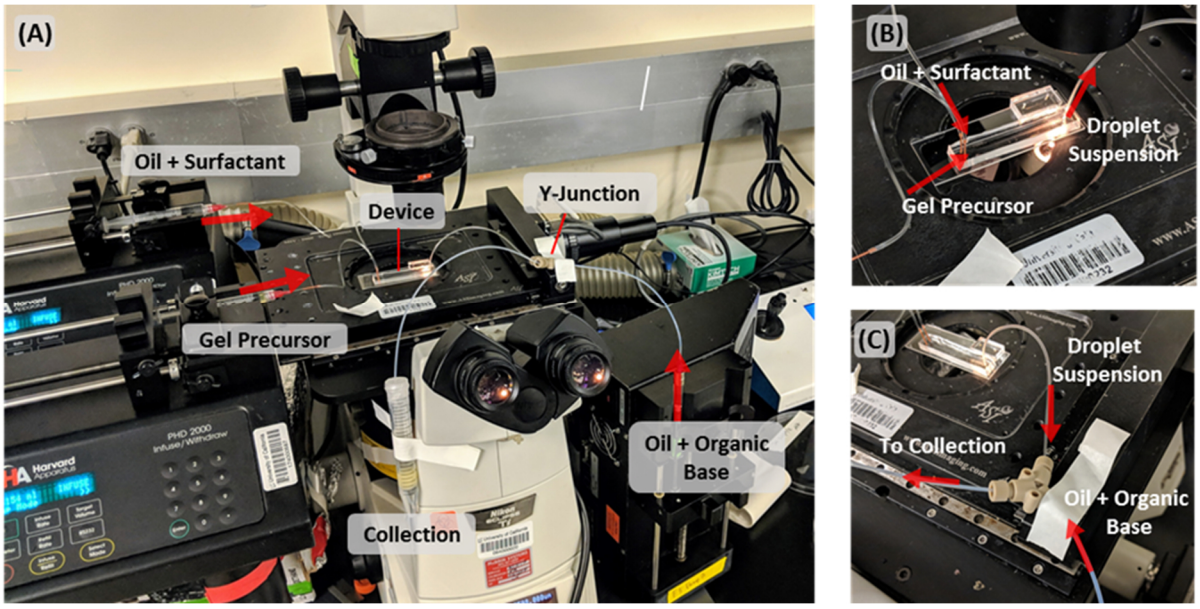


**Figure C-5 Images of experimental setup for particle fabrication using step emulsifier and pH modulation.** (A) General equipment setup; (B) PDMS droplet generator; (C) Y-junction used to introduce organic base to initiate gelation.

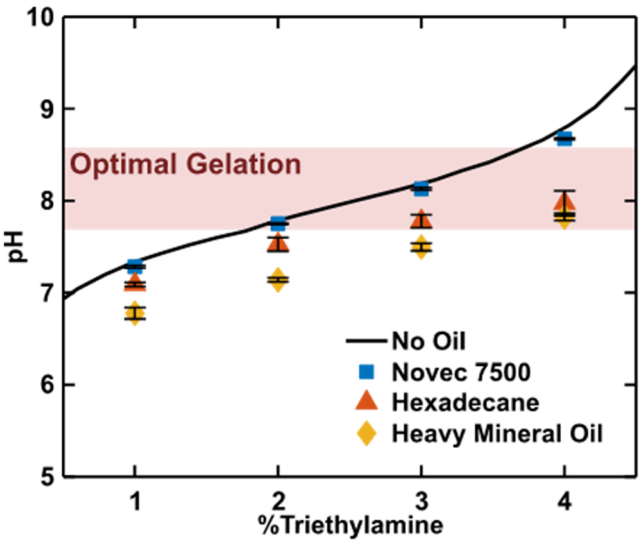


**Figure C-6 Bulk measurements of pH modulation in different oils.** Various amounts of triethylamine were added to a buffered solution (0.3 M triethanolamine, pH 5) indirectly through the oil phase listed in the legend at a 1 to 1 ratio (volume percent relative to aqueous volume). Solutions were mixed via vortexing and the pH was measured using an electronic pH meter (Mettler-Toledo FiveEasy pH meter). For the hexadecane and mineral oil conditions a large amount of the triethylamine remains in the oil phase as indicated by the lower pH as compared to the no oil condition. For the Novec 7500 oil condition nearly all of the triethylamine partitions into the aqueous phase after mixing as indicated by the close correlation to the no oil condition.

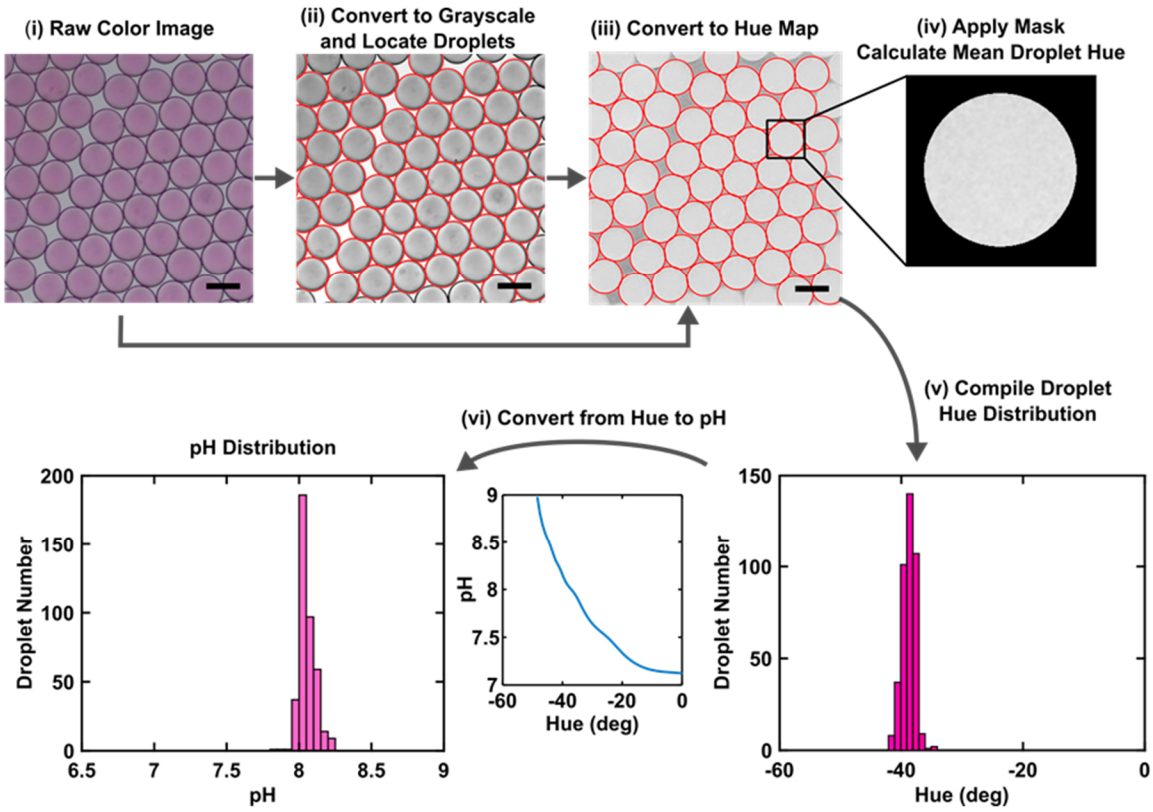


**Figure C-7 Workflow for calculating pH distribution among droplets.** (i-ii) Raw color image is converted to grayscale and droplets are identified. (iii-v) Image is converted to hue values and the mean droplet hue is calculated for each droplet and compiled. (vi) Hue is then converted to corresponding pH value using a calibration curve. All scale bars are 100 µm.

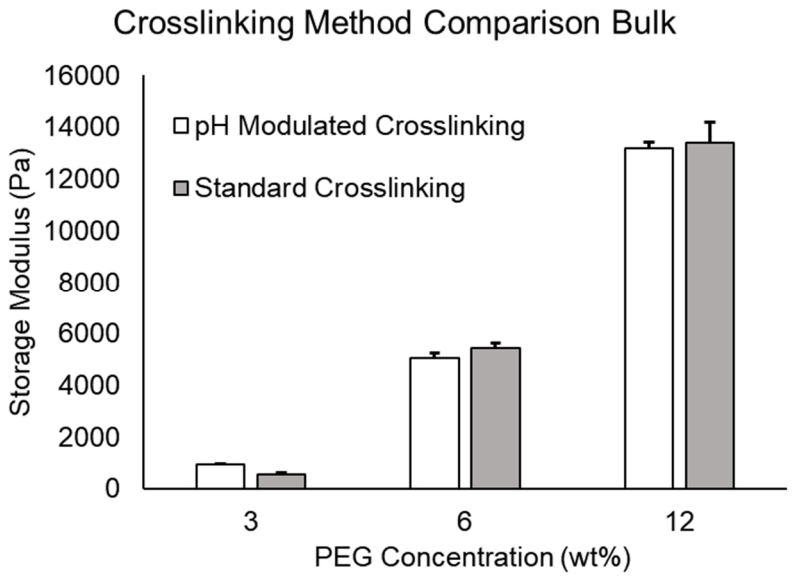


**Figure C-8 Storage modulus of bulk gels crosslinked using standard crosslinking and pH modulation approaches.** Resulting rheometric measurements showed little to no difference between the two approaches indicating that using an organic base to adjust the pH of the solution has little effect on the resulting hydrogel properties.

**Table C-3 Extrapolated droplet production throughput from 10 channel step emulsification device.**

| | **Throughput CV<3% (mL/hr)** | | |
|---|---|---|---|
| **PEG wt%** | 10 Channel Device | 200 Channels Extrapolated | 200 Channels Actual |
| 4 | 1.5 | 30 | 7.2 |
| 12 | 1.35 | 27 | 14.4 |

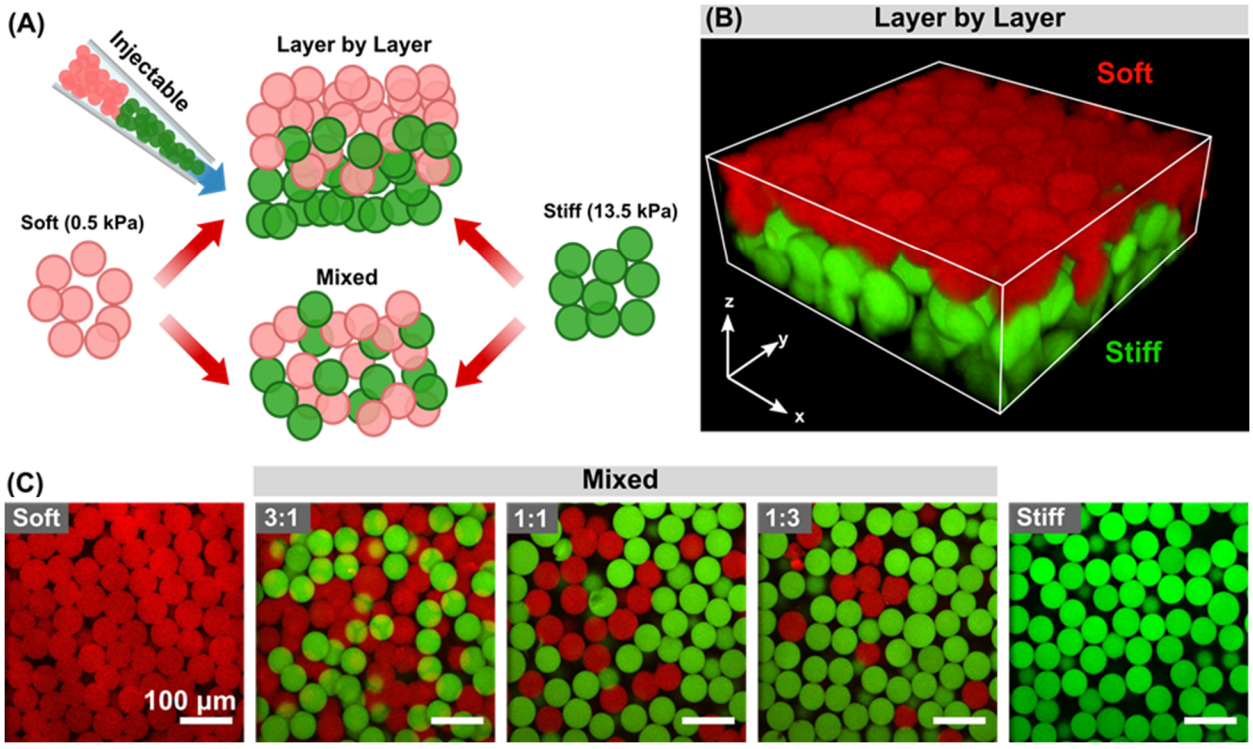


**Figure C-9 Fabrication of injectable mechanically heterogeneous scaffolds from modular building blocks.** (A) Schematic showing various schemes for injectable heterogeneous scaffold formation. Here we experimentally demonstrate both layer-by-layer (B) and mixed (C) scaffolds composed of 50 µm µgels. 3D confocal stack dimension: 350 x 350 x 150 µm. Large gradients in materials properties are possible.